Migration of interneuronal precursor cells in the developing cerebellum of mice: model-based cell tracking and simulation

Dissertation

zur Erlangung des Doktorgrades (Dr. rer. nat.)
der
Mathematisch-Naturwissenschaftlichen Fakultät
der
Rheinischen Friedrich-Wilhelms-Universität Bonn

vorgelegt von
David Hecker
aus Köln

Bonn
September, 2010

Angefertigt mit Genehmigung der Mathematisch-Naturwissenschaftlichen Fakultät
der Rheinischen Friedrich-Wilhelms-Universität Bonn

1.Gutachter: Prof. Dr. Wolfgang Alt
2.Gutachter: Prof. Dr. Karl Schilling

mündliche Prüfung: 19.11.2010
Erscheinungsjahr: 2010

Contents

Introduction

Since many years the cerebellum, as well as the brain, continues to be an ongoing intensive research topic. Their very complex, yet highly conserved structures which give rise to fascinating functions like complex motor control (cerebellum) and higher thought processes (cerebrum), make them popular objects of attention. Additionally, this very organized nature particularly opens the cerebellum to a great many research options, as small defects/interferences usually lead to observable morphological and/or functional abnormalities. Thus, our knowledge of tissue composition and of cells that make up these tissues has steadily increased in recent years. However, there remains much that still needs to be discovered particularly when considering embryogenesis and early postnatal development.

Coinciding with its primary task of control of motor functions, the cerebellum shows a large boost in volume just after birth (see fig.1). During this developmental phase the cerebellum features a unique layered structure consisting of the external granular layer (EGL), molecular layer (ML), Purkinje cell layer (PCL), internal granular layer (IGL). Each of the mentioned layers is made up of several different types of neurons and supporting cells as well as extracellular matrix (ECM) (see fig.3)). Beyond these layers the white matter (WM) is located, mainly consisting of axons providing sensory input from the precerebellar nuclei and inferior olive.

The EGL is a germinal zone where precursors of granule cells proliferate and develop before they finally migrate through the molecular layer into the IGL to fully mature and assume their final positions by making contact with the primary source of input into the cerebellum, mossy fibers. Consequently, the EGL vanishes as development of the cerebellum terminates. The molecular layer consists of different inhibitory interneurons (mainly stellate and basket cells), the axons of granule cells (parallel fibers; proceeding from the IGL), as well as glia cells and their processes. Furthermore, it contains the Purkinje cell dendrite trees, while the Purkinje cell bodies are located in the correspondingly named Purkinje cell layer. The PCL also contains

Bergmann glia cells that extend their processes up to the EGL, these processes are known to be used by developing granule cells as guiding structures on their way to the IGL ([1], [2]). Below the PCL we find the IGL and directly at the border of these two tissues Golgi neurons are located. These are inhibitory interneurons receiving input from mossy fibers and forming feedback loops with granule cells. For a more detailed overview of the cerebellum's structure see [3] and of the cells comprising it [4]. The review article [5] additionally contains information about cerebellar circuitry.

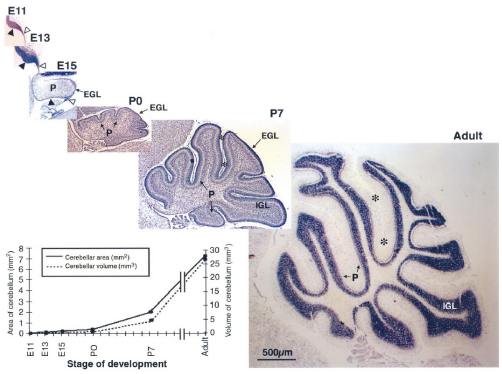

Figure 1: Overview of the development of a cerebellum of mice between embryonic day 11 (E11) and adult. Notice the strong increase in volume growth starting right after birth (P0). Picture taken from [4].

For a long time the EGL was thought to be the primary germinal zone of the cerebellum, giving rise not only to granule cells but also to other interneurons. In 1996 it was shown by Zhang and Goldman that the EGL contains granule cell progenitors only, while precursors of interneurons and glia cells were migrating from the deep cerebellar anlage through the WM into the cerebellar cortex ([6], [7]). By now it has been established that precursors of cerebellar interneurons originate from the ventricular zone and migrate into the cerebellum via the nascending white matter. It is then a question of how this migration is controlled and how cells manage to find their destination area. When Maricich detected Pax2 as a marker specific to inhibitory (GABAerg) interneurons and their precursors [8] it was possible for the first time to target these cells specifically. It was only a small step to establish a GFP marked mouse strain and, finally, to producing time-lapse movies of cerebellar slices depicting GFP-marked Pax2-positive interneuronal precursors (see fig.2 for an exemplary image). In particular, imaging of cerebellum preparations of 8 day old mice build the basis of this work.

Preparations are 250 μm thick slices cut with a tissue chopper from extracted cerebella

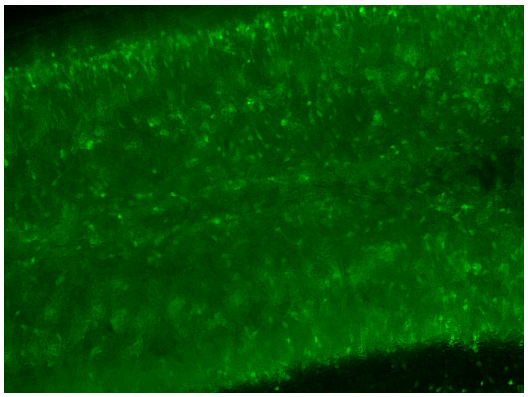

Figure 2: Image 1 from a time-lapse movie consisting of 96 images. Depicted is a slice of the cerebellum of an 8-day old mice (P8). Fluorescent cells have been Pax2-GFP marked. Images produced and provided by the group of Prof. Dr. Schilling at the Institute of Anatomy and Cell Biology of the University of Bonn.

of decapitated mice at postnatal day 8. Preparation steps will be outlined in section see 1.2.1. With these movies it was feasible to analyze the migration of precursors of inhibitory interneurons by the use of direct imaging. Due to technical limitations it was necessary to establish a method of correcting slice deformations occurring during the recording process, which we performed in [9]. Previous analyses of these corrected recordings showed differences in mode of migration within white and grey matter and particularly suggested that cell move along (guiding) structures. Indications of this were consistently straight path sections and a phenomenon we termed "path reversal" (see figs.2.2a,b).

Overview and goals

The goal of this work is to investigate the migration behaviour of precursors of inhibitory interneurons on their way from the ventricular zone through the nascending white matter into the molecular layer of the cerebellar cortex. To this end, we will employ a two-sided approach. First, development and implementation of a tracking program to extract necessary data and, second, design of a mathematical model to simulate this particular type of cell using the gained information. Finally, we will compare simulation and tracking results to increase our understanding of this type of cell and its migration during development of the cerebellum.

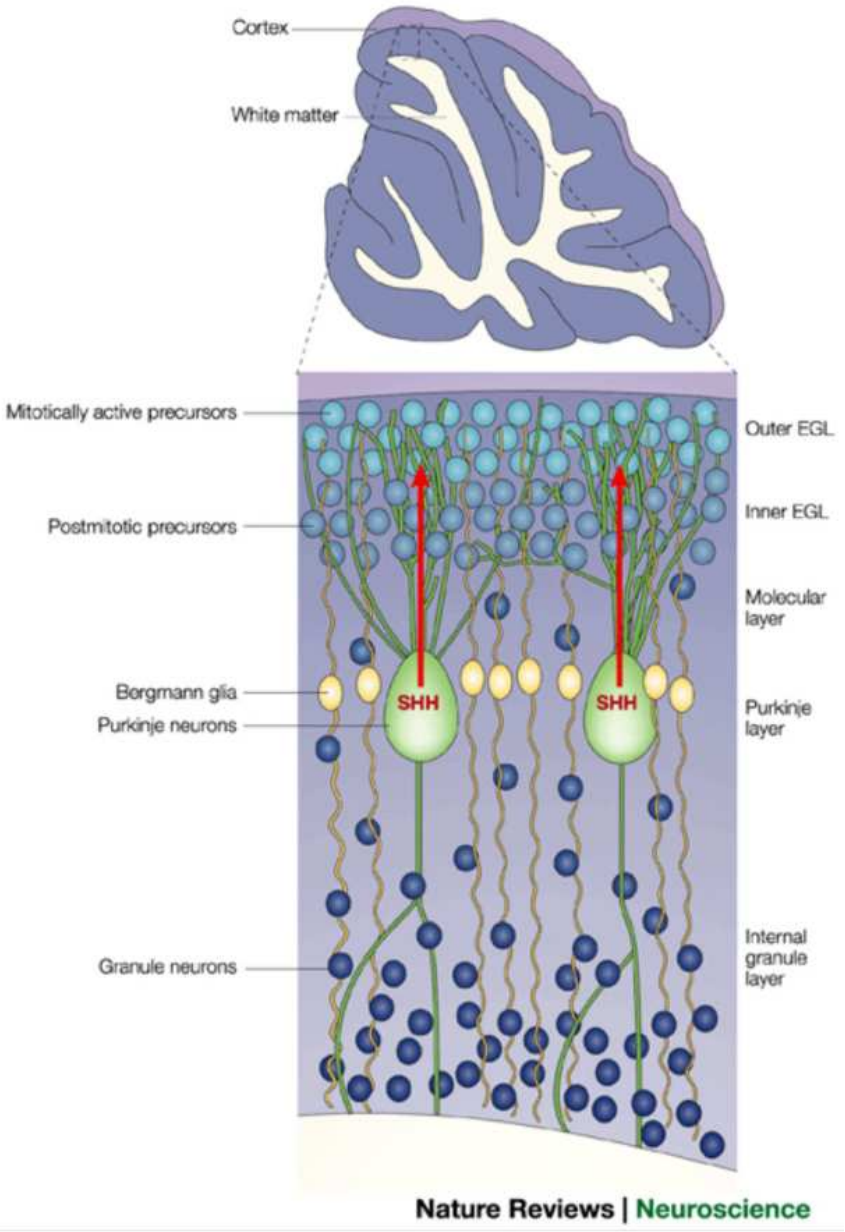

Figure 3: Layers of a developing cerebellum. From outside to inside: outer external granular layer (EGL) containing mitotically active granule cell precursors. Inner EGL containing postmitotic granule cell precursors starting to migrate towards the internal granular layer (IGL) along Bergman glia fibers. The molecular layer (ML) contains, among others, inhibitory interneurons and the Purkinje cell dendrite trees. This is the final destination of the interneuronal precursor cells examined in this work. Inside the IGL the mature granule cells find their final positions. Below the IGL the white matter begins (not shown).

Chapter 1

Model based cell tracking using image forces

1.1 Introduction

In recent years, as imaging and computational methods and hardware improved steadily, we have seen a huge increase in dynamic imaging data. Especially the cell imaging community feels the need for reliable and fast methods for comparing large numbers of images and image sequences (time-lapse recordings, for instance) and, for example, to track individual objects (such as cells) in such image sequences. Consequently, the number of available tracking programs has increased as well. Why the need for yet another tracking software?

Prevalent methods for tracking of objects can be split into a few different categories [10]. Thresholding (segmenting the image via a (fixed) brightness threshold) is a simple and commonly used method, even though it is prone to errors [11]. As a more advanced method, boundary templates have come into use for cells with fixed cell shapes [12] & [13]. These methods use *a priori* knowledge about the designated target cell morphology to identify and follow objects in images. Understandably, this method is not suited to track shape changing cells like the interneuronal precursor cells discussed in this work. A third method, developed by Beucher in 1979 [14], is called "watershed" and interprets grey scale images as a topographical relief that is then "flooded". This method often suffers from oversegmentation, an effect where the image is split into too many fragments. Related, but not a tracking method by itself, is the concept of cell skeletons [15]. Cell skeletons are a reliable method for detecting cell shape in single images, based on application of equal border distance algorithms.

Recently, model-based tracking programs have come more and more into use. These programs do not rely on image properties alone, but also incorporate terms including image-independent factors as, for instance, size and maximal bending of target cells. We usually find two different basic methods used in model-based tracking. First, the level-set method, which is ideal for tracking shape-changing objects due to its non-parametric numerical approach [16]. The second method prevalently used for tracking cell position and shape is that of a deformable model cell based on parametric contours (see, for instance, [17] & [18]).

Thus, none of the above methods seemed appropriate for our needs. Neur(on)al migration, which was at the center of our interest, is typically characterized by cell locomotion along guiding structures (see, for instance, [1], [2]). A reasonable assumption, then, is the concept that not only position and direction, but also cell shape systematically relate to such structures. Thus, we needed a method that was capable of extracting not only positional information (which is all many available programs track), but was also able to yield information on cell shape, especially length and lengths distribution into front and rear. On top of this an additional advantage of the model we finally decided on, is the inclusion of internal brightness values to determine a cell center and, thus, the ability to detect changes in cell polarity by altered brightness levels, even if position and shape remained fixed. And, finally, we wanted a method suitable to perform tracking automatically.

The program introduced here is based on the general idea of model based 2-dimensional image processing by using virtual cell models ("adaptive templates") representing morphological properties of a projected cell image. More precisely, a cell in any given image is to be represented by a template consisting of a cell center and two extensions termed "legs". Image forces calculated from brightness values of the target image are then applied to adapt the template to the target cell in every given movie image.

The model's setup reflects the following common views on cell migration. In effect, protrusion of a leading edge in a direction ultimately defining migration direction is followed by movement of the cell body and finally the trailing edge. Accordingly, for the template, fitting of leg length is done first, followed by orientation adaption and finally displacement of cell body. However, instead of accounting for retraction last, it is considered together with protrusion and modeled as a single length adaption process. This is in part motivated by programming considerations, and also because there is, in general, no predefined leading and trailing edge in our model template. Thus, separate calculations for protrusion and retraction are avoided leading to faster

program runtime.

Due to ongoing model development, there are currently two different versions of the program, called "rigid" and "hinged". The first does not allow bending of the cell template ("rigid"), which is thus modeled as a straight rod going through the cell center. This version sports faster processing of images and is best used for stiff cells that do not show a large degree of bending or other distortions.

In the second version, the cell center basically acts as a hinge, around which both legs can rotate. Processing time of this version is increased, but it yields increased fitting precision especially for shape-changing cells. Currently, the program tracks two legs, but in principle there is no technical limit to the number of legs hinged at the cell center.

We will take a detailed look at the rigid template and its algorithms before proceeding to the hinged model, which is exclusively used throughout the later chapters of this work.

1.2 Methods

1.2.1 Tissue preparation & time-lapse movies

Time-lapse images used throughout this work have been supplied by the group of Prof. Dr. Schilling at the Institute of Anatomy and Cell Biology of the Rheinische Friedrich-Wilhelms-Universität Bonn. Slices of cerebella of 8-day old Pax2-GFP mice have been extracted and subsequently cut using a Tissue Chopper. Slices were cultivated for 4 hours in PLL-coated 12-well plates in $500\mu l$ Neurobasal/B27/2mM L-Glutamax medium at 37° and $5\%CO_2$. Afterwards slices were transfered to a DM IRE2 breeding chamber and images were taken every 10 minutes over a period of 16 hours using a Leica DFC 350 photo camera. Resulting time-lapse image sequences thus consist of 96 consecutive image.

1.2.2 MTrackJ

Some tracking results we refer to were taken from a previous work [19]. These were gained by the use of a manual tracking program called *MTrackJ*, which is a plugin for a common image editing program by the name of *ImageJ*. *MTrackJ* is available for free at [20] and *ImageJ* is available at [21]. For parameter setting and similar, refer to [19].

1.2.3 MatLab

All programming during the course of this work has been done using MatLab [22]. This includes the fitting program and simulation model, but also statistical analyses like correlation and orientation analysis for which we used internal programs developed by our group of Theoretical Biology at the University of Bonn.

1.3 "Rigid" fitting model

This program defines the cell template as a single straight line through the cell center representing the longer cell body axis, and is most useful for oval cells without large deformations. In particular, the virtual cell is represented by a discrete cell center from which two legs emanate. In the rigid version of the program, these legs are independent from each other in length, but not in angle.

Thus, as previously mentioned, the rigid model uses a template that is essentially a stiff rod (compare fig.1.1). This rod does have two lengths parameters, a front and a rear length, defined by the distance from the center to each respective tip. The center does not act as a hinge in this case. Obviously, this template is calculation-time efficient, but can be efficiently used only to fit rigid target cells.

In general, motion of the virtual cell template from one frame to the next should reproduce the frame-to-frame deformation and locomotion of the analyzed cell. To this end, a large number of iterations (up to 200) of image force calculation, subsequent application of these forces to the template and resulting template displacement is employed to each frame. Table 1.1 shows a flow diagram for a single iteration of this process.

First, based on the primary image of the stack, a subroutine establishes starting position and orientation of the virtual cell template roughly fitting the target cell. Then, from pixel brightness values a subroutine calculates image forces longitudinal to the template and, from those, protrusion and/or retraction for both leg tips separately. Next, transversal forces are determined to derive a torque and to establish cell rotation. In the last two steps, longitudinal and transversal forces are used to identify displacement of the virtual cell center.

All of these steps comprise a single iteration of the program after which the whole process is repeated. This is done for a large fixed number of iterations (usually between 100-200) or until a certain stop condition is met. Stop conditions usually include low to no change in calculated forces and/or displacement of cell center or

image forces	template change
	startpos
	(first image only)
	|
longitudinal forces	**protrusion/retraction**
|	|
transversal forces, torque	**rotation**
|	|
longitudinal forces	**center longitudinal movement**
|	|
transversal forces	**center transversal movement**

Table 1.1: Flow diagram of one iteration of the tracking process, including image forces calculated **(left)** and corresponding cell template adaptation process **(right)**. Between 150 and 200 iterations are calculated during the fitting process of a single image, depending on image quality and target cell shape.

either cell leg.

If the program is used to track a cell across more than one image (the usual case), the next image is loaded once the stop condition is met. Necessary data of the virtual cell template are saved, transfered as starting position onto the new image and tracking is continued. Technically, once all images have been processed, the program can continue on to further cells on the same image stack, again starting with the first image of the stack. Or, alternatively, the program can track several cells on a given image before loading the next image of the stack and continuing all previous tracks.

1.3.1 Function and algorithms

We will now present a detailed calculation of image forces for each component in the same order as shown in the flow diagram (see tab.1.1). Generally, for the rigid model, the full template is defined by position of the center (x, y), the length of either respective leg l_p and the angle of the legs α (with respect to the x-axis). Position of leg tips (x_p, y_p) can be easily calculated from center position, leg lengths and angle via

$$\begin{pmatrix} x_p \\ y_p \end{pmatrix} = \begin{pmatrix} x \\ y \end{pmatrix} \pm l_p \begin{pmatrix} cos(\alpha) \\ sin(\alpha) \end{pmatrix}. \tag{1.1}$$

For the different template motions, different parts of the equation will be fixed while forces are applied to the remaining parts. In effect, protrusion/retraction of the legs (change of leg lengths l_p) is calculated with a fixed center position and angle. For rotation of the template (change of angle α), cell center and leg lengths are fixed. For cell center displacement longitudinal to the template, leg tip positions (x_p, y_p) and α are fixed. While for displacement in orthogonal direction, l_p and α are fixed, but not (x_p, y_p) (compare fig.1.1).

Startpos

This subroutine is run once for each real cell to be tracked to determine starting position and orientation of the virtual cell template. It has two modes of operation, the first simply takes the first brightest spot it can find in the image, starting at the top left corner and working from left to right and top to bottom. (Notice that in an 8-bit greyscale image there can be several pixels with the highest brightness value.)

The second mode finds all pixels with a certain minimal brightness, then takes the mean of each of these and the respective twenty-four surrounding ones, and again compares this to a given minimal threshold brightness. Of all spots that surpass this threshold, it selects the brightest. The minimal brightness value, as well as the amount of surrounding pixels used for calculation of the mean, are parameters that need to be set depending on the overall brightness of the image, signal to noise ratio and size of target objects.

In a second step, after establishing the template's center position, the subroutine rotates a virtual ray of given length 360° in eight steps of 45° around the selected pixel and measures brightness values along this ray for all orientations. The orientation with the highest brightness sum is then chosen as the starting orientation.

Finally, starting position and orientation are reported back to the tracking program.

Furthermore, this subroutine can also be used as a safeguard in case the virtual cell template loses its real counterpart during the tracking process. This can happen, for instance, if the real cell moves very fast and out of detection range of the virtual cell. In this case, the *startpos* subroutine can be called to find the real cell again, set the virtual cell template on top of it and continue tracking.

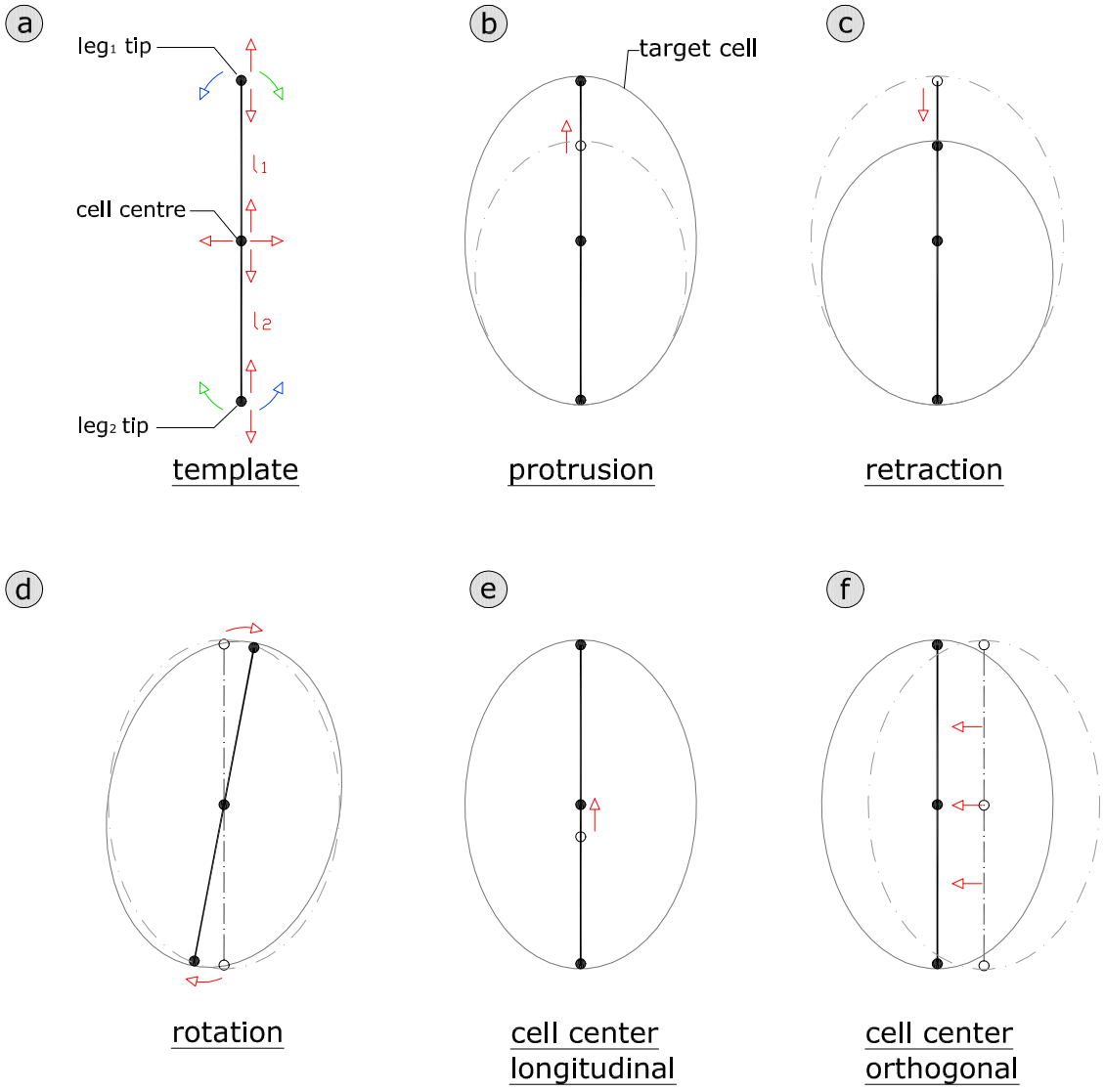

Figure 1.1: Rigid template overview: Possible template adaptation processes. **(a)** The template incorporates three mobile entities, namely, the two leg tips and the cell center (black dots). While the center can move in longitudinal and orthogonal directions, the tips can displace along the longitudinal axis (effectively changing the length of the template) and jointly rotate. **(b-f)** Adaptation processes: The grey oval represents a schematic target cell and the black rod denotes the template adapting to this cell. Filled circles and lines represent the template with tip and center positions, while open circles and dashed lines denote the same entities at positions prior to the adaptation process.

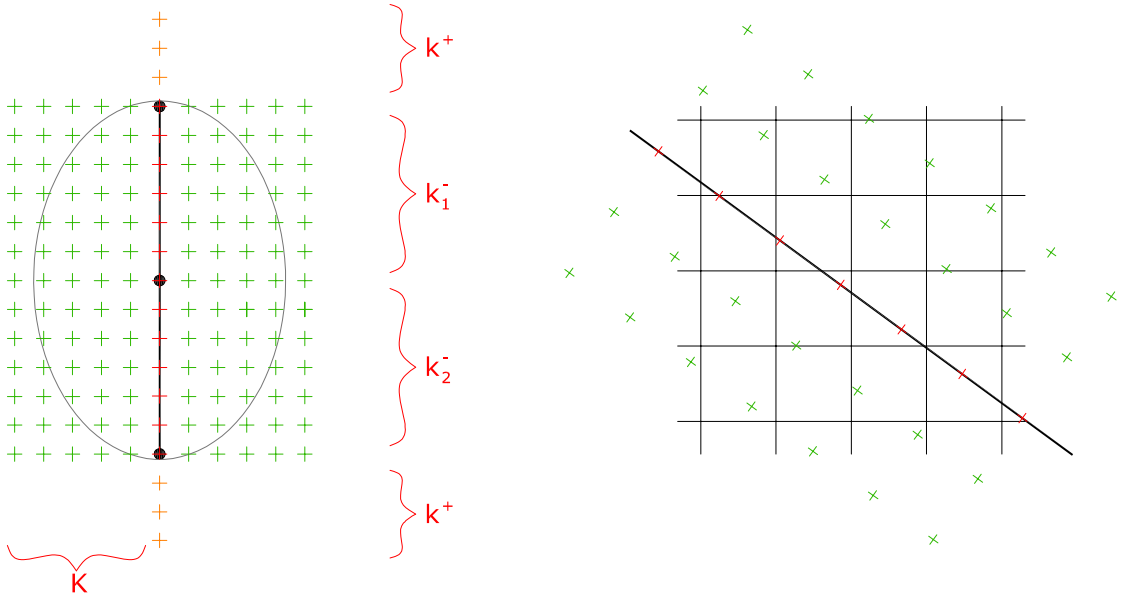

Figure 1.2: **(Left)** Brightness reading around the template. The grey oval represents a target cell, while the black rod represents the template. Crosses mark designated points at which pixel values are read. Values at positions with red crosses are used in protrusion, green crosses in rotation and cell center orthogonal displacement. Orange crosses are used in cell center longitudinal displacement and retraction. K is the parameter determining the width of brightness readings. k^+ sets range of brightness readings ahead of the leg tip to be used for calculation of image forces for protrusion, while k_1^- and k_2^- are variables storing leg lengths l_1 and l_2 in pixel distances. **(Right)** Illustration of a rotated template on the fixed image pixel grid. As before brightness readings are indicated by crosses. Values of pixel squares, in which a given cross falls, are read and used in image force calculations.

Protrusion & Retraction

On a given image, protrusion of a leg of the virtual cell template occurs if this leg does not reach the edge of the real cell, whereas retraction should occur if the template leg overshoots the real cell's edge (compare fig.1.1b, c).

First, pixel values at certain regular points between the template center and a given template leg tip are determined. Depending on the size of the target object, every pixel, every other pixel or every n^th pixel can be used. Throughout this work, usually every pixel is being used because the object size is small. To be able to measure any possible protrusion it is also necessary to check pixel values further out than the tip of a given leg (see Fig.1.1c). Again, the distance of this measurement is

a parameter to be chosen and its optimal setting depends on resolution and signal to noise ratio of the image, as well as the size of the target objects.

Using these pixel values, image force for protrusion is then calculated as the mean of distances weighted by respective pixel brightness outward from the given leg tip with weights g(H):

$$g(H) = [H - H_{th}]_+^2 \tag{1.2}$$

$$F_{prot,p} = s_{prot} \frac{\sum_{i=1}^{k^+} i\, g(H_i)}{\sum_{i=1}^{k^+} g(H_i)} \tag{1.3}$$

with p denoting legs, H_i being the brightness at distance i from the leg tip (Fig.1.1). In this case, every pixel until the k^+-th one. H_{th} is a threshold brightness to account for background noise and facilitate edge detection. s_{prot} is a parameter for protrusion strength, that needs to be chosen according to image and target object properties.

If there is no protrusion force, ie. if pixel brightness outward of tip is below the threshold (H_{th}), the program will calculate possible retraction forces. In this case, every pixel from the one at the tip of the respective leg p until the template center, where k_p^- ($\in \mathbb{N}$) denotes the distance from the center to the outmost pixel read.

Because of the way forces are calculated from brightness, equation 1.3 needs to be adapted for retraction force calculation to accommodate for force generation by low brightness between tip and center.

$$g(H) = [H - H_{th} - H_{mean}]_+^2 \tag{1.4}$$

$$F_{ret,p} = s_{ret} \frac{\sum_{i=0}^{k_p^-} i\, g(H_i)}{\sum_{i=0}^{k_p^-} g(H_i)} \tag{1.5}$$

with H_{mean} being mean brightness from tip to cell center and s_{ret} a retraction strength parameter. Retraction strength is generally set higher than protrusion strength to ensure cohesiveness of the template.

The resulting change of position of the tip position of the respective leg p, (x_p, y_p), is then calculated by an overdamped motion formula with a frictional coefficient of 1:

$$\begin{aligned} dl_p &= F_{prot,p}\, dt + \epsilon\, \xi\, \sqrt{dt} \\ dl_p &= F_{ret,p}\, dt + \epsilon\, \xi\, \sqrt{dt} \end{aligned} \tag{1.6}$$

Here ϵ is a factor for fluctuation strength and ξ is a normally distributed random number between -1 and 1. Finally, leg tip positions are updated using eq.1.1 (fixed center position and angle, leg lengths updated).

Orthogonal Forces and Torque

After adjusting length, the virtual cell legs are rotated to improve the fit to the given image of the real cell. For the rigid template this means that the legs rotate jointly. Forces are calculated from pixel brightness the same way as before, but this time with reading points transversal to the virtual cell's legs (green crosses in fig.1.2).

The width K of this reading is a model parameter determining the distance checked in both directions from the virtual cell's axis. This parameter needs to be set a little larger than the width of the target objects to ensure that target objects are wholly covered.

Image force calculation is analogous to the protrusion/retraction case, but instead of a linear dependency, a gauss shaped base function (eq.1.9) is used (see fig.1.3). The difference in underlying functions reflects the distinctive tasks: edge finding of a leg tip to determine leg length in the protrusion/retraction case, as opposed to finding the center balance point of image forces in order to establish a midline orientation.

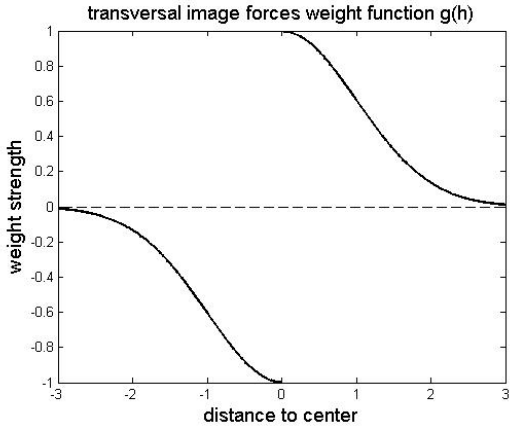

Figure 1.3: Weight function for transversal image forces, used for transversal displacement and rotation of template axis. Weight strength depends on distance between reading point and template in a gauss shaped fashion. The step at distance 0 originates from the need of distinguishing left (negative) and right (positive). The weight function value for a given reading point is determined by its distance. This value is then multiplied by the pixel brightness value at that reading point (compare fig.1.2, right side) to calculate resulting image forces used for template changes.

First, forces for each orthogonal are determined and summed up to get the resulting

force at each intersection i. Comparing figure 1.2 orthogonals are lines perpendicular to the template legs, they are comprised of green crosses and intersecting the template at orange crosses. In a second step, these forces are used to calculate torque, rotation and transversal displacement of the cell center.

$$g(H) = H^2 \tag{1.7}$$

$$F_{orth,i} = s_{orth} \frac{\sum_{j=1}^{K} W_j \, g(H_{i,j})}{\sum_{j=1}^{K} g(H_{i,j})} \tag{1.8}$$

where $H_{i,j}$ is the brightness along at transversal distance j from intersection i. For the orthogonal force calculation a function of the type

$$W(dist) = a \, \frac{sign(dist)}{\sigma \sqrt{2\pi}} \, e^{-\frac{1}{2}\frac{dist}{\sigma}^2} \tag{1.9}$$

is used. With a being an amplitude parameter, σ a parameter for the shape of the bell shaped curve and $dist$ being the distance to the template. In the current case $dist = j$ because every pixel brightness value is read. As soon as pixels are omitted this is not true anymore, usually applied for larger objects, where not every pixel value is used or brightness values are averaged. Maximum distance for orthogonal brightness measurement is defined in parameter K (compare fig.1.1).

Torque is calculated by multiplying transversal forces with their respective distance d_i from the cell center to the intersection i and a strength factor s_{rot}:

$$\Omega = \sum_i \omega_i = s_{rot} \sum_i \, d_i \, F_{orth,i} \tag{1.10}$$

Then, in analogy to 1.6 angular change is determined from torque:

$$d\alpha = (\frac{1}{\lambda_{rot}}) \, \Omega + \epsilon_{rot} \, \xi \, \sqrt{dt}, \tag{1.11}$$

where λ_{rot} is a friction, ϵ_{rot} the fluctuation strength and ξ a normal distributed random number.

Before calculating displacement of the virtual cell's center, the changed coordinates of the tips have to be determined using the new angle values. This is done for both legs p separately. In line with earlier comments, it is to be noted that application of torque is performed with fixed cell center and leg lengths, while angle and tip positions are updated.

Displacement of Cell Center

After determining protrusion, retraction and (in this case, combined) rotation of the front and rear legs, displacement of cell center is calculated. The resulting longitudinal displacement force F_{cl} is based on pixel brightness along the cell axis, similar to protrusion/retraction force calculation.

$$F_{cl} = s_{cl} \frac{\sum_{0}^{k^-} d_i \, H_i^2}{\sum_{0}^{k^-} H_i^2} \tag{1.12}$$

Where H_i is the brightness at distance d_i from the cell center towards either tip, with i being positive towards leg 1 and negative towards leg 2. s_{cl} is a strength factor for longitudinal force determination.
Longitudinal displacement along the cell axis is then given by

$$\begin{aligned} dx &= (\frac{1}{\lambda_{cl}}) \, F_{cl} \, cos(\alpha) + \epsilon_{cl} \, \xi \, \sqrt{dt} \\ dy &= (\frac{1}{\lambda_{cl}}) \, F_{cl} \, sin(\alpha) + \epsilon_{cl} \, \xi \, \sqrt{dt}, \end{aligned} \tag{1.13}$$

with fixed leg tip positions and angle α, (x, y) coordinates as well as lengths of the front and rear legs are updated.

Transversal displacement is done in a second step based on orthogonal forces determined previously (see eq. 1.8).

$$F_{co} = \sum F_{orth,i} \tag{1.14}$$

$$\begin{aligned} dx &= (\frac{1}{\lambda_{co}}) \, F_{co} \, cos(\beta) + \epsilon_{co} \, \xi \, \sqrt{dt} \\ dy &= (\frac{1}{\lambda_{co}}) \, F_{co} \, sin(\beta) + \epsilon_{co} \, \xi \, \sqrt{dt} \end{aligned} \tag{1.15}$$

with $\beta = \alpha + \frac{\pi}{2}$. This time, the angle is still fixed, but leg tips are released and may change position. Thus, new (x, y) and (x_p, y_p) coordinates are calculated. After this step, the program will check a possible stop condition and proceed accordingly.

1.3.2 Results

To ascertain the capabilities of the program, several test runs were performed, each with increasing demands to the fitting process. We started with a simple binary image,

parameter	value	description
t_{end}	15	iteration time
dt	0.1	iteration step size
K	4	width of transversal brightness measurement
k+	[1:3]	length of brightness measurement in front of leg tip
k_p-	var	brightness readings from leg tip to template center for leg p
l_p	var	length of leg p
H_{max}	var (256)	maximum brightness value in current image
H_{th}	$\frac{H_{max}}{20}$	brightness threshold for force generation
s_{prot}	5	strength factor protrusion force
s_{ret}	15	strength factor retraction force
s_{ortho}	1	strength factor orthogonal force
s_{rot}	0.4	strength factor rotation force
s_{cl}	3	strength factor longitudinal force on cell body
λ_{ortho}	2	orthogonal friction
λ_l	2	longitudinal friction
λ_{rot}	1.43	rotation friction
ϵ_{ortho}	0.2	orthogonal fluctuation strength
ϵ_l	0.2	longitudinal fluctuation strength
ϵ_{rot}	0.2	rotation fluctuation strength
σ	4	shape of distance weight function
a	2.5	strength of distance weight function

Table 1.2: Table of parameters used for all rigid template applications of this chapter.

proceeded to a 8-bit greyscale version and finally tested a stack of 8-bit greyscale images. All of these test images were derived from original time-lapse images and have been modified with *ImageJ* and/or *The Gimp* as desired. Modifications included, for instance, extracting a "Region of Interest" (RoI) with a single cell and downgrading color resolution to binary. The parameters used are displayed in table 1.2.

Single binary image (proof of concept) (fig. 1.4)

First, we show that the program can track a cell in the binary version of an image. This is the most simple scenario, because calculated forces will be either high or zero making especially edge finding very simple.

The images in fig.1.4 show the situation at every 20th iteration of a full 140 iterations run. The process of protrusion/retraction manages to detect the dimensions of the cell well, and the final fit of the edges is good, the center of the virtual cell stays in the middle of the original as intended. This is because with only a single pixel value (ie. equal brightness all around), force equilibrium at

the center of this brightness spot is only reached, if it is symmetrically shaped as in the case here. Thus, force calculation and fitting process work as intended.

Additionally, we can also see that the fit is already sufficient at images four or five, it is thus possible to implement a stop condition and/or end time to shorten the program runtime for this tracking scenario.

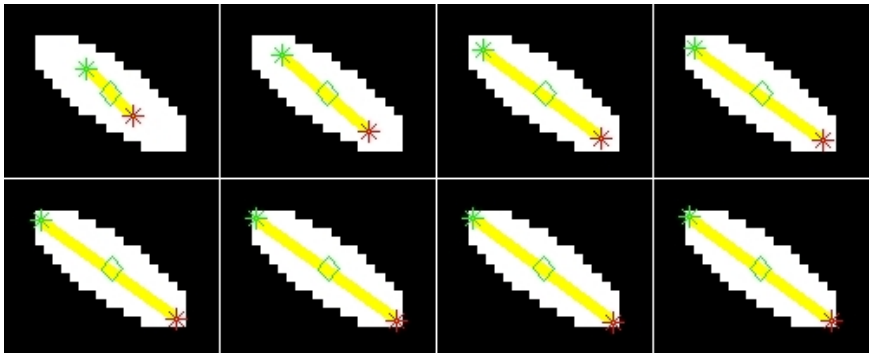

Figure 1.4: Image series of fitting a single binary image of a cell using the rigid tracking model. The cell is displayed white with pixel values of 255, the background is black with pixel values of 0. 20 iterations have been calculated between each picture. Green diamonds mark template center. Green and red asterisk mark tips of legs one and two, respectively. Legs are depicted by yellow lines.

Single greyscale cell (fig. 1.5)

A greyscale image of an asymmetrical target cell was chosen for the next test. Edge detection will be more difficult, but good greyscale tracking is important for analysis of real images. Furthermore, the asymmetric shape of the target cell poses additional problems to the rigid version of the fitting program.

When considering greyscale images, the above mentioned brightness threshold H_{th} (see Section 1.3) becomes important. This parameter defines the necessary minimum brightness of pixels to still be accounted for as part of a cell. In effect, if there are smooth transitions or smeared edges from cell to background, it will affect at which point a protrusion (or retraction) stops. Setting this too low will lead to overshooting, while setting it too high will result in undershooting. This holds true for both protrusion and retraction.

As a result of the *startpos* subroutine, the virtual cell starts with its center at the brightest pixel and an orientation that yields the highest overall brightness. Over the course of 150 iterations the virtual cell enlarges (or shrinks) and rotates to fit the displayed cell. Looking at figure 1.5, the asymmetric shape of the target cell with a prominent protrusion leads to a template fit that is similarly

asymmetrical, as desired. With a higher threshold value H_{th} the protrusion can be ignored if desired, this yields a final fit similar to the one in the second picture in the top row.

The position of the virtual template center remains in the bright region, but leaves the brightest spot. This is because the protrusion at the bottom is pulling the center downwards and influences the angle of the fit. The program has to establish a state that satisfies all requirements as good as possible and the final position reflects this. Indeed, the shape of the target cell is reproduced well, with a cell center in the bright region, a short upper leg and a long lower leg depicting the protrusion.

With a proper set of parameters, this solution is stable and unique. As mentioned, changing the threshold value leads to the protrusion being ignored, making it obvious that results and stability of the solution entirely depend on parameter sets.

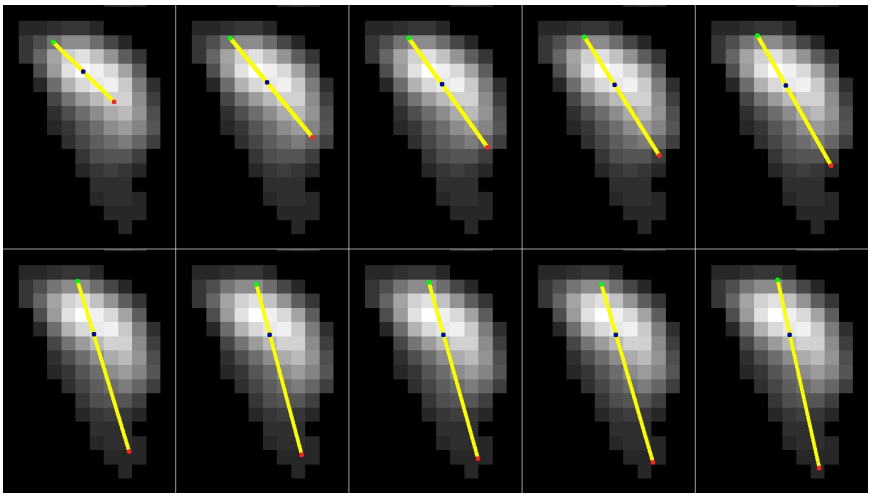

Figure 1.5: Image series of fitting a single greyscale image of a cell over 150 iterations using the rigid template. Range of pixel values 0-255 (black to white). Time between images is 15 iterations. Blue dots mark template center. Green and red dots mark tips of leg one and two, respectively. Yellow lines indicate legs.

Greyscale consecutive images (fig. 1.6)

The next step was to determine whether the program can track a cell over more than one image. To test this, a cell was selected and a RoI containing it was cut out on two consecutive images. In fig.1.6 the top left picture displays the last position of the virtual template cell on the first of the two images, the picture

next to it shows the state after the virtual template cell was transfered to the second image and a single iteration has been calculated. Proceeding towards the right and down we show the beginning of the tracking procedure establishing the new position of the cell. The bottom right picture displays the final position of the virtual cell at the end of the tracking process. Again, the asymmetrical shape of the target cell is reflected, as cell center, forward and rear leg all depict the target cell quite well. Regarding edge finding, tip position of both legs appears sufficient. This conclusion seems justified all the more as it has to be kept in mind that, when tracking a cell over time, its brightness may fluctuate, making it difficult, if not impossible, to set a unique brightness threshold H_{th} that guarantees a perfect edge fit in every image.

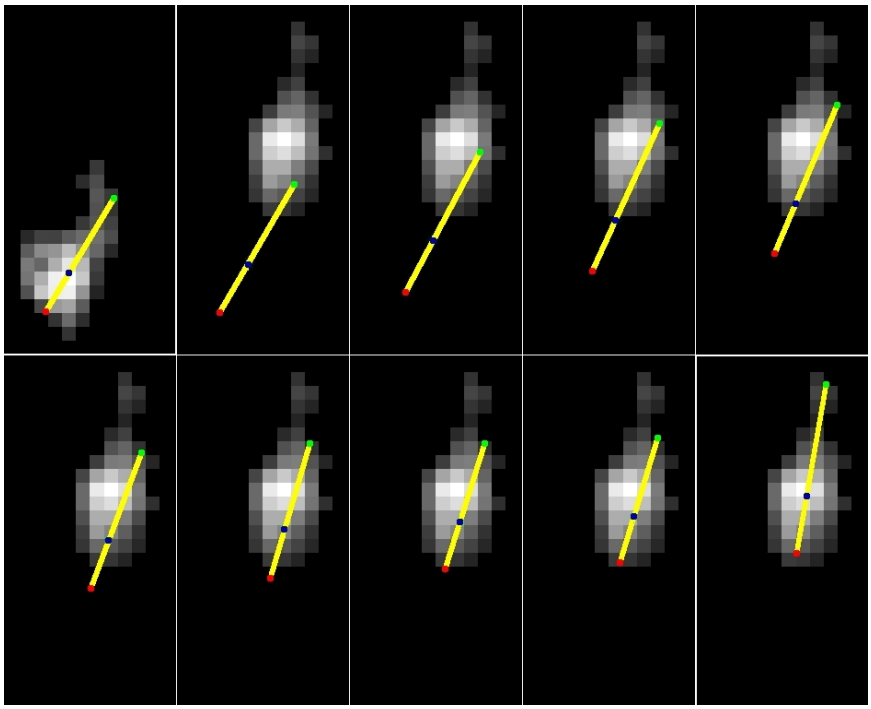

Figure 1.6: Tracking of a given cell over two images using the rigid template. Pixel brightness values between 0-255 (black to white). Blue dots mark template center. Green and red dots mark tips of leg one and two, respectively. Yellow lines indicate legs. **top left:** final position of fitting of the rigid template on the first image. **2nd from top left:** template on second image after transfer of final position from first image and calculation of a single iteration. **towards right and down**: tracking of image 2 (image interval: 20 iterations). **bottom right**: tracking skipped to final position on image 2 (120 iterations skipped, but final position reached sooner.).

1.4 "Hinged" fitting model

In figures 1.5 and 1.6 it can be easily noticed that the straight rod template does not always fit the real cell very well. It would be advantageous to have the possibility of kinks and angles in the virtual cell to account for shifting and changes of form in the original cell. This may not be necessary for every cell and is indeed pointless for very rigid (non-deforming) cells.

Cells of the type discussed here extend and retract one or more protrusions regularly, show elongation in relation to migration speed and are generally changing shape in a way that is not accommodated by the model discussed above.

To increase fit quality, we therefore have changed the fitting program such that the front and rear legs may take different angles. Thus, the cell center basically acts as a hinge around which both legs can pivot. fig.1.7 shows the model scheme in more detail.

1.4.1 Function and algorithms

The differences of the hinged as compared to the rigid template include torque calculation, as well as cell displacement, both due to having different angles for front and rear legs. Protrusion and retraction are only changed in so far as their directions change respective to the direction of the legs, but their calculations remain exactly the same as for the rigid template.

Whereas there was a single angle α before, we now introduce two separate angles α_1 and α_2 for the respective legs. All orthogonal forces are calculated as before, but this time both angles have to be taken into account. Additionally, due to the higher template freedom, its behavior is changed for center orthogonal displacement. Before, the angle and leg lengths were fixed so that the whole template was shifted. Now, because legs are independent, angles and lengths can be released and instead we fix leg tip positions. Thus, only the center displaces during this step, leading to template bending as opposed to whole template shifts in the rigid model. As generalization of eq.1.1 we now have:

$$\begin{pmatrix} x_p \\ y_p \end{pmatrix} = \begin{pmatrix} x \\ y \end{pmatrix} \pm l_p \begin{pmatrix} cos(\alpha_p) \\ sin(\alpha_p) \end{pmatrix}. \tag{1.16}$$

α_p being the direction of the respective leg p.

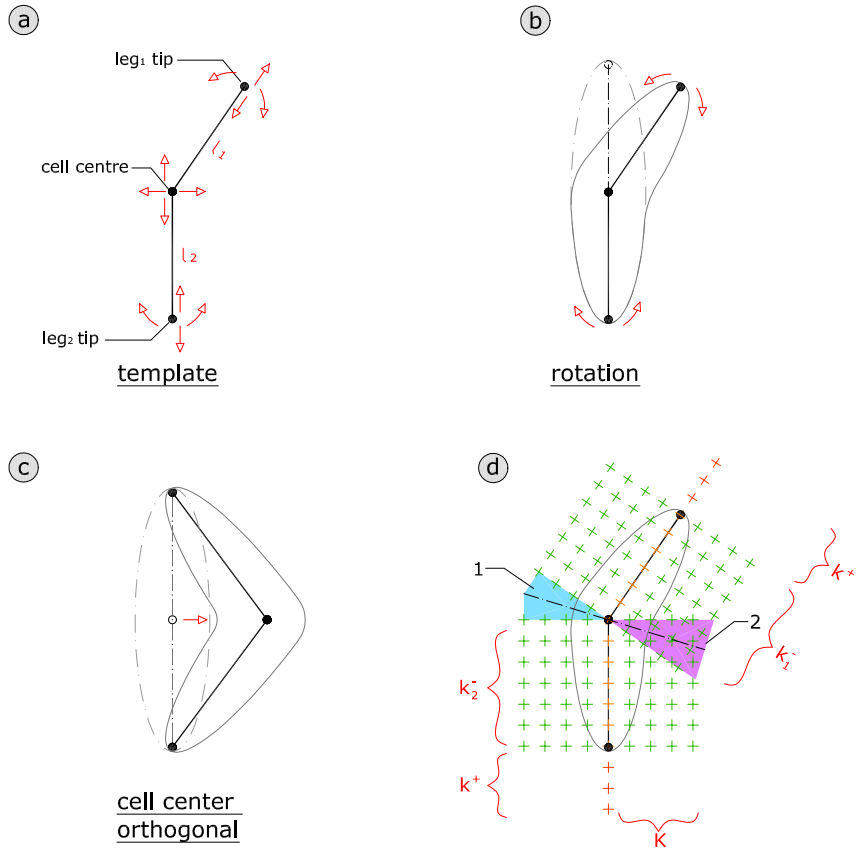

Figure 1.7: Schematic overview of the hinged template. Only differences of template motions relative to the rigid version are displayed, namely the ability to rotate a single leg independently from the other and displacement of cell center in orthogonal direction. **(a)** Overview of possible template adaptions for the hinged template. **(b)** Example of rotation of a single leg. The tip of one leg is rotated, keeping the rest of the template fixed. Rotation does not affect leg length. **(c)** Illustration of template changes due to cell center displacement. With the introduction of a hinge the template center can move independently now. Leg tip positions are fixed and, thus, leg lengths change during this adaption process. **(d)** Difference in brightness readings as compared to the rigid model. Areas 1 and 2 show the consequences of the hinged model. Due to the perpendicular orientation of reading points to template legs, area 1 contains no brightness reading points, while there are reading points stacking on the same pixels in area 2. This asymmetry in brightness readings is countered by the introduction of additional reading points according to the angle bisector of the two areas (striped line). Constant and variable names as before (fig.1.1)

Protrusion & Retraction

As mentioned, the only difference in the program concerning protrusion and retraction is that front and rear legs will extend in different directions. This changes only the calculation for the final (x, y)-position of the tip. Analogous to the rigid model, center position and angle are fixed while leg length is adjusted according to:

$$\begin{aligned} dl_p &= F_{prot,p}\, dt + \epsilon\, \xi\, \sqrt{dt} \\ dl_p &= F_{ret,p}\, dt + \epsilon\, \xi\, \sqrt{dt}. \end{aligned} \tag{1.17}$$

Leg tip positions are updated using eq.1.16 before calculating orthogonal forces.

Orthogonal Forces and Torque

The most profound change of the hinged version of the program concerns calculation of orthogonal forces, since there are two different orthogonal directions now. A torque will have to be calculated for both legs separately.
The torque equations are thus duplicated from eqs.1.8, 1.10 and 1.11

$$g(H) = H^2 \tag{1.18}$$

$$\begin{aligned} F_{orth,p,i} &= s_{orth} \frac{\sum_{j=1}^{K} W_j\, g(H_{p,i,j})}{\sum_{j=1}^{K} g(H_{p,i,j})} \\ \Omega_p = \sum_i \omega_{p,i} &= s_{rot} \sum_i d_i\, F_{orth,p,i} \\ d\alpha_p &= (\frac{1}{\lambda_{rot}})\, \Omega_p + \epsilon_{rot}\, \xi\, \sqrt{dt} \end{aligned} \tag{1.19}$$

with p denoting the respective leg, i the intersection of an orthogonal line on template leg p and j the points on the orthogonal line intersecting at i. Leg tip positions are updated again at this point before continuing.

Displacement of Cell Center

For longitudinal displacement, depending on which side has the stronger protrusion force, the cell center will move either in the direction of leg_1 or leg_2. For orthogonal movement, however, there is one issue that arises. If we look at fig.1.7 we can see that next to the cell center there is no regular brightness reading in area **1**, while there

is a crossover of readings in area **2**. For torque calculation this is not an issue, since brightness is weighted by distance d_i along the cell axis, which is zero for intersections going through the cell center. However, it is important for correct determination of cell center displacement. Thus, a new reading is introduced at the mean angle of the two angles $\beta_1 = \alpha_1 + \frac{\pi}{2}$ and $\beta_2 = \alpha_2 + \frac{\pi}{2}$, namely

$$\beta_m = \frac{\beta_1 + \beta_2}{2}. \tag{1.20}$$

this is worked into the formula by taking the mean of the sum of brightness values of all three lines intersecting at the cell center (compare fig.1.7d):

$$H_i^{\beta_1,\beta_2,\beta_m} = \frac{\sum H_{\beta_1,i,j} + \sum H_{\beta_2,i,j} + \sum H_{\beta_m,i,j}}{3} \quad | \ [i = 0] \tag{1.21}$$

All other parts of the formula are as described for the single angle version.

Next, direction of transversal displacement is determined by taking the mean of α_1 and α_2, weighted by their respective lengths.

$$\beta = \frac{l_1\,\alpha_1 + l_2\,\alpha_2}{l_1 + l_2} \tag{1.22}$$

Final formulas for longitudinal displacement in the dual angle version are thus

$$\begin{aligned} dx &= (\frac{1}{\lambda_{cl}})\, F_{cl}\, cos(\alpha_p) + \epsilon_{cl}\, \xi\, \sqrt{dt} \\ dy &= (\frac{1}{\lambda_{cl}})\, F_{cl}\, sin(\alpha_p) + \epsilon_{cl}\, \xi\, \sqrt{dt} \end{aligned} \tag{1.23}$$

$$p = \begin{cases} 1 & , \text{ if } F_{prot,1} > F_{prot,2} \\ 2 & , \text{ if } F_{prot,1} < F_{prot,2} \end{cases}$$

For transversal displacement the respective formulas are

$$H_i = \begin{cases} H_{\alpha 1,i,j} & , i > 0 \\ H_i^{\beta_1,\beta_2,\beta_m} & , i = 0 \\ H_{\alpha 2,i,j} & , i < 0 \end{cases} \tag{1.24}$$

$$F_{orth,i} = s_{orth} \frac{\sum_{j=1}^{K} W_j \, H_{i,j}^2}{\sum_{j=1}^{K} H_{i,j}^2} \tag{1.25}$$

$$F_{co} = \sum_i F_{orth,i} \tag{1.26}$$

$$dx = (\frac{1}{\lambda_{co}}) \, F_{co} \, cos(\beta) + \epsilon_{co} \, \xi \, \sqrt{dt}$$

$$dy = (\frac{1}{\lambda_{co}}) \, F_{co} \, sin(\beta) + \epsilon_{co} \, \xi \, \sqrt{dt} \tag{1.27}$$

1.4.2 Results

Parameters used:

parameter	value	description
t_{end}	15	maximum iteration time
dt	0.1	iteration time step size
K	5	width of transversal brightness measurement
k+	[1:4]	length of brightness measurement in front of leg tip
H_{max}	var (256)	maximum brightness value in current image
H_{th}	$\frac{H_{max}}{15}$	brightness threshold for force generation
s_{prot}	25	strength factor protrusion force
s_{ret}	10	strength factor retraction force
s_{ortho}	1	strength factor orthogonal force
s_{rot}	0.1	strength factor rotation force
s_{cl}	4	strength factor longitudinal force on cell body
λ_{ortho}	10	orthogonal friction
λ_l	2	longitudinal friction
λ_{rot}	10	rotation friction
ϵ_{ortho}	0.1	orthogonal fluctuation strength
ϵ_l	0.1	longitudinal fluctuation strength
ϵ_{rot}	0.1	rotation fluctuation strength
ϵ_{co}	0.1	orthogonal fluctuation strength cell body
ϵ_{cl}	0.1	longitudinal fluctuation strength cell body
σ	4	shape of distance weight function
a	2.5	strength of distance weight function

Table 1.3: Table of parameters used for all hinged template runs of this chapter. H_{max} is a variable value depending on the give image, however for all presented results this has been scaled to 256. This supports consistency of tracking on different images, as well as parameter evaluation.

Single greyscale cell (fig.1.8)

First, we tracked the same image as in figure 1.5. Using the hinged template model the shape of the target cell is reflected much better than for the rigid version. In contrast to fig.1.5 the cell center fit is much improved. This is obviously because of the dual axis allowing a kink. Overall orientation of a given cell is also displayed much better, the orientation of the forward leg reflects the current cell orientation, while the orientation of the rear leg reflects the previous orientation. This way, directional changes of target cells are reproduced nicely.

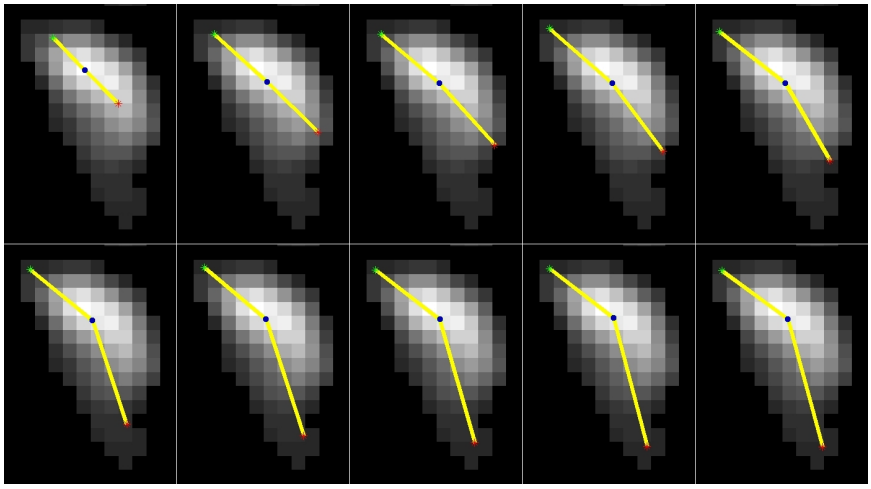

Figure 1.8: Fitting of a greyscale image using the hinged template. Pixel brightness values between 0-255 (black to white). Blue dots mark template center. Green and red dots mark tips of leg one and two, respectively. Yellow lines indicate legs. 20 iterations between images. For comparison of the same image fitted with the rigid template see fig.1.5.

Consecutive greyscale images (fig.1.9)

The next step was to observe consecutive images and for this we have chosen the same greyscale image as for the rigid template (fig.1.6). We again start at the final position of the template in the first image and transpose this template layout to the second image. Noticeably, transition from one image to the next is working smoothly for the hinged template version of the program. Furthermore, we see that cell centers fit well, as well as leg orientation and length fits are improved over the rigid template approach. The lower leg extends from the edge of the real cell's protrusion up to the brightness center of the real cell

containing the template center. In the same manner, the upper leg extends from the opposite edge of the template to the brightness center of the real cell.

Overall, it appears that tracking of consecutive images is working well and we continue on to the real task: tracking of a larger stack of images, ie. a movie of a migrating cell.

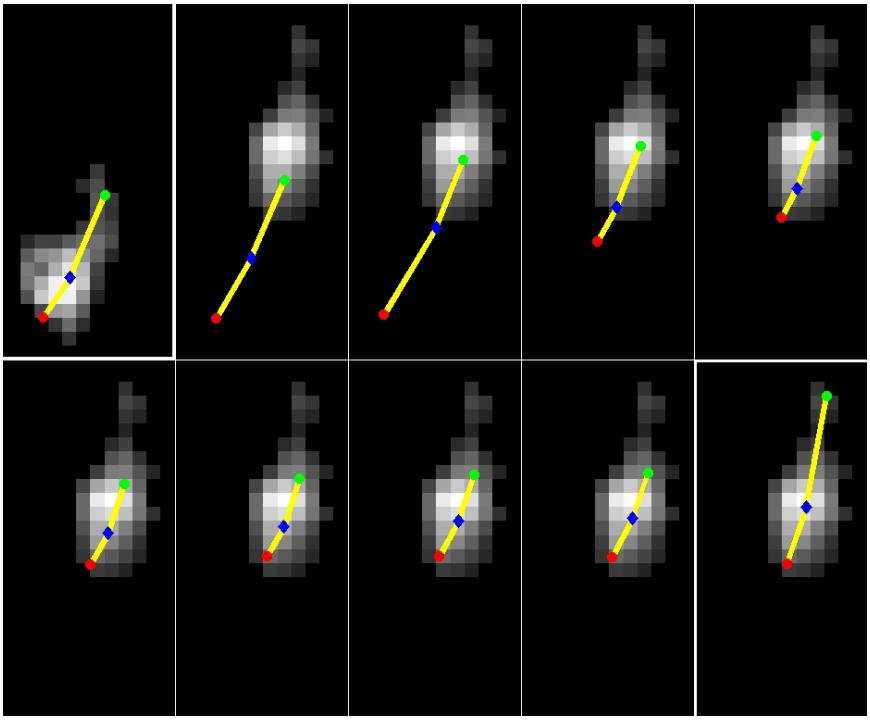

Figure 1.9: Fitting of the same cell on two consecutive images with the hinged template. Pixel values between 0-255 (black to white). Blue dots mark template center. Green and red dots mark tips of leg one and two, respectively. Yellow lines indicate legs. The images are the same as fig.1.6. **A:** Final template fit in first image. **B:** template on second image after transfer of final position from first image and calculation of a single iteration. **C-I:** fitting process, 20 iterations between images. **J:** 120 iterations skipped. Final position of hinged template in second image.

Cell path track (fig.1.10)

Figure 1.10 shows a cell track over 26 images. The target cell changes migration speed and direction a few times over the course of tracking, making this a good test object. Our virtual cell template manages to stay on target on every image and is indeed able to consistently and correctly track protrusion length and orientation, as well as cell center position.

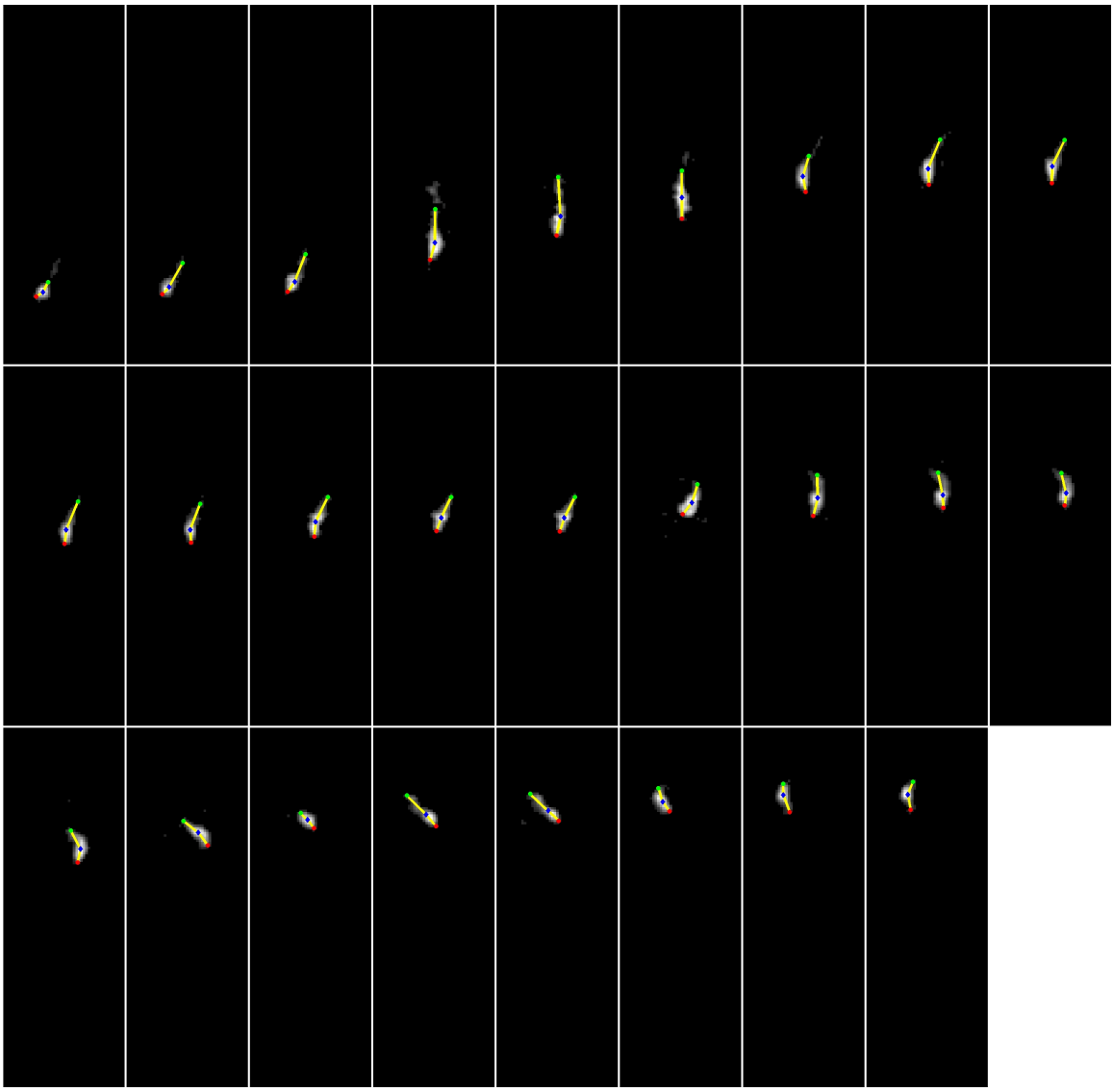

Figure 1.10: Tracking of a cell over 26 images using the hinged template. Pixel values range from 0-255 (black to white). Blue dots mark template center. Green and red dots mark tips of leg one and two, respectively. Yellow lines indicate legs. Each image depicts the resulting template after fitting of this particular image. 200 iterations per image.

1.5 Discussion and outlook

We have shown that the tracking program works well on single binary and greyscale images and is also able to track a cell across consecutive images (image stacks). While both modes (rigid and hinged) yield good results, comparison of figures 1.5 and 1.8 makes it clear that the hinged template results in a better fit for deforming cells, as

expected. It is obvious that for deformable cells, like interneuronal precursor cells of the type investigated in this work, the hinged mode is to be preferred, and will thus be exclusively used for the rest of this work.

When using this program it should be noticed that tracking results will always be based on the result of the previous image (the history of the track). In effect, due to the equivalency of legs on any given (first) image there are (at least) two solutions. (Equivalency of legs means that neither leg is predefined as front or rear leg, but instead both legs are considered equal and can be leading or trailing.) Thus, the *startpos* subroutine can yield two interchangeable results. The first result will be the best fit the template can adapt to and the second will be that same fit with exchanged legs. This is not an inherent flaw of the program, but instead stems from the equivalency of legs. The reason we have implemented it this way is that it enables the program to correctly track cells that start to move backwards without turning.

Stability of tracking also raises the topic of stop conditions of the tracking iteration process. Generally, a stop condition cannot improve tracking results, but only shorten program runtime. For the hinged mode three different entities need to fulfill any given predefined stop condition. These are the two legs and the cell center. Ideally, a program stop must occur only if all three of these entities are in their final (optimal) position. Furthermore, depending on target cell form it may happen that one leg is stuck in a non-optimal position for a time until the fluctuation becomes large enough to overcome this image force "hill" and only then can this leg acquire its final (optimal) position (see fig.1.11). In a case like this a premature stop may occur. Because of this and the fact that checking fulfillment of stop conditions increases runtime itself, no stop conditions, apart from a suitably chosen maximum number of iterations, have been introduced.

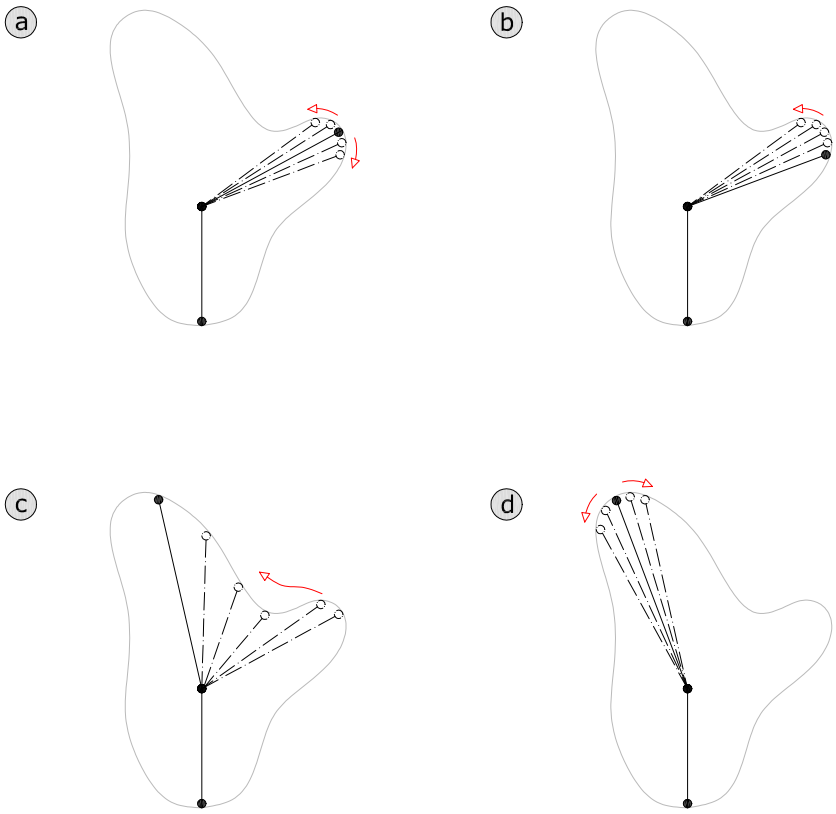

Figure 1.11: Example of the issue of stop conditions. The leg proceeds into a small bulge instead of the real protrusion (**a**) and remains there (**b**), until the random component of the algorithm generates a large enough fluctuation and overcomes the image force "hill" (**c**) so that the leg can advance into its final position (**d**).

Chapter 2

Modeling an interneuronal precursor cell

2.1 Introduction

When observing GFP-stained precursor cells of GABAergic interneurons migrating in developing cerebellum of P8 mice, several interesting properties can be found. These include prominent protrusions, path reversal, clustering and movements reminiscent of chain-migration. Fig.2.1 includes examples of regularly observed protrusions. These are presumed to be involved in migration, detection of surrounding structures, extracellular matrix, and others [23]. Figures 2.2a and 2.2b show a feature which has been termed "path reversal" by us. Regularly it can be observed that cells move in a certain direction, stop and, after a short time, start migrating backwards exactly the same path. Whether this change of direction is due to a 180° turn of the cell or an internal reorganization, inducing the rear part of the cell to become the front, cannot be definitely determined from the available image resolution. However, observations imply the latter alternative. Path lengths of such sections vary, but usually exceed the length of protrusions, so it can be proposed that this reversal is not due to a cell appendage that is still attached to a given structure and "pulls" the body backwards passively after detachment of the front protrusion. It rather can be assumed that new protrusions are activated at the rear. An underlying cause for this kind of directional behaviour would be the existence of structures that the cell uses to move along. It then also seems that this presumed structure does not impart a fixed predefined migration direction.

Another observation is clustering and chain-migration, which often occur together

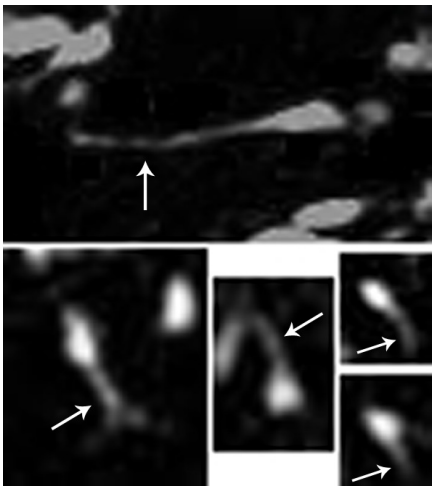

Figure 2.1: Examples of regularly observed protrusions (arrows) in Pax2-GFP stained time-lapse images of cerebellar preparations of P8 mice. Regions of interested extracted from complete images.

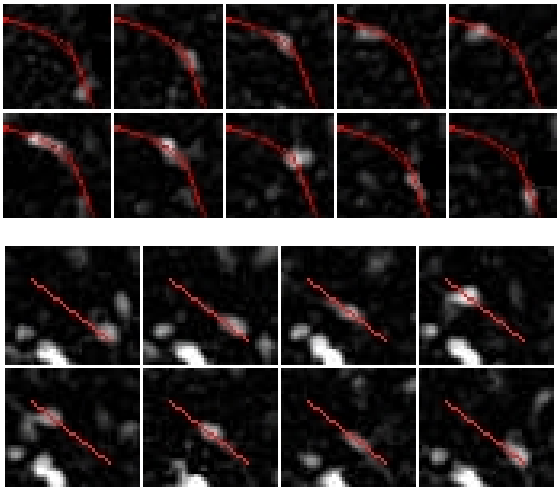

Figure 2.2: Occurrences of path reversal in Pax2-GFP stained time-lapse images of cerebellar preparations of P8 mice. Regions of interested extracted from complete images. Red line marks cell tracks.

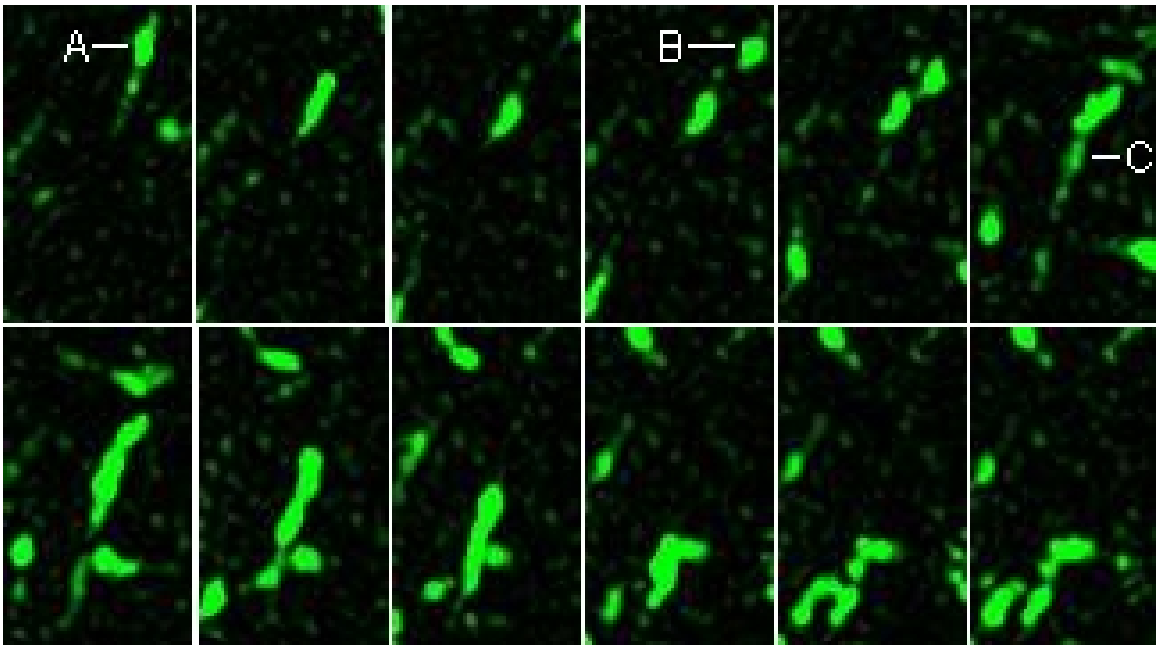

Figure 2.3: Example of clustering and chain migration. The first cell (A) stops migrating and remains in place. After about 3 hours a second cell (B) moves into it from the top right. Simultaneously, a third cell (C) appears in the focus area, seemingly from within the slice. Once clustered, the three cells move together in a chain formation, before splitting up again (time span of chain migration is about 4 hours). Time span from first to last image is about 9 hours.

(fig.2.3). The usual appearance is that a cell stops its migration and remains seated until a second cell migrates right into it, then both cell start migrating in a chain-like formation. Sometimes, the second cell will not trigger the chain-migration, but they both remain until a third cell migrates into the cluster. A higher number than that has not been observed in the movies available to us. Due to other research targets and tracking difficulties in dealing with chain migration, we will not explore this specific behaviour in more detail.

In a previous work [19] we have shown that cell tracks usually contain relatively straight sections (see figs.2.4a and 2.4b). These sections often continue one another even though they are derived from different cell tracks. Together, the above observations strongly suggest the existence of leading structures within the developing cerebellum.

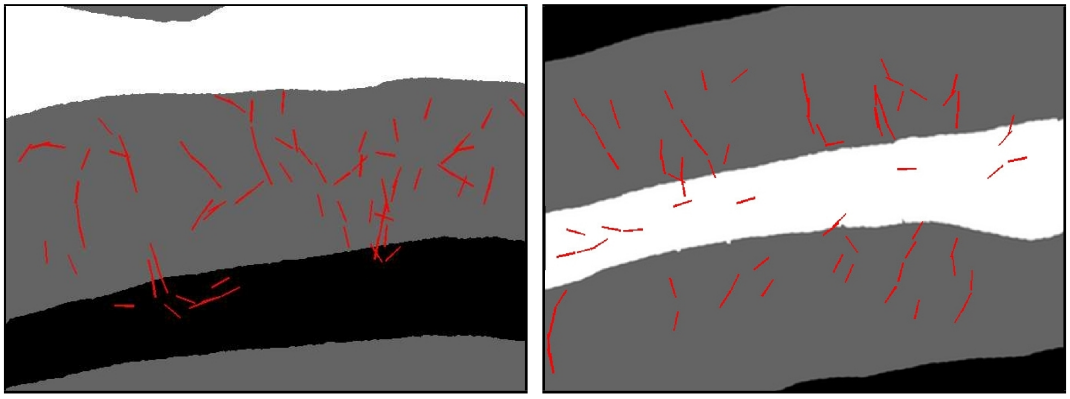

(a) S007 (b) S008

Figure 2.4: Tissue masks of the first images of two time-lapse movies (image stacks). Straight path sections marked by red lines. Straight path sections were selected by small angular changes of migration direction and a migration speed above a set minimum, both over a persistence period of at least 5 images (pictures taken from diploma thesis [19]).

Consequently, our model of an interneuronal precursor cell consists of two major components, namely protrusive activity (termed "protrusivity" by us) and guiding structures. In general, the cell is represented by two vectors called **W** and **P**, depicting the cell's protrusive activity and the cell body's long axis, respectively (for a schematic overview of the model vectors and reciprocal influences of important parameters see fig.2.5(a)&(b)). The first component is modeling of protrusivity, represented by a vector (**W**) that can rotate around the cell body and elongate/shrink. This vector is used in cell migration by influencing the cell's polarity vector (**P**) and also in detection of guiding structures. Furthermore, there are two distinct methods of incorporating

the protrusivity vector, which, due to the way they work into cell movement, we call parity 1 and 2. At parity 1 the cell is "unidirectional", ie. it has a defined front and rear, always moving forward with its front. To move backwards, the cell's polarity vector **P** has to rotate by 180°. For the parity 2 case, this definition is removed, effectively allowing the cell to move forwards and backwards without having to turn. This is probably the more biologically fitting case for our specific cell type and is what will mainly be discussed. A more in-depth explanation of the two modes is given in section 2.3.4.

The second component is influence of a structure, like an axon of a Purkinje cell or a climbing fiber, which is used to guide the cell. This influence takes two forms, the first is what we call alignment or attraction of the cell towards the structure. However, a simple attraction towards the structure will only result in the cell moving into the structure's vicinity, but will not support directional movement along the given structure. In effect, attraction alone will lead to something resembling a 1-dimensional random walk and cells will not displace very far from the point where they first made contact with the structure. To counter this, directional guidance is introduced in the form of a guidance function that results in cell movement along the structure. The way this influence is modeled, it does not privilege any of the two possible directions, but enhances an already established cell polarity, thus leading to higher persistence of migration and consistent displacement from the origin.

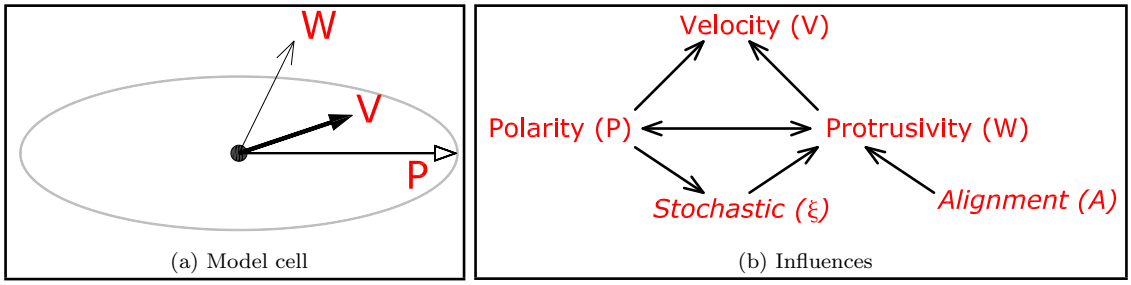

Figure 2.5: **(a)** Schematic of a model cell. Oval cell border just for illustration purposes. Polarity vector **P** depicts the model cells length axis. Protrusivity vector **W** depicts protrusive activity within the model cell. Velocity vector **V** depicts resulting movement of the model cell. **(b)** Reciprocal influences of governing parameters: **V** velocity vector, **W** protrusivity vector, **P** polarity vector, ξ stochastic component of the model, **A** structural influences.

2.2 Method: orientation analysis

In this work we employ orientation analysis calculations. Autocosine and Autoorientation deal with deviation of a single vector to itself at a time delay, equivalent to autocorrelation analysis, while crosscosine and crossorientation analysis compare different vectors at time delays, equivalent to crosscorrelation analysis. We will explain these tools in this section.

Autocosine (and equivalently autosine) analysis calculates the cosine (sine) of a vector with itself at a delay of τ up to a specified τ_{max}. In this regard, it is similar to correlation analysis. As in standard cosine calculation the cosine is 1 if the angle of compared vectors matches (0°), it goes towards zero as the angle approaches 90° and returns -1 for angles of 180°. Thus, the autocosine is a measure of relative vector direction and persistence of direction. Figure 2.6(a) shows the angles of an exemplary unit vector **W** (blue) over time, whose direction stochastically fluctuates around a pivoting unit vector **V** (red) (displaying a sine wave with an amplitude $A = \frac{\pi}{3}$ and period $P = 2\pi$) with a mean adjustment time of $T_a = 2$. (b) displays the corresponding autocosine. For a τ of zero the autocosine is always 1, so the graph always starts at [0,1]. Equivalent to autcorrelation analysis, the decline depicts directional persistence times and additional peaks can indicate corresponding periodicities. In (b) the trough at $\tau \approx 3.1$ shows the half-period and the peak at $\tau \approx 6.2$ corresponds to the full period, reflecting the period of the leading vector **V**. (c) displays the autoorientation result of **W**. The x-axis corresponds to mean sine values and the y-axis corresponds to mean cosine values. Time delays τ are displayed as diamond shaped marks connected by a line. Each diamond depicts a time step $d\tau = 0.2$ (for readability only every second time step is depicted in (c) and (e)). The starting point of $\tau = 0$ is at mean cosine of 1. This is obviously given as the autocosine at no time deviation will always be 1 and the autosine will always be 0. Following the graph we can see how the vector behaves in regard to previous times. Amplitude along the y-axis indicates correspondence of vectors (cosine of vector angles), while amplitude on the x-axis indicates deviation towards the left or right (sine of the vector angles). In this particular case we see that orientation correspondence is diminished the longer the time delay (each diamond representing one time step of delay) and that the vector deviates towards negative angles (ie. to the right from the original orientation) compared to the leading vector **V**.

(d) displays a crosscosine plot where we again compare the vectors **W** and **V** depicted in (a). Crosscosine analysis displays a clear positive maximum at negative τ

and a clear negative correlation for positive τ. Since $\mathbf{W}$ follows $\mathbf{V}$ with a time delay, this delay is reflected in the crosscosine analysis. Higher/lower adjustment times lead to longer/shorter delays τ, respectively.

Finally, (e) displays a crossorientation plot. Similar to the autoorientation graph x-axis displays the mean crosssine and y-axis depicts the mean crosscosine. In the plot a τ of zero is marked by a filled circle, while stars are used for negative time delays and diamonds are used for positive delays. Again, for readability only every second time step was used, leading to $d\tau = 0.2$) between marks. Interpretation of the graph follows the one for autoorientation analysis. High amplitudes along the y-axis correspond to conforming angles and amplitudes on the x-axis display left and right deviation. Equivalent to the crosscosine plot, highest/lowest correlation (maximal/minimal y-value) is found, respectively, for a negative/positive delay corresponding to the chosen adjustment time T_a. Additionally, we find that for negative τ (stars) the following vector ($\mathbf{W}$) deviates towards negative angles (to the right) and for positive τ it deviates towards positive angles (to the left) compared to the leading vector ($\mathbf{V}$).

2.3 Function and algorithms

To begin with, we will look at the general movement algorithms of the simulation including influence of the protrusivity. Afterwards, the attraction and guidance effects of the structure will be explained. We end by integrating both aspects.

2.3.1 Cell migration

Cells are modeled having a certain preferred mean speed s_0, directly influenced by polarity vector $\mathbf{P}$, which in turn is influenced by protrusivity vector $\mathbf{W}$. Length of the polarity vector ($p = |P|$) influences cell speed and elongation, while orientation $\hat{(\mathbf{P})} = \frac{\mathbf{P}}{p}$ governs movement direction in conjunction with protrusivity ($\mathbf{W}$). The resulting migration velocity V is calculated as the projection of the protrusivity onto the polarity vector and its 90° to the left rotated counterpart $\mathbf{P}^{\perp}$, multiplied by the

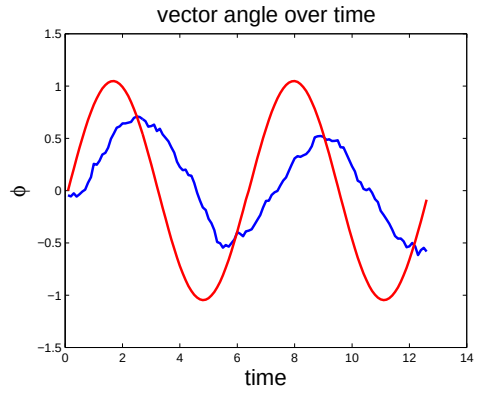

(a) Angle over time

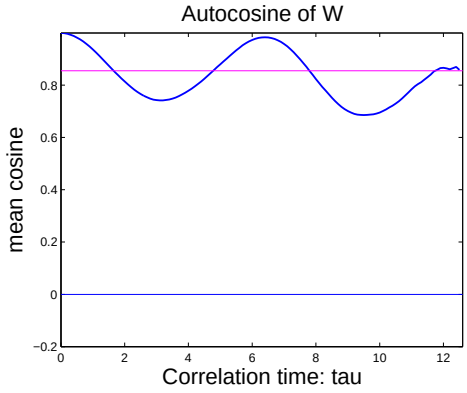

(b) Autocosine

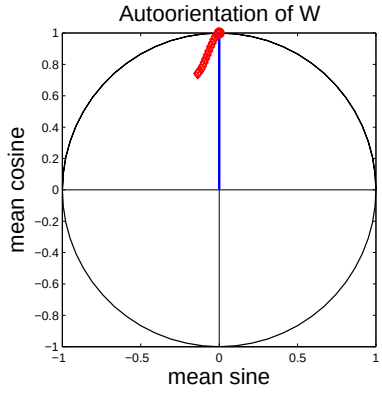

(c) Autoorientation

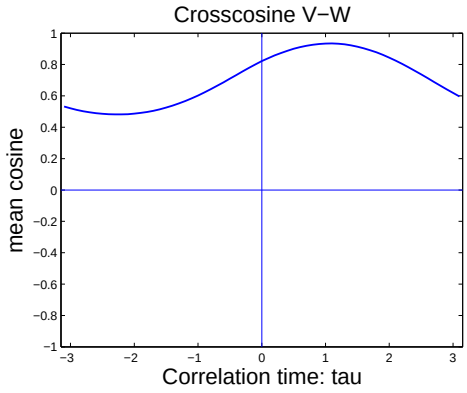

(d) Crosscosine

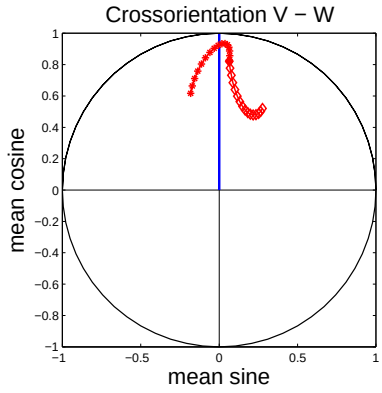

(e) Crossorientation

Figure 2.6: **(a)** Angle of an exemplary vector **W** (blue) over time. This vector follows a second vector **V** (red) with an adjustment time of 2 minutes (20 iterations). The vector **V** describes a periodic sine wave between $\frac{\pi}{3}$ to $\frac{-\pi}{3}$. **(b)** Autocosine of **W**. Magenta lines display significance border. **(c)** Autoorientation of **W**. **(d)** Crosscosine of **V**-**W**. **(e)** Crossorientation of **V**-**W**. Stars mark negative time delays, diamonds mark positive time delays and filled circle marks $\tau = 0$.

preferred mean speed s_0.

$$\begin{aligned} \mathbf{P}^{\perp} &= \begin{pmatrix} -\mathbf{P}_y \\ \mathbf{P}_x \end{pmatrix} \\ w_{cos} &= \frac{\mathbf{W} \cdot \mathbf{P}}{p} \qquad (2.1) \\ w_{sin} &= \frac{\mathbf{W} \cdot \mathbf{P}^{\perp}}{p} * w_{cos} \qquad (2.2) \\ \mathbf{V} &= s_0(w_{cos}\,\mathbf{P} + v_c\, w_{sin}\,\mathbf{P}^{\perp}) \qquad (2.3) \end{aligned}$$

v_c (where $0 < v_c < 1$) is a limiting factor for influence of the perpendicular movement component on model cell polarity rotation. Thus, the resulting movement is the amalgam of conformity of polarity and protrusivity. To proceed, we will model the stepwise change of the polarity vector during a small time step dt:

$$\begin{aligned} \mathbf{P}_{t+dt} &= \mathbf{P}_t + d\mathbf{P} \\ d\mathbf{P} &= (\theta - \mathbf{P})\frac{dt}{T_p} \qquad (2.4) \end{aligned}$$

Here θ is defined as

$$\theta = \frac{\hat{\mathbf{W}} \cdot \mathbf{P}}{p}\hat{\mathbf{W}} \qquad (2.5)$$

with the goal to model a bipolar cell. Polarity $\mathbf{P}$ steers towards $\hat{\mathbf{W}}$ ($\hat{\mathbf{W}} = \frac{\mathbf{W}}{w}$ is the unit vector of $\mathbf{W}$ and, thus, direction of protrusivity) in the shortest direction. Meaning that, instead of turning around when protrusivity is located in the back half of the cell body, it can orient polarity along protrusivity and change migration direction, effectively creating a modeled cell with no defined front and rear ends.

2.3.2 Protrusivity vector

As we have explained in the last modeling section (compare fig.2.5b), movement is based on polarity, which is in turn influenced by protrusivity, and so we have to model the protrusivity vector $\mathbf{W}$ next. As the cells we are simulating display prominent protrusions, which are very likely involved in directional guidance and signal processing necessary for migration, there are several factors involved in calculation of the protrusivity vector. The full formula is a stochastic vector differential equation:

$$\begin{aligned} dW = &\frac{1}{2}(1 - \frac{w^2}{w_0^2})\frac{dt}{T_w}\, W \\ &- I_{W,P}\,\frac{dt}{T_m} + \begin{pmatrix} A_h \\ A_v \end{pmatrix} dt \qquad (2.6) \\ &+ (b_r\,\xi_1\,\hat{w} + b_o\,\xi_2\,\hat{w}^{\perp})\sqrt{dt} \end{aligned}$$

The algorithm consists of five parts, for description and values of parameters refer to table 2.1. The first part adjusts the length of the protrusion towards a preferred mean length w_0 with an adjustment time of T_w. T_w itself is variable and depends on magnitude of $\mathbf{P}$ via

$$T_w = T_{w0}(1 + c_w\, p) \tag{2.7}$$

Thus, the adjustment time increases the greater the modulus of $\mathbf{P}$ (p) is, i.e. the more the cell is polarized, i.e. elongated.

The second term is an adjustment term that rotates $\mathbf{W}$ towards $\mathbf{P}$, in other words, it rotates protrusivity towards the cell's polarity axis:

$$I_{WP} = \left(\mathbf{W} \cdot \mathbf{P}^{\perp}\right) (\mathbf{W} \cdot \mathbf{P})\ \hat{\mathbf{W}}^{\perp} \tag{2.8}$$

Due to multiplication of the dot product of protrusivity and polarity with the dot product of protrusivity and perpendicular polarity, this term is zero if $\mathbf{W}$ is parallel or perpendicular to $\mathbf{P}$, and maximal if the angle between the two vectors is equal to $\pm\frac{\pi}{4}$.

This means that a protrusion that is in line with cell polarity and diverts from there will be drawn back towards the cell's polarity, thus increasing persistence of movement. On the other hand, if the protrusion is unaligned with (i.e. perpendicular to) the cell body, this term will not influence its rotation in either direction. This is the main interaction between the two governing vectors $\mathbf{W}$ and $\mathbf{P}$. The third and fourth terms are both alignment terms. These govern attraction towards the structure and guidance along the structure and will be discussed next.

Attraction and guidance

Our model contains two terms describing interaction with extracellular structures. One for attraction towards the structure and one for guidance supplied by the structure. The structure itself is incorporated as the x-axis, meaning that formulas are build in such a way that the cell will always orient towards the base line of the (x,y)-coordinate frame (i.e. y-coordinates equal to zero). Attraction A_v is defined as:

$$A_v = c_v\Big(\frac{0.1}{\pi}\ \arctan(D_y) + \left(sign(D_y)\ |D_y^2|\right)\Big)\ e^{-(\frac{D_y^2}{2\,\sigma^2})} \tag{2.9}$$

with D_y being the distance from the tip of the protrusion to the structure:

$$D_y = W_y + y \tag{2.10}$$

Regarding the form of the attraction function (fig.2.7a), it can be argued that as the cell tip gets closer to the structure, attraction strength increases because the

protrusion can transduce a stronger signal (considering haptotaxis). However, as the cell tip location is even closer, it gains freedom of movement due to fluctuation of the protrusion and, particularly, because the signal gradient becomes zero on top of the structure. As we propose that this gradient is important for directional information, the influence on the cell diminishes the closer it gets. Thus, the attraction function is built such that attraction influences the cell only when within a given critical distance from the structure and increases to a maximum as the cell tip is located at about halfway between the dropoff distance and the structure, then attraction decreases again as the cell moves even closer.

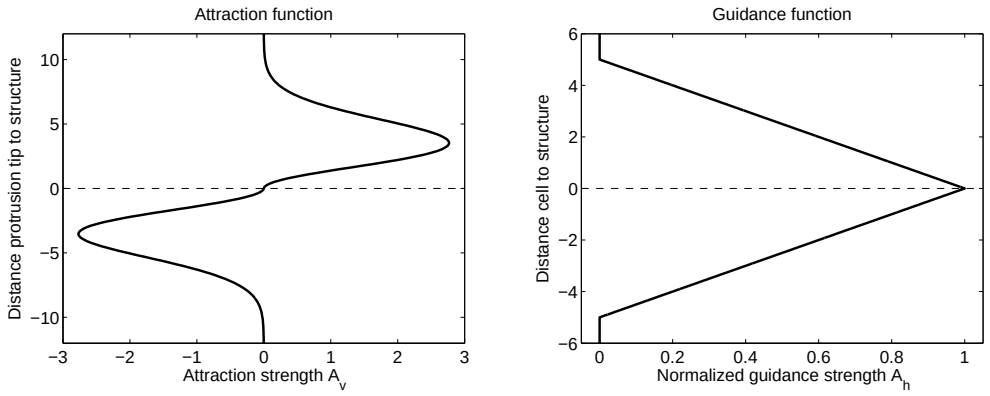

(a) attraction (b) guidance

Figure 2.7: Attraction and guidance strengths as functions of distance between model cell tip/center and structure, respectively. **(a)** The structure attraction function depicts a gradient of structural influence on the cell which the cell follows. As the cell draws close to the structure the protrusion begins to sense the (contact) gradient and moving even closer the influence of the structure increases. However, very close to (on top of) the structure the cell will sense structural contact in every direction, the gradient will be lost and, thus, the influence on the cell will be diminished, leading to freedom of movement. **(b)** Structure guidance is a simple linear function, increasing as the distance between model cell center and structure decreases.

The guidance term is introduced to increase persistence of movement along the structure once the model cell is within a certain range of it. We have chosen to use a simple linear dependency where strength of guidance increases the closer the cell center is to the structure. This is the simplest method and assumes that directional information is directly related to contact of the cell with the structure. The closer the cell is to the structure, the more contact points the possible protrusions can generate

and the higher the directional guidance will be. The guidance term is defined as:

$$A_h = c_h(\max \begin{pmatrix} 1 - \frac{|y|}{5} \\ 0 \end{pmatrix}) sign(W_x) \tag{2.11}$$

And last, the fifth term of protrusivity vector calculation is a standard fluctuation term. Noticeable is that parallel and perpendicular fluctuation strengths b_r and b_o, respectively, are not fixed but depend on the magnitude of $\mathbf{P}$.

$$b_o = \frac{b_0}{1 + c_b\, p} \tag{2.12}$$

$$b_r = \frac{br_0}{1 + c_r\, p} \tag{2.13}$$

As can be seen, both factors become smaller as the magnitude of $\mathbf{P}$ increases. This should effectively increase persistence of movement direction by lowering fluctuations with increased cell polarity.

2.3.3 Remaining calculations

With the above algorithms, the behaviour of the two main components of our simulation model are defined. From these components the values needed to describe all movement steps may be calculated, which, amongst others, include current movement speed s and actual position:

$$s = \sqrt{V_x^2 + V_y^2} \tag{2.14}$$

Increments of positional coordinates (x, y) are obviously proportional to (V_x, V_y), respectively.

$$\begin{aligned} dx &= V_x\, dt \\ dy &= V_y\, dt \end{aligned} \tag{2.15}$$

Finally, magnitude of protrusion and polarity vectors are calculated before continuing with the next iteration of the program.

$$\begin{aligned} w &= \sqrt{W_x^2 + W_y^2} \\ p &= \sqrt{P_x^2 + P_y^2} \end{aligned} \tag{2.16}$$

2.3.4 Parity

As mentioned before (see section 2.1), we have two ways of incorporating the protrusion vector into the cell's movement, leading to two different ways of cell migration.

The first, termed parity 1, results in a model in which the cell always moves forward with the same end, thus defining a front and rear end for the cell that cannot be interchanged. The second, termed parity 2, allows for the cell to reverse its movement direction by reversing its front and rear ends without turning, creating a cell without predefined front and rear. Both cases bear biological relevance, the usage of either depends on the type of cell to be simulated. Observations of migrating cell clearly indicates that the parity 2 model is the one suitable for the simulation of interneuronal precursor cells of the type discussed in this work, as it can be observed that these cells change movement direction by re-orienting the protrusion (and, most likely, internal reorganisation of the cell's actin skeleton), instead of turning the whole cell body. Nevertheless, we present both possibilities for generality reasons.

Figures 2.8a and 2.8b show the influence of protrusivity on polarity depending on the angle between the two vectors for parity 1 and 2. Basically, w_{cos} is a factor for influence of protrusion on movement speed, while w_{sin} governs rotation of the cell body (the polarity vector) towards the protrusivity vector. Formulas for both values are displayed in eqs.2.17 and 2.18.

Looking at the Parity 2 case first, w_{sin} (see eq.2.2 and fig.2.8b, bottom graph) is defined so that it encourages rotation of polarity into a parallel state to protrusivity as polarity diverts from protrusivity (vector difference reaches intermediate angles between parallel and perpendicular). w_{sin} becomes zero if P and W are oriented perpendicular to each other. This reduces the influence on rotation into the parallel or anti-parallel conformation. w_{sin} approaches 0 when the two vectors become parallel, as no rotation is necessary. w_{cos} (see eq.2.1 and fig.2.8b, top graph) takes on positive (in parallel configuration) and negative values (anti-parallel configuration), thus encouraging reversal of direction of the polarity vector and ultimately a reversal of movement direction.

$$w_{cos} = \frac{1}{2} * (1 + \frac{\mathbf{W} \cdot \mathbf{P}}{p}) \tag{2.17}$$

$$w_{sin} = \frac{\mathbf{W} \cdot \mathbf{P}^{\perp}}{p} * max(0, \frac{\mathbf{W} \cdot \mathbf{P}}{p})^{k_s} \tag{2.18}$$

The differences in the parity 1 model are that possible magnitudes of factors w_{cos} and w_{sin} do not allow for movement direction reversal (fig.2.8a). In effect, forcing the cell to rotate 180° to reverse movement direction, leading to the cell always moving forward with same end. This is achieved by having only positive values for w_{cos}, approaching 0 in anti-parallel configuration and thus removing any influence from

protrusivity on movement speed in that configuation. Also setting w_{sin} to 0 if the angle between the two vectors is greater than 90° neglects any influence on rotation when the protrusivity vector is in the back half of the cell ($90° < \theta < 270°$).

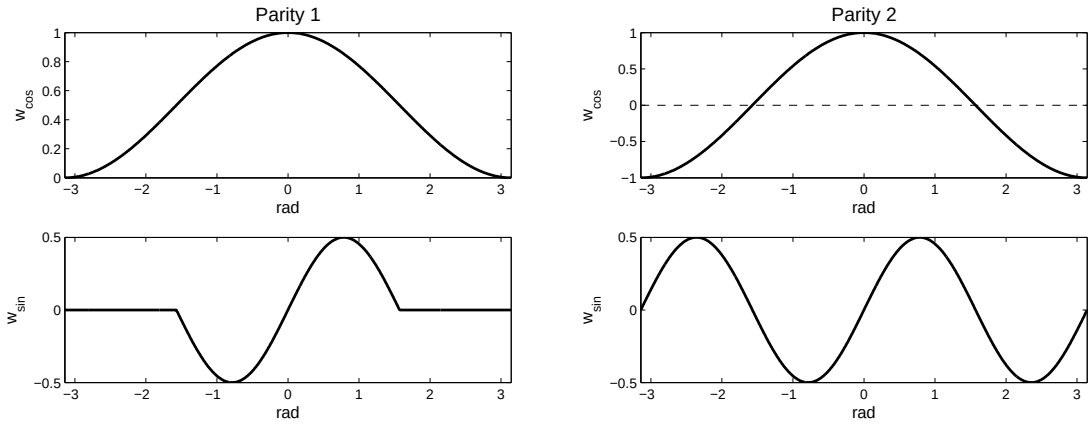

(a) Parity 1

(b) Parity 2

Figure 2.8: Normalized factors w_cos and w_sin for parity 1 and 2, depending on angle between **P** and **W**. Calculation range of angles is $-\pi$ to π. w_cos and particularly w_sin govern the turning behaviour of the cell. In **(a)** w_sin is zero when the angle between protrusivity and polarity is larger than 180°. In effect, protrusive activity at the "rear" of the cell is ignored. This leads to a cell always moving forward with the same tip and a necessity for turning prior to movement direction changes. In **(b)** protrusive activity is considered independent of directional differences between the vectors. This leads to a model cell that can reverse its movement direction without rotation and is able to move forward with both tips during a given simulation run. Instead of turning the polarity vector grows smaller and eventually reverses its prefix, thereby reversing migration direction.

parameter	value	description
t_{end}	100	maximum iteration time
dt	0.05	iteration time step size
c_v	8	attraction strength
c_h	0.23	guidance strength
T_m	2	adjustment time protrusivity towards polarity vector
T_p	3	adjustment time polarity towards protrusivity vector
c_w	10	influence polarity on protrusivity reset
c_b	5	influence polarity on fluctuation of protrusivity strength
c_r	3	influence of polarity on fluctuation of protrusivity orientation
v_c	0.6	reduction factor for orientation influence of $\mathbf{P}$
s0	5	initial cell speed

Table 2.1: Parameter description and values used in all simulations of this chapter.

Alignment	Autocosine P	Autocosine W
none	0.8017	0.0531
attraction	0.7876	0.0595
guidance	0.8178	0.0743
both	0.7850	0.1248

Table 2.2: Table of persistence and auto-cosine values, sorted by active alignments. Values averaged over 100 simulations with 2000 time steps each. Notably, the autocosine for the protrusivity vector increases with guidance enabled. This increase is enhanced if attraction is also active. In contrast, attraction alone does not have any influence on the autocosine of W. However, attraction does seem to have a slight deteriorating influence on the autocosine of polarity. This is easily explained by the added influence on polarity, which is perpendicular to the guidance influence. Influenced in two perpendicular directions, the autocosine is bound to diminish.

2.4 Results

2.4.1 Alignment influence

To determine the influence of the alignment functions (attraction and guidance) on cell migration, we explored simulations without alignment, attraction only, guidance only and, last, with both functions activated. Generally, all of the following tracks are generated with Parity 2, the leading structure is equivalent to the x-axis of the figures (black line), the starting position of the cell is $(x, y) = (0, 5)$ and starting orientation is facing to the right ($\alpha = 0°$).

Without alignment

Without any outside influence from structures on migration, cells move in a rather random fashion (see fig.2.9), but some inherent persistence stemming from protrusivity and polarity vectors can be recognized. Furthermore, we can see the influence of the parity setting leading to cells stopping and switching migration direction (leading to "path reversal"). This mode of migration leads to a bimodal distribution of speeds (fig.2.9 d,e,f), which conforms to our analyses of real cells (see chapter 3; also from unpublished diploma thesis [19]). Fig.2.9 shows calculations of auto- and crosscosine values of polarity and protrusivity vector for Track 3. Noticeably, autocosine values for polarity vector $\mathbf{P}$ show high correlation over a long correlation time, while autocosine of protrusivity decays much faster. This is reasonable as protrusivity fluctuates much more than polarity. As the third track (fig.2.9c) is fairly straight (with path reversals, but without turning), crosscosine values do not show any distinctive feature but remain at a similar level for both positive and negative correlation times. Interestingly crosscosine values are negative, indicating opposed vector directions. This is explained by the parity setting, allowing the cell to move in the direction opposite ($+\pi$) of the polarity vector. Model cells not influenced by alignment usually do not displace from their starting position very much (see fig.2.9c for an exception), indicating that this simple model is insufficient for our purposes and that additions are necessary.

Attraction

Once attraction is included into the model, cells move consistently towards the guiding structure, as expected. Yet attraction alone leads to a somewhat deteriorated form of migration, in terms of directed movement. Cell speed is reduced and displacement from the starting position is lower even than without any alignment influence (compare fig.2.9 (d)-(f) and fig.2.10 (d)-(f)). This is also indicated by the average autocosine of the polarity vector (see tab.2.2), which is reduced now, indicating more directional changes. All of this can be attributed to the influence of attraction. Due to the way attraction is implemented in our model (see fig.2.7a) the cell regains freedom of movement when it is very close to the structure. This leads to cells moving around the structure when very close to it, thus reducing the autocosine of polarity. In the autocosine plot for Track 2 (h) we find a shoulder at $\tau \approx 3$, reflecting this (oscillating) migration around the structure. This effect can indeed impede any directed migration if attraction is set too strong. Figure 2.11 shows such a case. It becomes

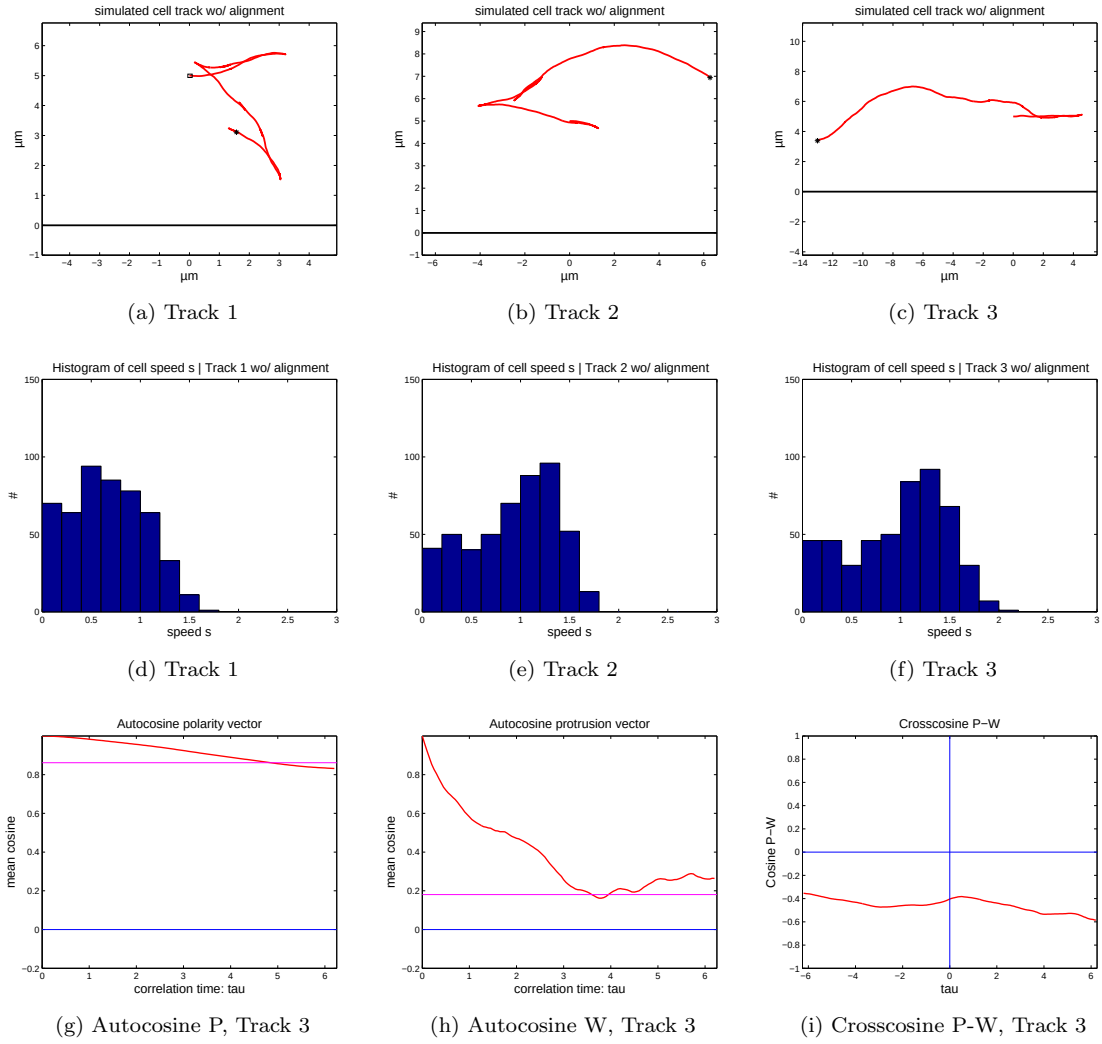

(a) Track 1 (b) Track 2 (c) Track 3

(d) Track 1 (e) Track 2 (f) Track 3

(g) Autocosine P, Track 3 (h) Autocosine W, Track 3 (i) Crosscosine P-W, Track 3

Figure 2.9: Simulated cell paths, **(a)-(c)**, and speed distributions, **(d)-(f)**, without attraction and guidance effects. **(g)-(i)** Exemplary orientation analysis of track 3. Autocosine P, Autocosine W and Crosscosine P-W.

instantly obvious that attraction needs to be balanced with other influences on the cell to achieve directed migration of any form.

Graph (i) shows that the crosscosine of polarity and protrusivity is higher for negative τ and approaching zero for positive τ. This indicates that protrusivity precedes polarity orientation.

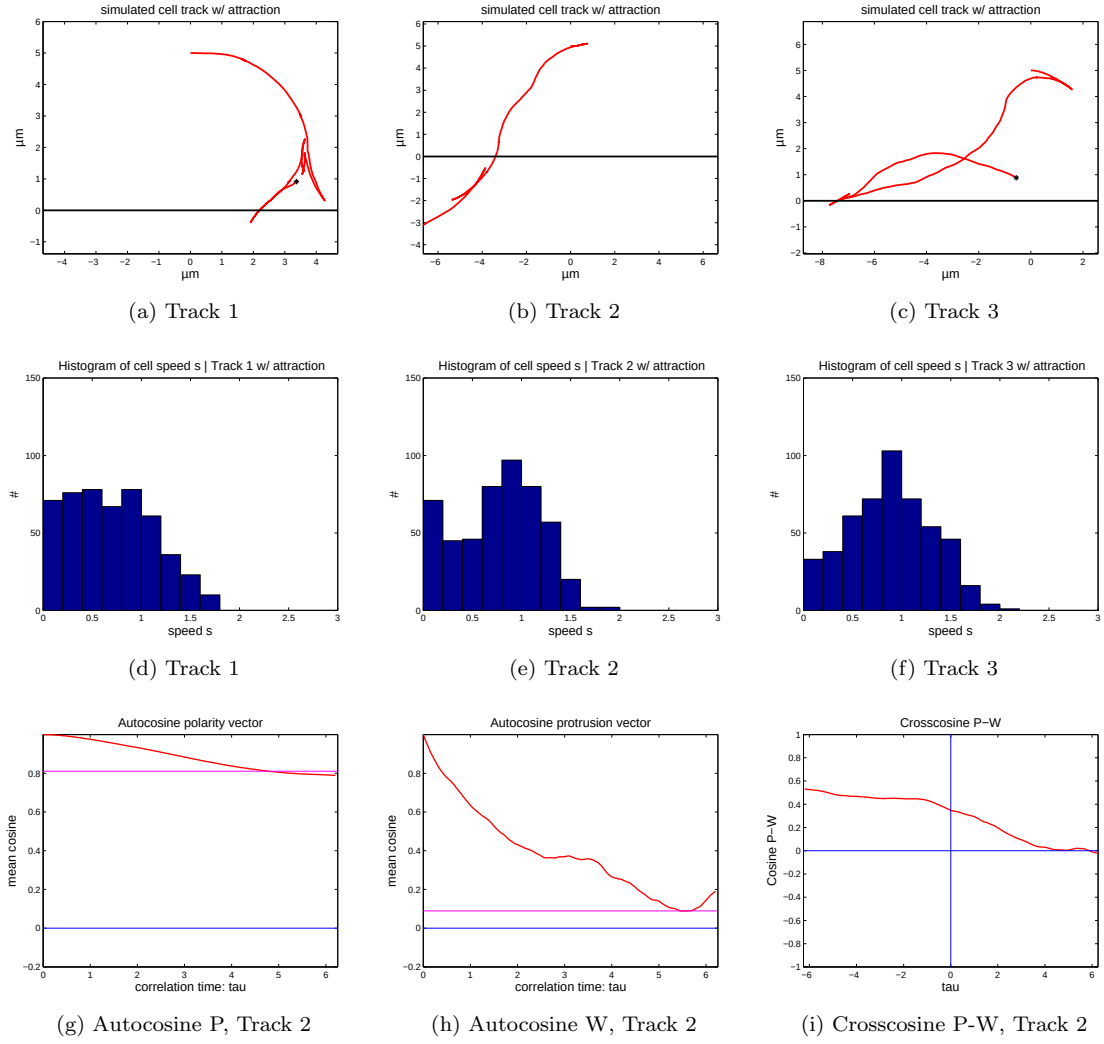

(a) Track 1 (b) Track 2 (c) Track 3

(d) Track 1 (e) Track 2 (f) Track 3

(g) Autocosine P, Track 2 (h) Autocosine W, Track 2 (i) Crosscosine P-W, Track 2

Figure 2.10: Simulated cell paths, **(a)-(c)**, and speed distributions, **(d)-(f)**, with structure attraction. **(g)-(i)** Exemplary orientation analysis of track 2. Autocosine **P**, Autocosine **W** and Crosscosine **P**-**W**.

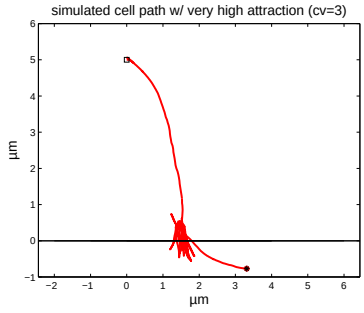

Figure 2.11: Simulation of a cell path with very high structure attraction ($c_v = 3$). The cell oscillates around the structure and does not migrate persistently into any direction.

Guidance

Taking a look at paths generated with a model that implements guidance only it is immediately obvious that cell speed and, thus, distance from starting position are increased in contrast to previous simulations (see figs.2.12 and 2.9). However, without attraction towards the leading structure the cells will eventually move away and loose the guidance effect (see fig.2.13). Furthermore, the bimodal distribution of speed is lost. This is most likely because the guidance effect lowers occurrence of path reversals by reinforcing cell polarity. The averaged autocosine of the protrusivity vector is increased (tab.2.2), as can be expected for the same reason. We again (see fig.2.10h) find peaks in the autocosine plot of protrusivity, showing a period of $P \approx 2.7$. Interestingly, with only guidance influence activated in the simulation crosscosine analysis (i) does not show a maximum for negative correlation times, reflecting a lower influence of protrusivity on polarity. This probably stems from guidance influence overshadowing protrusivity influence. Consistently straight paths show an even direction correlation without peaks, as is the case here.

Attraction and guidance

Once both forms of alignment are implemented simultaneously, cell paths become quite stable. Cells keep approaching the guiding structure and then start moving alongside it, traveling very far from their starting position compared to the previous simulations. Interestingly, even though guidance strength is the same as before, the bimodal distribution of speed is found again, indicating that cells either move fast along the guiding structure or slowly while reorienting themselves (which can result in path reversal). Tab.2.2 shows that the averaged autocosine of protrusivity is much increased over previous results, which can be attributed to the alignment influences. Protrusivity is influenced by cell polarity, which is much more stable if the cell shows fast directed migration. We again notice the shoulders in the autocosine plot of protrusivity (h), this time indicating a period of $P \approx 1.9$. Furthermore, crosscosine analysis (i) shows a high correlation for negative τ and a decreasing correlation for positive τ, again displaying the influence of protrusivity on polarity.

Thus, especially attraction strength must be balanced with other influences (see fig.2.11 again) and keeping this in mind, we now explore relative attraction and guidance settings on resulting cell velocity.

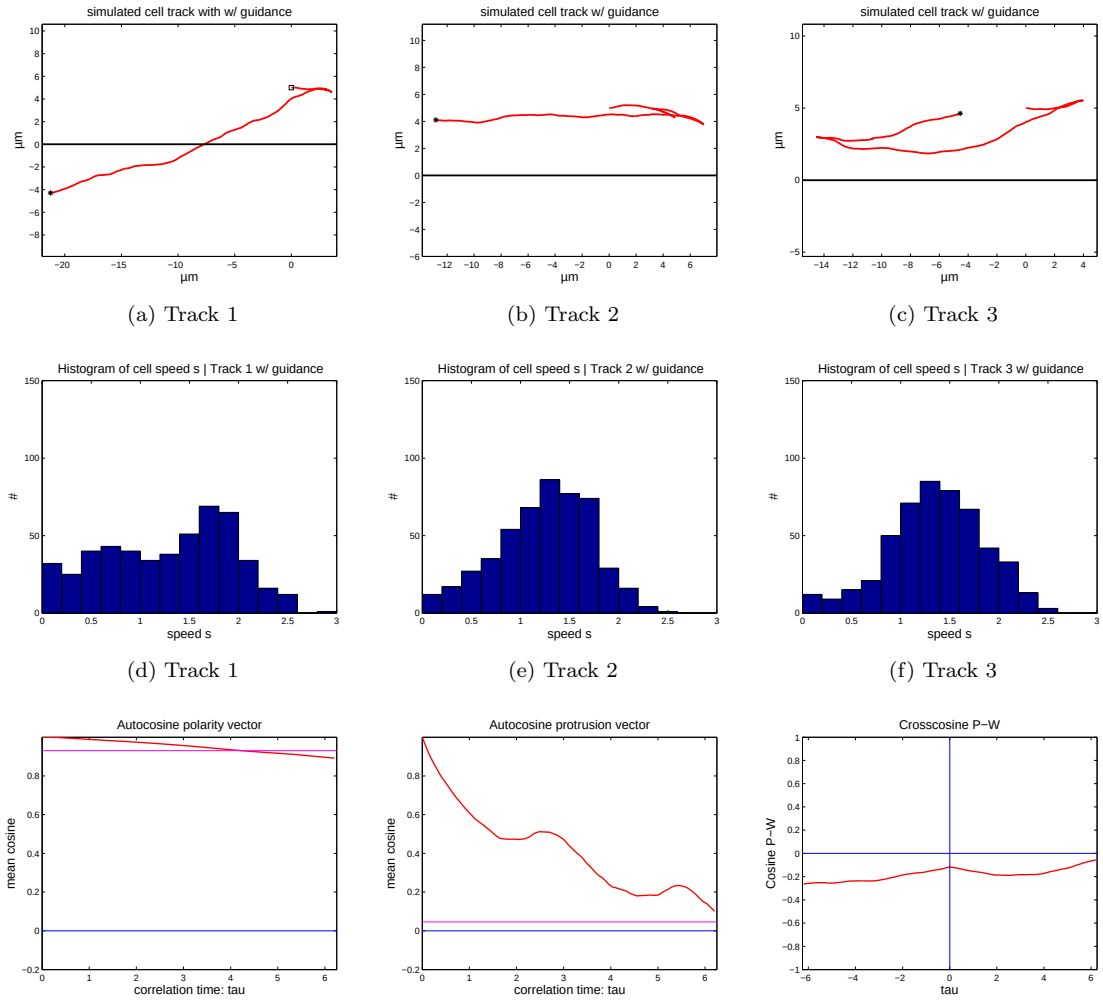

(a) Track 1 (b) Track 2 (c) Track 3

(d) Track 1 (e) Track 2 (f) Track 3

(g) Autocosine P, Track 3 (h) Autocosine W, Track 3 (i) Crosscosine P-W, Track 3

Figure 2.12: Simulated cell paths, **(a)-(c)**, and speed distributions, **(d)-(f)**, with guidance. **(g)-(i)** Exemplary orientation analysis of track 3. Autocosine **P**, Autocosine **W** and Crosscosine **P-W**.

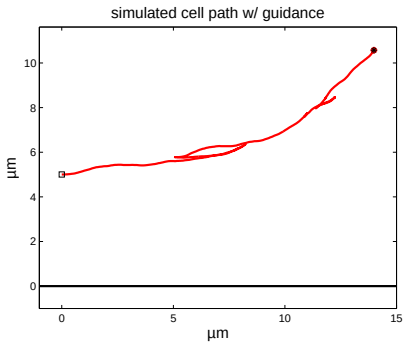

Figure 2.13: Simulation of a cell path with enabled guidance leaving the area of influence projected by the structure.

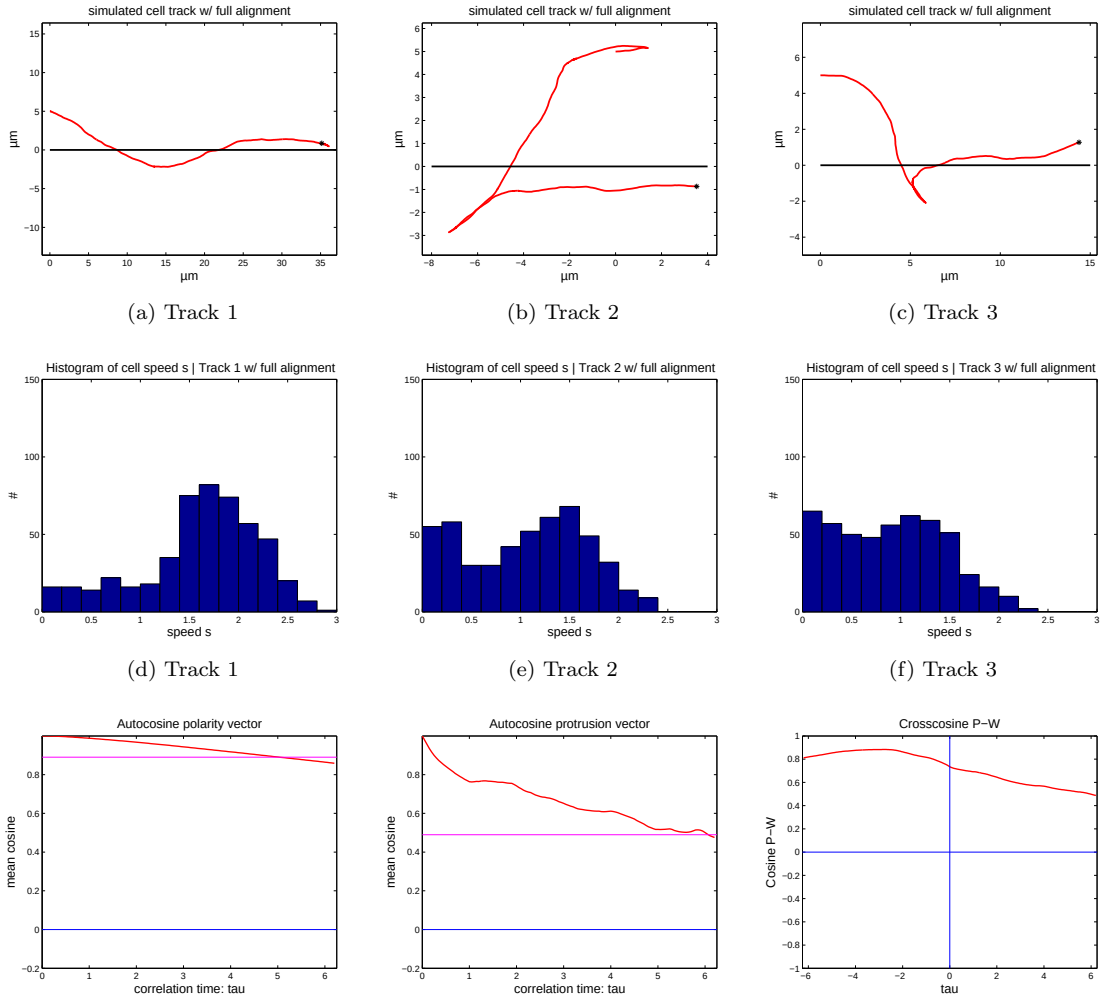

(a) Track 1 (b) Track 2 (c) Track 3

(d) Track 1 (e) Track 2 (f) Track 3

(g) Autocosine P, Track 1 (h) Autocosine W, Track 1 (i) Crosscosine P-w, Track 1

Figure 2.14: Simulated cell paths, **(a)-(c)**, and speed distributions, **(d)-(f)**, with structure attraction and guidance. **(g)-(i)** Exemplary orientation analysis of track 1. Autocosine P, Autocosine W and Crosscosine P-W.

2.4.2 Exploration of alignment parameter space

We explored the influence of relative settings of attraction and guidance strengths on resulting model cell velocity along the leading structure (V_x). To this end we performed several simulations with varying *cv* (attraction strength) and *ch* (guidance strength) values. Results can be seen in figure 2.15. Average V_x is reduced linearly for higher attraction strengths. This is expected as attraction generates forces perpendicular to the structure and, therefore, to the intended migration direction. Figure

2.11 shows the effect of a very high attraction strength, as we have mentioned earlier. On the other hand, V_x increases logarithmically with a noticeable saturation for higher guidance strengths. Because guidance affects protrusivity directly, which in turn influences polarity and, thus, cell velocity, it is expected that increased guidance strength increases cell speed. The saturation effect stems from the adjustment of protrusivity towards a given base protrusivity (see eq.(2.6)).

Changing both parameters in an ordered fashion and running 100 simulations with 200 timesteps each for every parameter set yielded results shown in figures 2.16 **(a)** and **(b)**. The surface plot has been smoothed twice with a moving average of width 2 and weights of [0.25,0.5,1], while the contour plot has been smoothed once using the same method. We notice the peak of V_x, declining for both lower guidance strength and higher attraction strength, confirming results of figure 2.15.

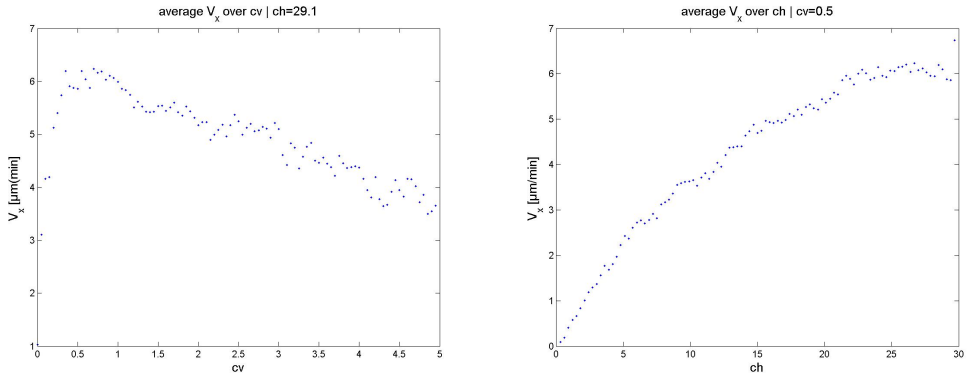

(a) c_v (b) c_h

Figure 2.15: Exploration of parameter influence. Depicted is the resulting average speed along the structure (V_x) over 100 runs. Exploring c_v **(a)** and c_v **(b)** respectively, other parameters as in tab.2.1.

2.5 Discussion

We have shown that our model of an interneuronal precursor cell we have developed is working as intended. Our modeling of these cells is based on the novel approach of explicit simulation of protrusive activity as a stochastic vector that influences cell polarity and is in turn influenced by polarity and, especially, outside factors, namely structure attraction and guidance. After identifying important factors and establishing valid parameter values, our model generates paths that resemble tracking results

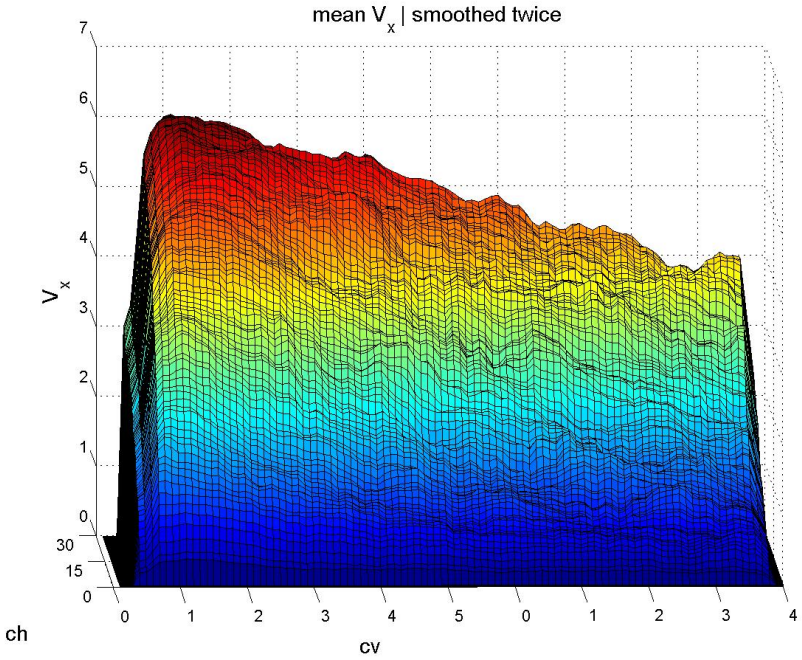

(a) surface plot

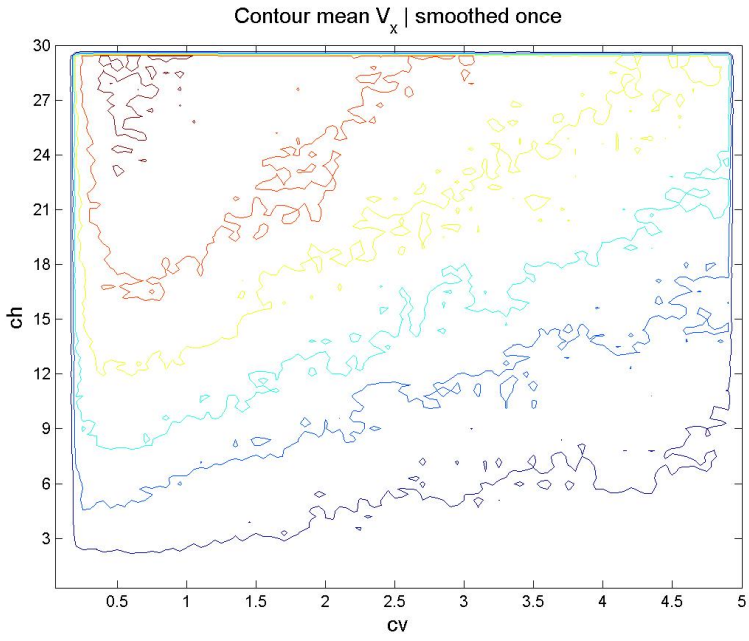

(b) contour plot

Figure 2.16: Surface (**a**) and contour (**b**) plots of average speed along the guiding structure (V_x) for varying attraction (cv) and guidance (ch) strengths. Mean V_x averaged over 100 simulation with 200 timesteps each. Surface plot smoothed twice and contour plot smoothed once with a moving average with distance 2 and weights of [0.25, 0.5, 1].

from real cells very much. These important factors specifically include influence of extracellular structures, without which we do not achieve persistent directional migration. The analysis of attraction and guidance strength parameter settings (see figs.2.16 and 2.11) yields interesting indications to the possible nature of structures or cues. As guidance needs to be relayed, either by contact or released cues, we can postulate that in the case of contact guidance amount and density of available structures needs to be related to contact strength between cell and structure. It is obvious that a cell that attaches very tightly to a given structure will need more influence (force) to migrate away from it, than a cell that attaches only lightly.

One of the important components that turned out to be responsible for appearance of the bimodal distribution is the influence of cell polarity on protrusivity fluctuation. It is a well known fact that cells transport and recycle actin and other substances necessary for migration, creating what is called a retrograde flow [24]. Increased speed of migration means increased need of migratory active substances and, thus, an increase in retrograde flow. Furthermore, increased cell speed usually corresponds to increased cell polarity, based on time-lapse observations this seems especially true for the type of cell we examine here. It seems reasonable to suppose that a streamlined, polar cell is less prone to influence of (internal) fluctuations.

Concluding, our model of structure-influenced protrusive activity governing cell polarity and, ultimately, migration is able to simulate cells moving persistently along a given guiding structure and is additionally capable of mirroring the specific bimodal distribution of speeds found in tracks of real cells.

Chapter 3

Application and comparison

3.1 Introduction

In the following we will describe results obtained by using the tracking program introduced in chapter 1 and analyze resulting cell tracks within the cerebellum's grey and white matter. We will then compare the gained information to simulation results of the same type of cells taken from 2.

Cell paths are extracted from the time lapse movies introduced in chapter 1. After cropping the region of interest containing the target cell, images were cleaned to remove background noise in order to facilitate tracking and improve result accuracy. To this end, pixels clearly not belonging to the cell in question had their value set to zero (black).

The special nature of our tracking program allows us to extract information about cell orientation and elongation behaviour, in addition to the standard positional information of usual tracking programs. After analyzing the received data, we will use any gained insights to set up our simulation model and will finally compare extracted (real) cell tracks to simulated cell paths. The comparison of tracking and simulation results will help us to achieve a better understanding of the character of migration of interneuronal precursor cells and, ideally, will lead to new insights about cell migration in general.

3.2 *In vivo* cell tracks

3.2.1 Grey matter

We will look at three exemplary cell tracks from inside the cerebellum's grey matter at first, as this was our primary research interest when this work began. Their paths and speed histograms, as extracted with our tracking program, are displayed in fig.3.1. The bimodal distribution of cell speeds we observed in earlier works (diploma thesis [19]; compare fig.3.2) is marginally noticeable. Clearly, this is due to the relatively low number of data points of each single track, each having a path length of about $100\mu m$ only. However, from the movies it can easily be seen that cells are characterized by low migration speeds with a few bursts of increased speed. Generally, we see a relatively large number of low speed occurrences, followed by a distinct trough at around $0.2\mu m/min$ and a broad distribution of higher speeds up to 0.8-1$\mu m/min$. Thus, precursor cells in grey matter seem to alternate between phases of reorientation at low speed and persistent migration at high speed.

To identify cell dynamics and also possible periodicities of the alternating behaviour, cell speed and leg lengths were plotted over time (figs.3.3). Curves were smoothed by a weighted moving average with a width of 2 time-lapse steps and weights of [0.25,0.5,1]. A few interesting observations are easily noticed in these graphs. Cell speed (blue) increased before an increase in cell length (overall leg lengths, black) became visible (compare fig.3.3c). This is particularly true for front leg lengths (green), while we found a short delay between corresponding slopes of rear leg lengths (red) and cell speed. This result of an increase in speed prior to an increase in cell lengths is confirmed by crosscorrelation analysis of these two values (see fig.3.4(a), (b), (c)) showing significant correlation peaks at a delay of ≈ 10 minutes. Further crosscorrelation analyses (figs.3.4(d)-(f) & (g)-(i)) established that the observed relation between speed and cell length is due to a delayed increase in rear leg length, (g)-(i), and not primarily because of an increased front leg length. While graphs (g)-(i) are consistently showing significant positive correlations between an increase in cell speed and a delayed increase in rear leg length, graphs (d)-(f) warrant closer inspection of front leg dynamics. To this end, crosscorrelation of front and rear leg lengths, (j)-(k), shows peaks at $\tau = 0$minutes with shoulders towards positive time delays, indicating that the front leg is indeed preceding the rear leg. This relation extends to orientation as well with Crosscosine analysis showing small peaks for low positive τ (see figs.3.6(g)-(i)).

The fairly blurred nature of the relation between cell speed and front leg length was

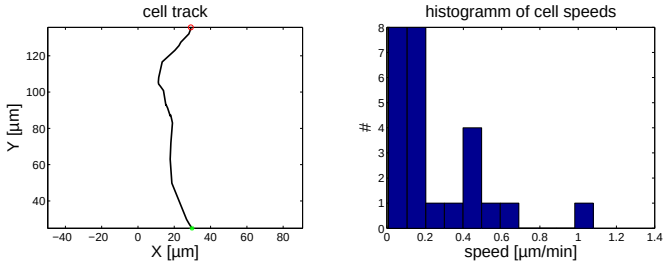

(a) Track

(b) Histogram s

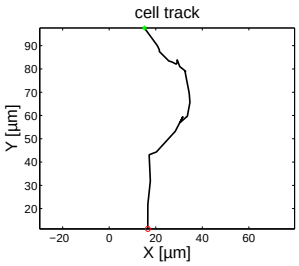

(c) Track

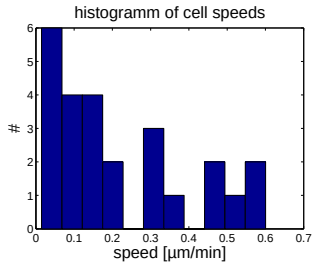

(d) Histogram s

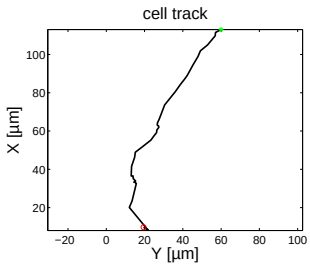

(e) Track

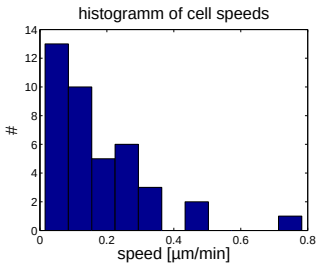

(f) Histogram s

Figure 3.1: Tracks and histogram of cell speeds of interneuronal precursor cells migrating in grey matter. As determined by image force supported automated tracking (see chapter1), extracted from time-lapse movies S008 (Track 1&2) and S007 (Track 3). **(a,c,e)** Green asterisk: starting position. Red circle: final position. **(e)** Image rotated 90° to match structure orientation to other tracks.

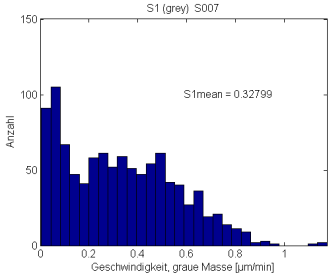

(a) Histogram s, S007

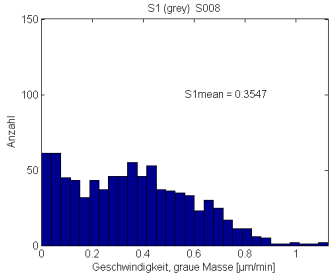

(b) Histogram s, S008

Figure 3.2: Histograms of cell speeds in grey matter. Data pooled over 50 cell tracks, extracted manually with *MTrackJ*. Data taken from diploma thesis [19].

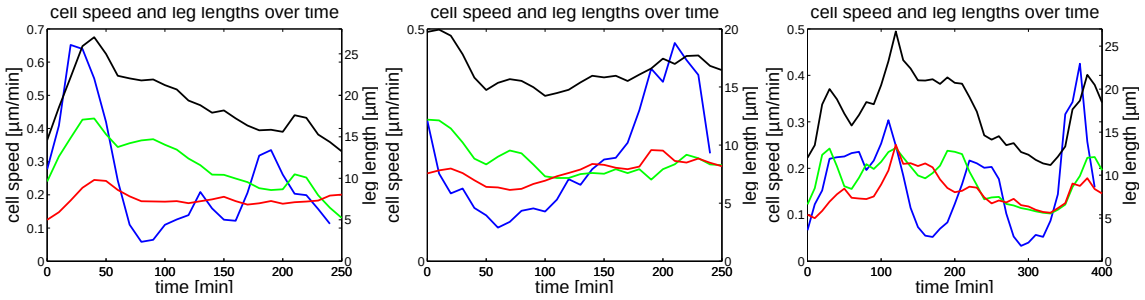

(a) Track 1 (b) Track 2 (c) Track 3

Figure 3.3: Cell speed and leg lengths of front and rear legs, as well as combined length. Curves smoothed with a weighted moving average of width 2 (time-lapse steps) and weights of [0.25, 0.5, 1]. **Blue line:** Cell speed [$\mu m/min$]. **Green line:** Front leg length [μm]. **Red line:** Rear leg length [μm]. **Black line:** Sum of front and rear leg lengths [μm]. Leg lengths values correspond to left and speeds to right y-axis.

unexpected, but might be explained by interference effects of cell dynamics. Figure 3.5 shows autocorrelation analyses of speed, front and rear leg lengths. Due to the relatively low amount of data results are not significant in all cases, but can still be used as an indication of cell dynamics. Autocorrelations of cell speed show correlation shoulders or peaks at 30 minutes, (a)&(b), indicating a periodic behaviour with a period duration of 30 minutes. Furthermore, autocorrelation of front leg length, (d)-(f), indicates a possible periodicity at 50-60 minutes. It is clear that an independent change in front leg length overlaid on a cell speed dependent length change can result in unclear crosscorrelation results. Thus, the exact relation between cell speed and front leg length is unclear.

Autocorrelation of rear leg lengths indicates a periodicity of 30 minutes (2*30=60 minutes in fig.3.5g), just like cell speed. However, these results are possibly a result of interference of cell speed periodicity. Proposing that the rear leg trails the cell (passively) and, thus, follows any speed changes with changes in length after a short delay, it is expected to find cell speed periodicity reflected in rear leg dynamics. The small positive time delay of crosscorrelation of speed and rear leg length, as well as the autocorrelation results fit the picture of a rear leg passively trailing the cell body.

Next, we employed crosscosine calculation (see sec.2.2) to gain insights into orientation relations between migration and leg directions. Figures 3.6 (a), (b), (c) show the calculated crosscosine for velocity vector $\mathbf{V}$ and front leg $\mathbf{P}$ for all three tracks. The curves run quite smoothly keeping values of around 0.6. This signifies that the

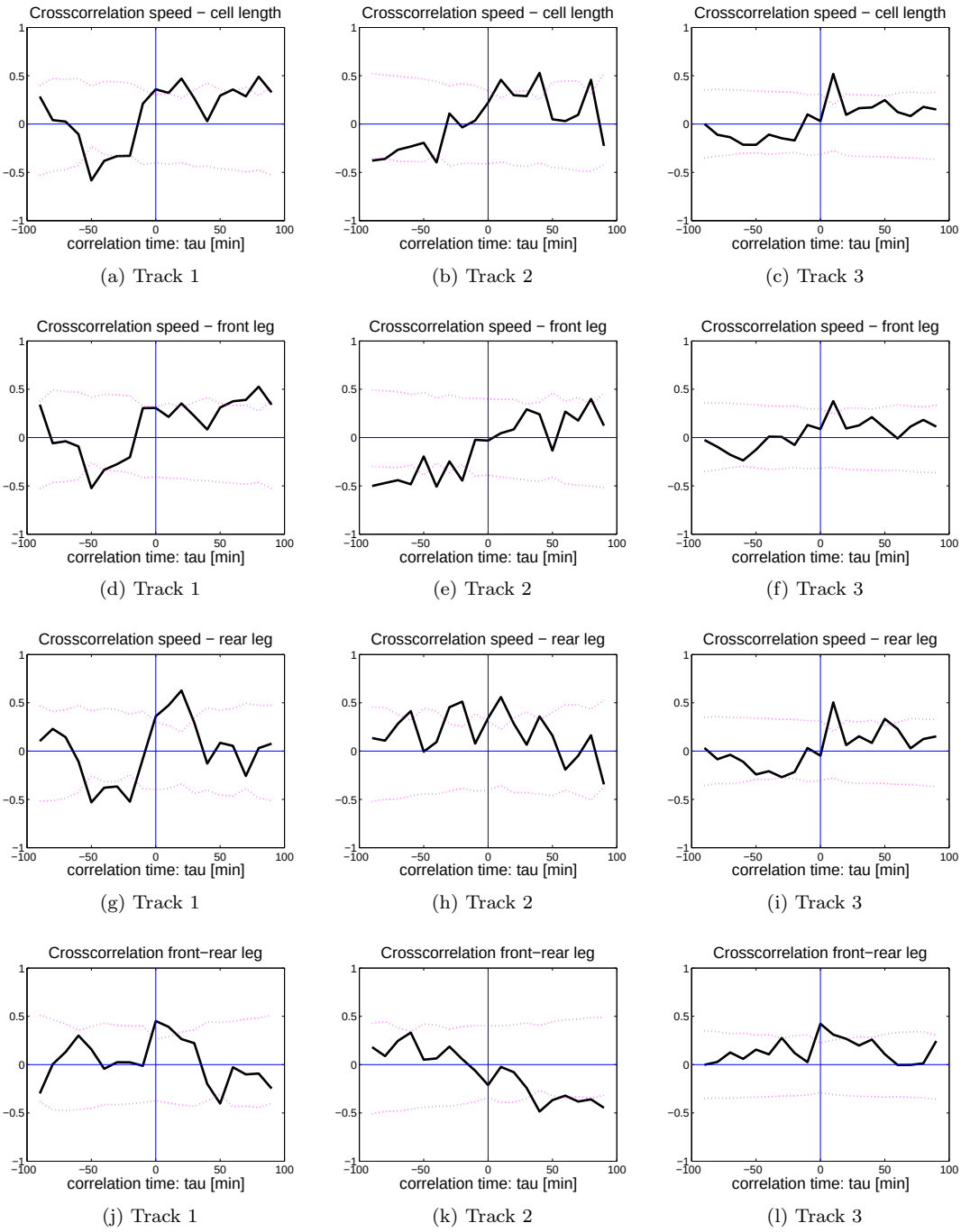

(a) Track 1 (b) Track 2 (c) Track 3

(d) Track 1 (e) Track 2 (f) Track 3

(g) Track 1 (h) Track 2 (i) Track 3

(j) Track 1 (k) Track 2 (l) Track 3

Figure 3.4: Crosscorrelation of overall cell speed and leg lengths for three selected cell tracks within the grey matter. **(a)-(c)** Overall length. **(d)-(f)** Front leg length. **(g)-(i)** Rear leg length. **(j)-(l)** Crosscorrelation front with rear leg. Maximum correlation time $\tau_{max} = 100min$ represents a third of the complete time series length. 10 minutes between images. Dotted magenta line indicates significance threshold.

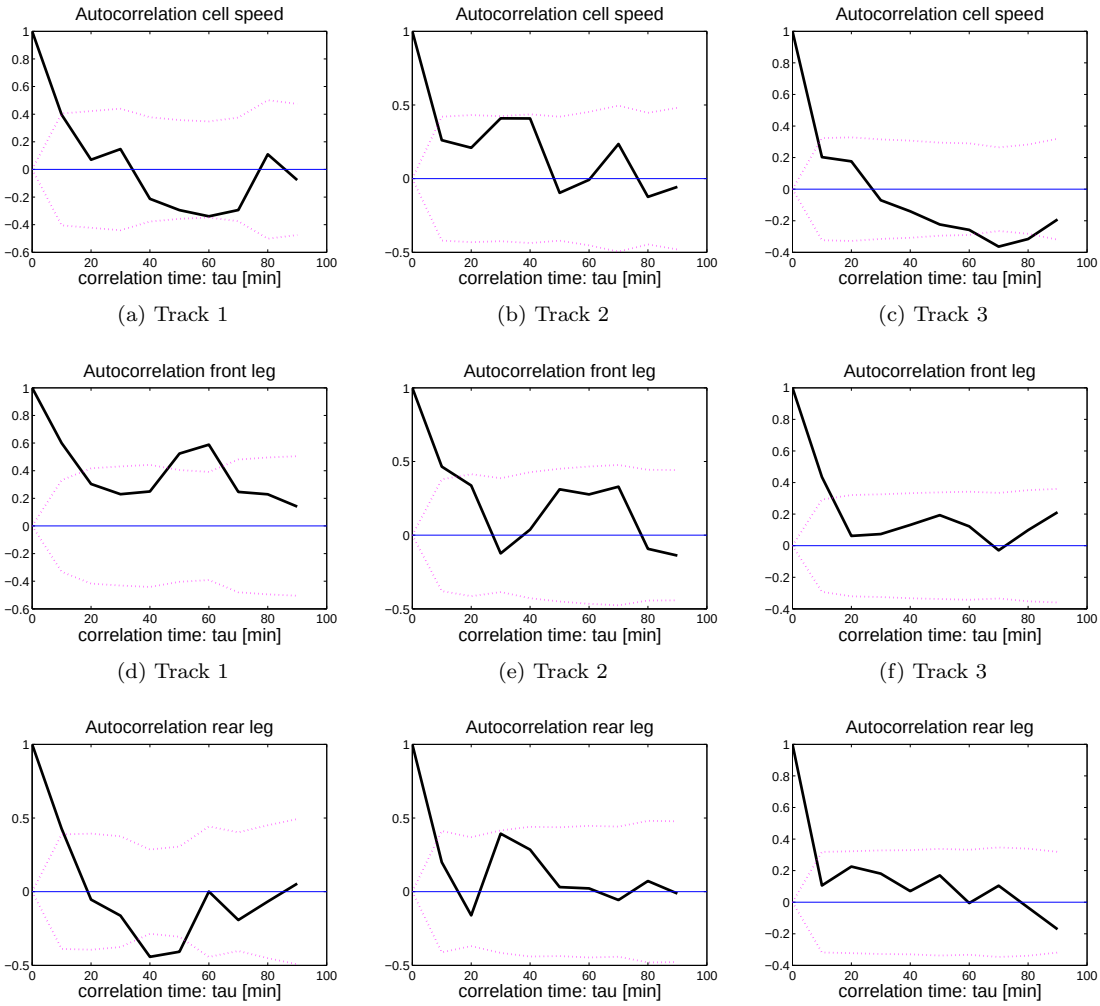

(a) Track 1 (b) Track 2 (c) Track 3

(d) Track 1 (e) Track 2 (f) Track 3

(g) Track 1 (h) Track 2 (i) Track 3

Figure 3.5: Autocorrelation of cell speed and leg lengths for three selected cell tracks within the grey matter. **(a, b, c)** Autocorrelation of speed s. **(d, e, f)** Autocorrelation of front leg length. **(g, h, i)** Autocorrelation of rear leg length. Maximum correlation time $\tau_{max} = 100min$ represents a third of the complete time series length. 10 minutes between images. Dotted magenta line represents significance border.

track itself is quite straight, displaying, at most, a consistent small curvature (confirm fig.3.1). Looking more closely at the plots, it can be seen that, while crosscosine values are positive for all correlation times, they show a slightly higher correlation for positive time delays τ. This can be taken as an indication that front leg orientation follows cell velocity direction, rather than preceding it.

Comparison of velocity vector and rear leg orientation by crosscosine (figs.3.6 (d), (e), (f)) shows more pronounced negative peaks at small positive tau values. This means that the angle difference is closer to 180° at small time delays. In effect, rear leg orientation follows migration direction with a time delay of approximately 10 minutes, this is the same value we have determined for delay between cell speed and rear leg length (compare fig.3.4(h)&(i)).

Track section

For more detailed information on turning and vector orientations we take a look at a specific turning event of a typical cell, displayed in figure 3.7. The section taken here stems from a grey substance track and consists of eight data points. As orientation analysis is obviously less useful on straight path sections, we have specifically chosen a section including a reasonably large orientation change, which covers roughly 70°. Front leg vectors are displayed in green, while rear leg vectors are colored red. Blue lines correspond to velocity vectors, i.e. the cell track. A slight divergence between velocity vectors and front leg vectors can be seen by eye. However, crossorientation analysis only shows that this discrepancy is only marginal (fig.3.8a). Confirming previous evaluations of full tracks, figure 3.8a shows a delay of rear leg and velocity vector orientation. Both of these results are in line with our earlier observations in this chapter and confirm that front leg orientation corresponds to migration direction without time delay ($tau = 0$), while rear leg orientation follows migration direction with a slight time delay. Furthermore, both legs show best overall length correlation (largest y-axis amplitude) at $tau = 0$, indicating that even though rear leg angular changes are delayed, its length relates directly to current migration speed.

Additionally, crossorientation analysis suggests that the cell is migrating half its cell length during the time between two images. At $\approx 0.5\mu m$ per minute, 10 minutes between images and cell lengths of $\approx 10\mu m$ this is a reasonable observation.

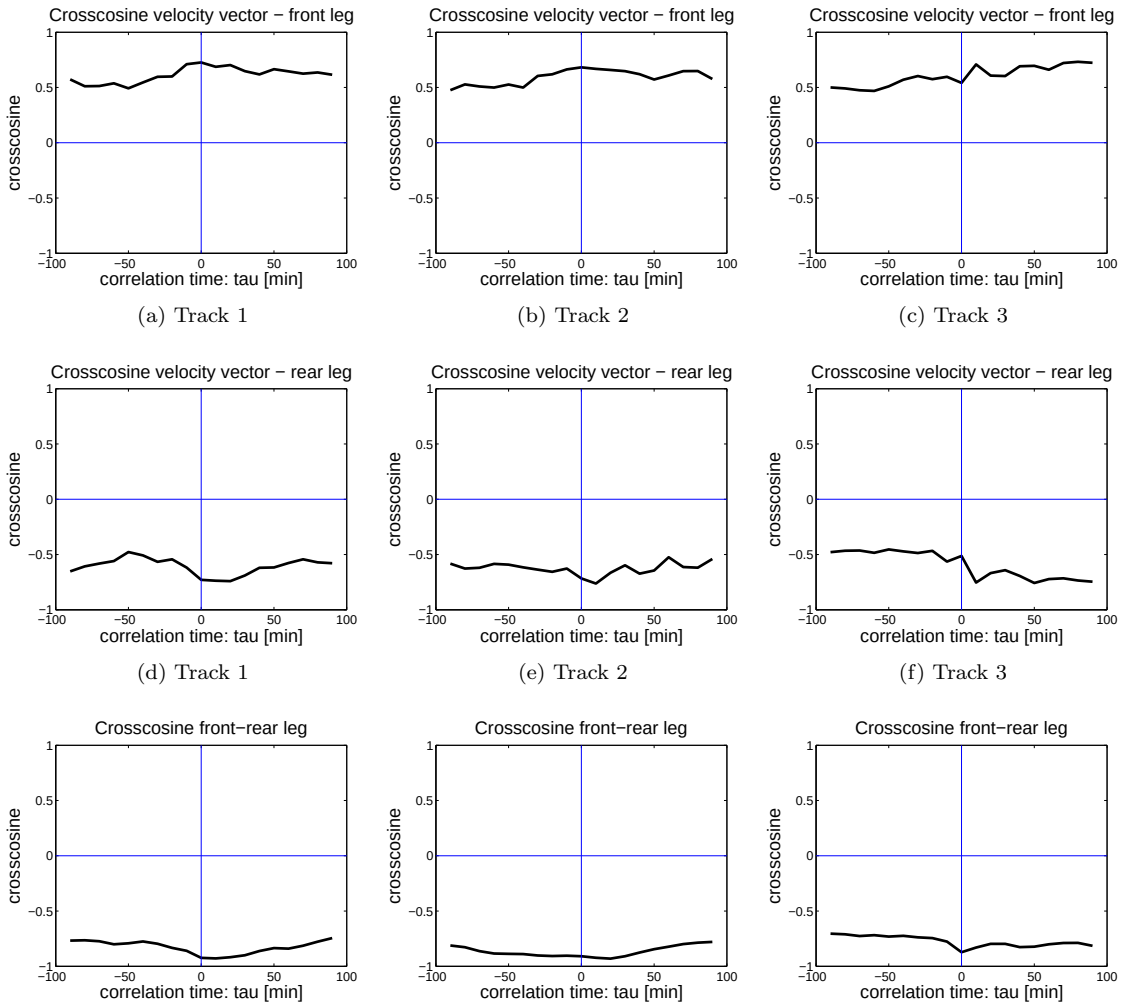

(a) Track 1 (b) Track 2 (c) Track 3

(d) Track 1 (e) Track 2 (f) Track 3

(g) Track 1 (h) Track 2 (i) Track 3

Figure 3.6: Crosscosine of velocity vector with front, **(a)-(c)**, and rear leg, **(d)-(f)**, directions for three selected cell tracks within the grey matter. **(g)-(i)** Crosscosine front leg with rear leg. Maximum correlation time $\tau_{max} = 100min$ represents a third of complete time series length. 10 minutes between images.

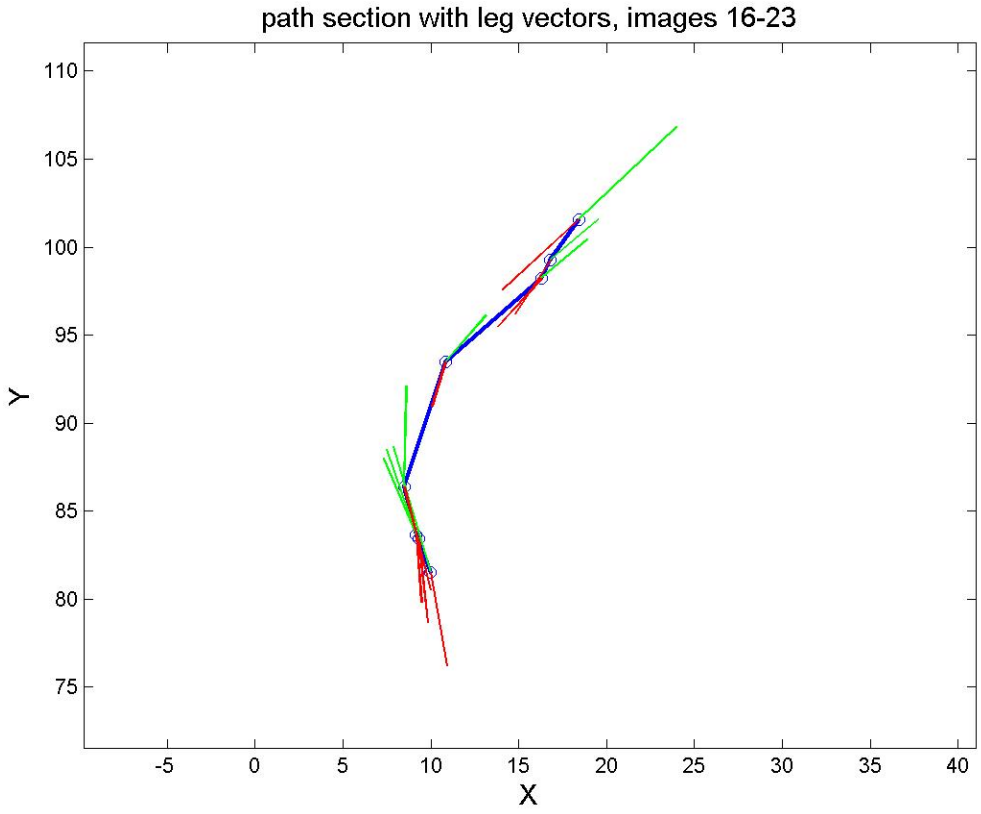

Figure 3.7: Section of a cell track displaying a directional change. Section extracted from track 1, images 16-23. Units of X and Y axis are $[m]$. Displayed vectors are **blue**: Cell track/velocity, **green**: Front leg, **red**: Rear leg.

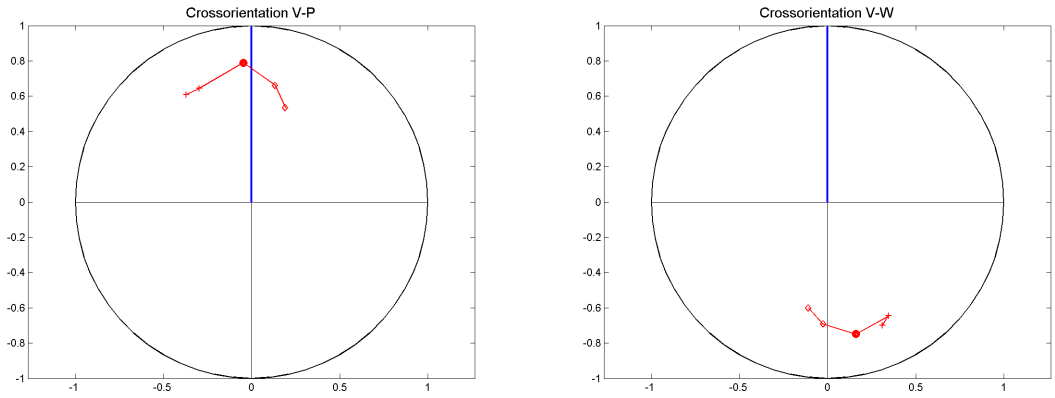

(a) Track 1

(b) Track 2

Figure 3.8: Crossorientation of velocity vector and front and rear leg directions of the selected track section. Maximum correlation time τ_{max} equal to eight images. 10 minutes between images.

Conclusions

We summarize the key points of the previous results as they influence our model of a migrating interneuronal precursor cell, presented in section 3.3.1.

- Consistently observed **path reversals**.
- Cells move with a **bimodal distribution of speeds**. This probably stems from regular rounding and slowing down between modes of fast migration.
- **Periodicity of cell speed** with a period of $\approx$ 30 minutes and possibly front leg with a period of $\approx$ 50 minutes.
- Data suggests a **(passively) trailing rear end** following the cell body with a delay of $\approx$ 10min, both in orientation and length.
- **Front leg length** (protrusion) changes **precede rear leg length** changes (cell body) and, less significant, orientation.

#	tissue	mean speed [$\mu m/min$]	mean speed (dipl) [$\mu m/min$]
1	grey	0.33 ± 0.17	0.34 ± 0.23
2	white	0.52 ± 0.24	0.40 ± 0.24

Table 3.1: Mean speeds of tracked cells in white and grey matter. **First column:** Values averaged over tracks displayed in this work for grey and white matter respectively. **Second column:** Averages taken from a previous work (diploma thesis [19]). Even though values differ between works, speeds in white matter are consistently higher than in grey matter.

3.2.2 White matter

It is known that interneuronal precursor cells of the type observed here migrate from the germinal layer through the white matter towards the molecular layer of the cerebellum [25]. As we have found in a previous work [19] migration behaviour is different inside the cerebellum's white matter as compared to grey matter. This difference can likely be attributed to different morphologies. The white matter consists mainly of axons and fibrous extracellular material [26], while the grey matter is more complex and includes several different types of neurons and other cells, as well as axons and dendrite trees oriented in different planes (compare fig.3 and [4] & [3]). Figures 3.9 (a), (c) and (e) display extracted white matter paths with a proposed structure orientation roughly equal to the x-axis.

In line with previous observations maximum cell speed is similar to that in grey matter, but overall speeds are shifted towards a higher mean with fewer occurences of low speeds and a corresponding loss of the bimodal distribution (see figs.3.9 (b), (d), (f) and compare fig.3.10). This is supported by observations by us that cells show constant movement when inside the white matter, as opposed to a more saltatory form of migration inside the grey matter. Table 3.1 shows calculated mean speeds averaged over tracks of this work (first column) and a previous work averaged over 50 tracks (second column). In both works mean speeds of white matter tracks are consistently higher than those of grey matter tracks.

Looking at time plots in figures 3.11 (a), (b) and (c) it seems that changes of cell speed (blue) precede changes of cell length (black), though less pronounced than previously observed for grey matter tracks. Crosscorrelation results (see figs.3.12(a)-(c)) are less significant than for grey matter tracks (fig.3.4(a)-(c)), but still support this observation. Taking a closer look at this dynamic, figures 3.12(g)-(i) indicate a correlation of rear leg to cell speed at $\tau \approx$10minutes, equal to what we found for grey matter tracks. Additionally, correlation of front leg length and speed, (d)-(f), proposes

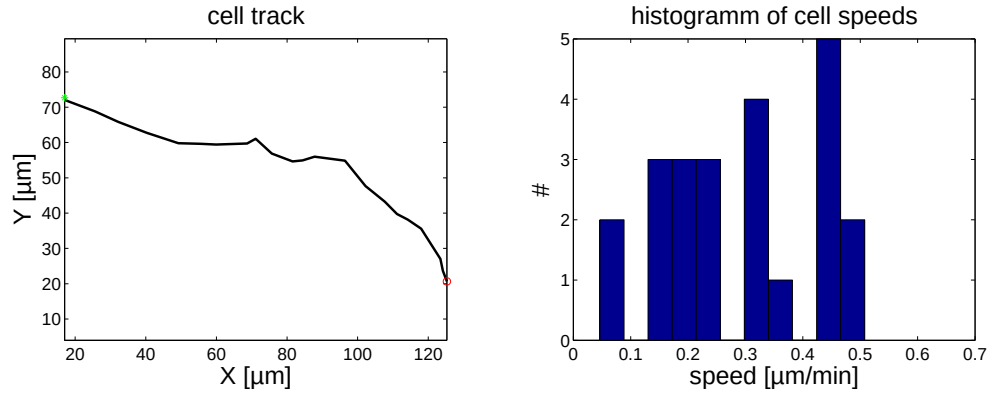

(a) Track (b) Histogram s

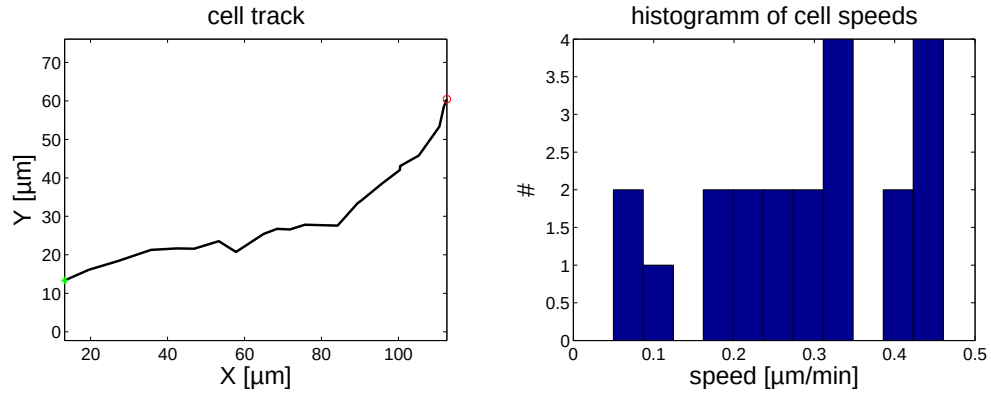

(c) Track (d) Histogram s

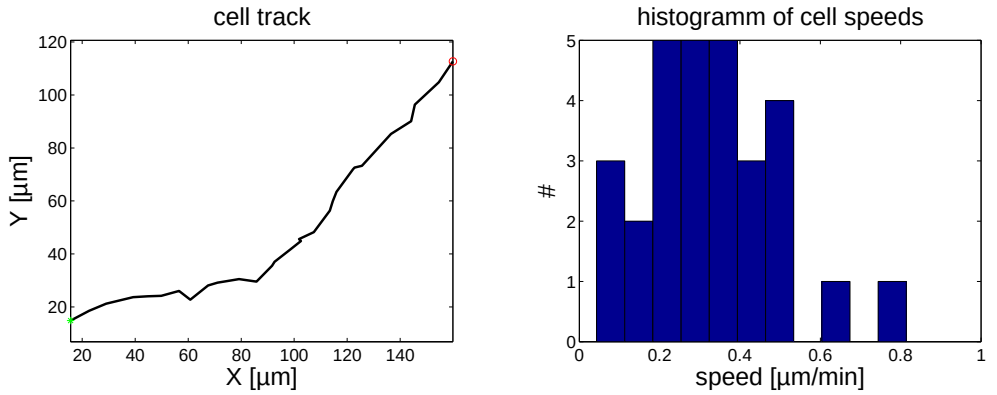

(e) Track (f) Histogram s

Figure 3.9: Tracks and histogram of cell speeds of interneuronal precursor cells migrating in white matter. As determined by image force supported automated tracking (see tracking chapter). Extracted from time-lapse movies S008. **(a,c,e)** Green asterisk: starting position. Red circle: final position.

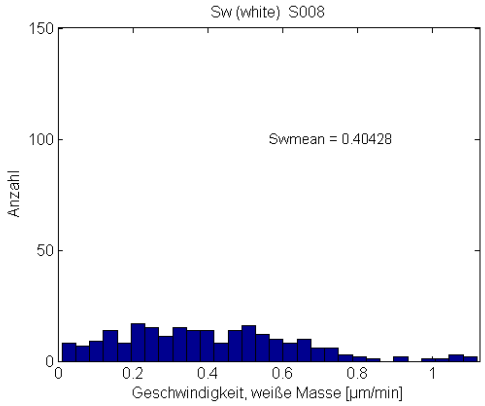

Figure 3.10: Histogram of cell speed s in white matter. Data pooled over 5 tracks, extracted manually with *MTrackJ*. Data taken from diploma thesis [19].

that the front leg enlarges simultaneously with speed increases by showing maxima at $\tau \approx 0$minutes. Crosscorrelation of front and rear leg lengths displays significant correspondence between an increase in leg lengths without time delay (and additional shoulders towards positive τ), indicating a slightly preceding front leg. This is equal to what we found for grey matter tracks. Orientation analysis (figs.3.14(g)-(i)) further supports these similarities by showing highest directional correlation at $\tau \approx 0$ minutes.

Again, we expect that interference effects are overlaid on correlations. Autocorrelation of cell speeds confirms a possible 30 minute periodicity in migration behaviour (fig.3.13(a)-(c)) and autocorrelation results of rear leg length reflect this period, (g)-(i). These results are consistent with our results for grey matter tracks (see 3.2.1). Furthermore, autocorrelation of front leg length (d)-(e) indicates periodicity at 40-50 minutes, also equal to previous results for grey matter tracks. Assuming that cells exhibit an independent protrusion dynamic with a period duration of approximately 50 minutes and a migration periodicity of 30 minutes, as well as a relation between increased cell speed and cell length, it is clear that interference effects can heavily influence results.

Crosscosine analysis of velocity vector and front leg shows a slightly increasing correlation for positive correlation times (see figs.3.14 (a), (b), (c)), while rear leg analysis shows the characteristic negative dent at small positive tau (see figs.3.14 (d), (e), (f)). Both of these observation match the ones done for grey matter tracks (compare figs.3.6) and further support the idea of a front leg orientation following migration direction and a rear leg trailing the main cell body with a short delay.

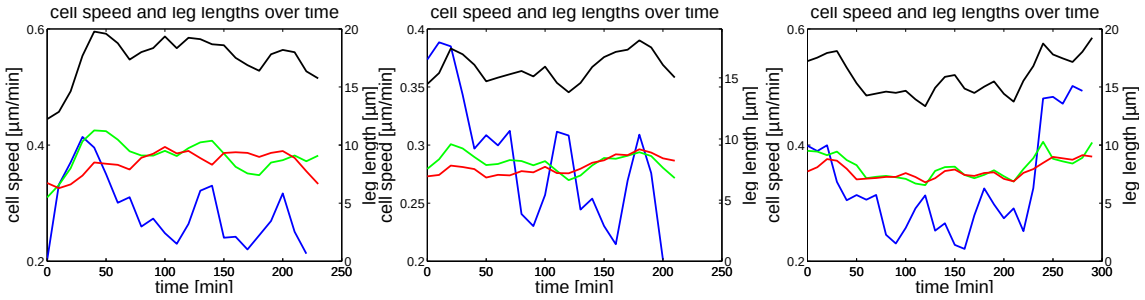

(a) Track 1 (b) Track 2 (c) Track 3

Figure 3.11: Cell speed and leg lengths of front and rear legs, as well as combined length. Curves smoothed with a weighted moving average of width 2 (time-lapse steps) and weights of [0.25, 0.5, 1]. **Blue line:** Cell speed $[\mu m/min]$. **Green line:** Front leg length $[\mu m]$. **Red line:** Rear leg length $[\mu m]$. **Black line:** Sum of front and rear leg lengths $[\mu m]$. Leg lengths values correspond to left y-axis and speeds to right y-axis.

Conclusion

- **Absence of path reversals** in white matter tracks.
- **Unimodal distribution of speeds**.
- **Periodicity** of cell speed with a period of 30 minutes and of front leg length with a period of 50 minutes. Mirroring to results of grey matter tracks.
- Indications of a **(passively) trailing cell rear**, following the cell body, both in size and orientation with a delay of ≈10 minutes.
- Correlation of front and rear leg lengths and orientation at $\tau \approx 0$ minutes, indicating faster cell migration dynamic compared to grey matter.

3.2.3 Results

Summarizing the results of *in vivo* cell tracks, we found conforming dynamics of cell behaviour in grey and white matter. Durations of periods of speed (≈30min), front leg (≈50min) and rear leg (≈30min) are matching in both areas. We consistently found increases of cell speed preceding cell elongation, where correlation analysis showed that front leg precedes rear leg length (and also orientation). Differences we detected were indications of a slightly faster dynamic of rear leg following front leg length. The most significant change in migration behaviour was the distribution of speed that changed from unimodal, in white matter, to bimodal, in grey matter. However,

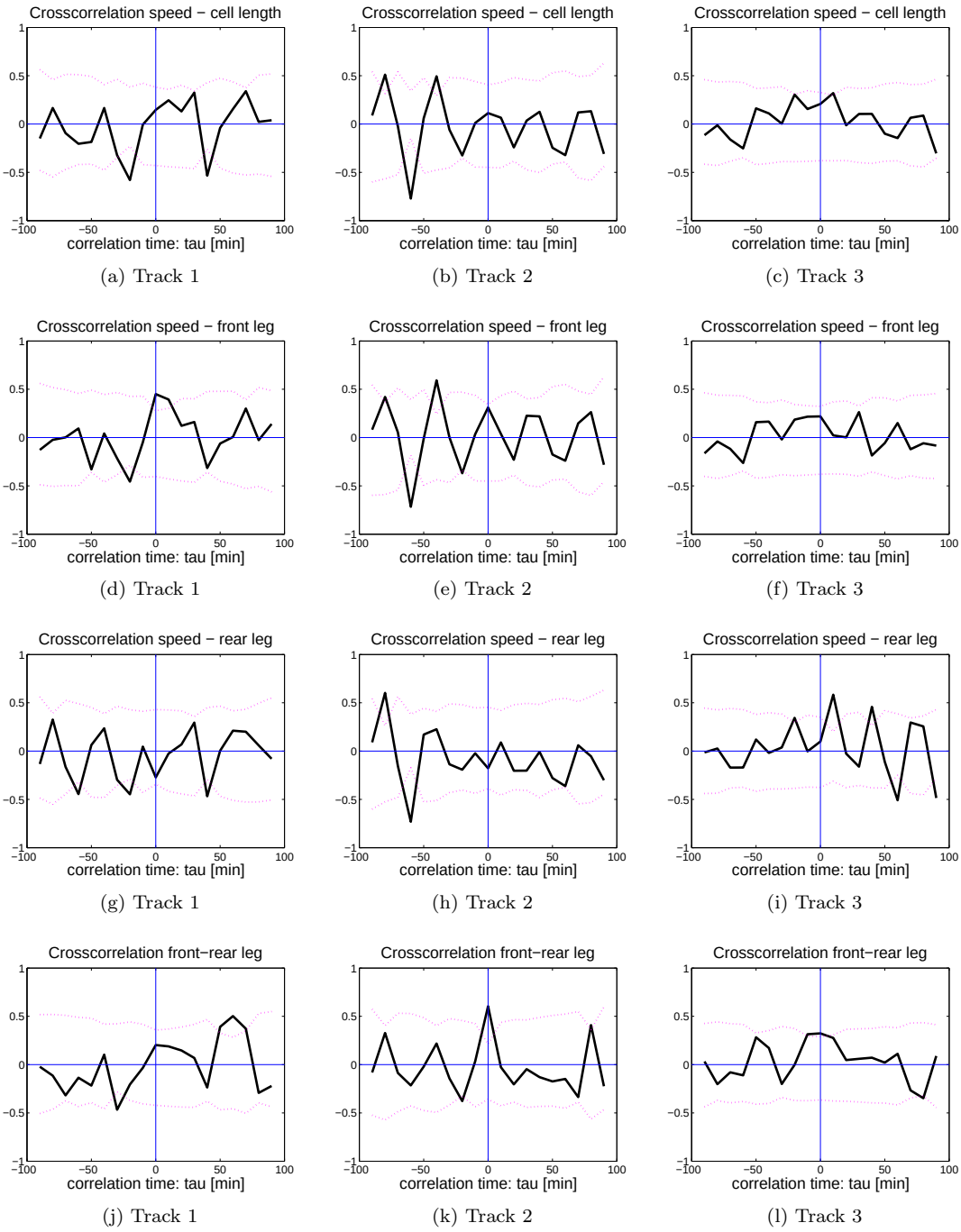

(a) Track 1 (b) Track 2 (c) Track 3

(d) Track 1 (e) Track 2 (f) Track 3

(g) Track 1 (h) Track 2 (i) Track 3

(j) Track 1 (k) Track 2 (l) Track 3

Figure 3.12: Crosscorrelation of overall cell speed and leg lengths for three selected cell tracks within the white matter. **(a)-(c)** Overall length. **(d)-(f)** Front leg length. **(g)-(i)** Rear leg length. **(j)-(l)** Crosscorrelation of front leg with rear leg. Maximum correlation time $\tau_{max} = 100min$ represents a third of the complete time series length. 10 minutes between images. Dotted magenta line indicates significance threshold.

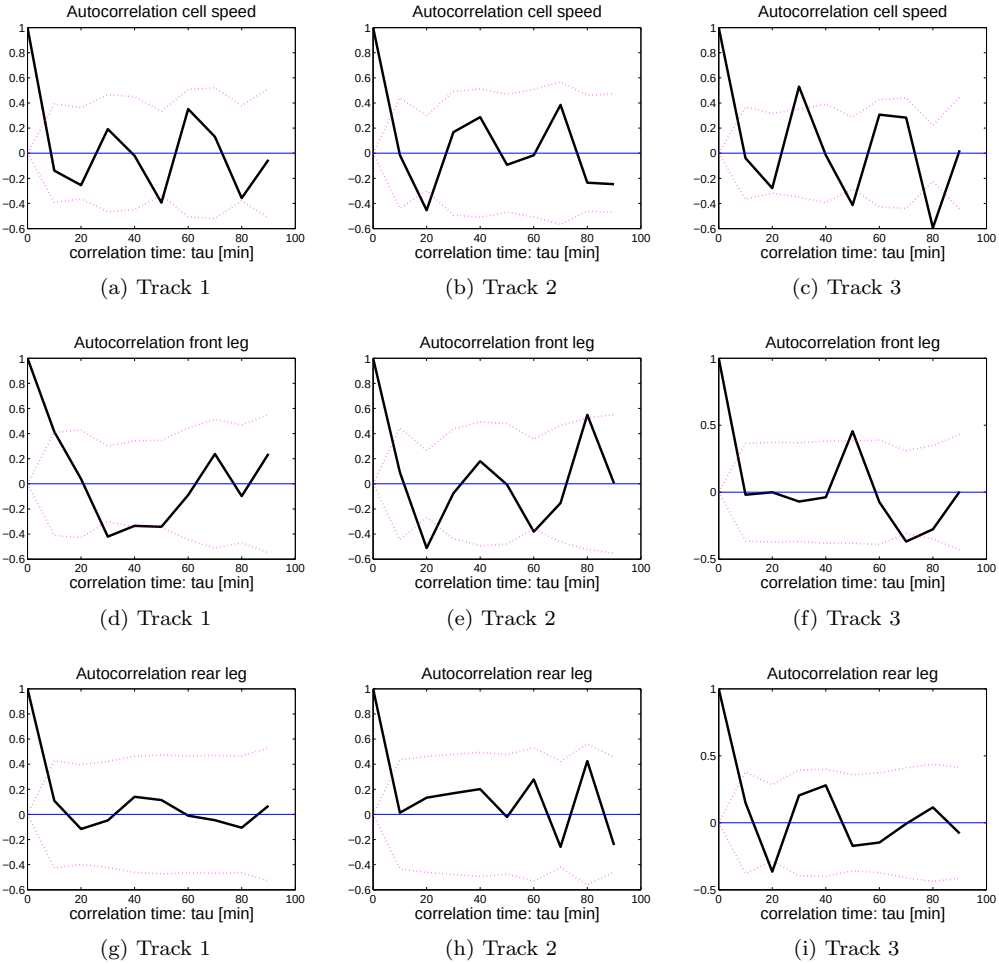

(a) Track 1 (b) Track 2 (c) Track 3

(d) Track 1 (e) Track 2 (f) Track 3

(g) Track 1 (h) Track 2 (i) Track 3

Figure 3.13: Autocorrelation of cell speed and leg lengths for three selected cell tracks within the white matter. **(a, b, c)** Autocorrelation of speed *s*. **(d, e, f)** Autocorrelation of front leg length. **(g, h, i)** Autocorrelation of rear leg length. Maximum correlation time $\tau_{max} = 100min$ represents a third of the complete time series length. 10 minutes between images. Dotted magenta line represents significance border.

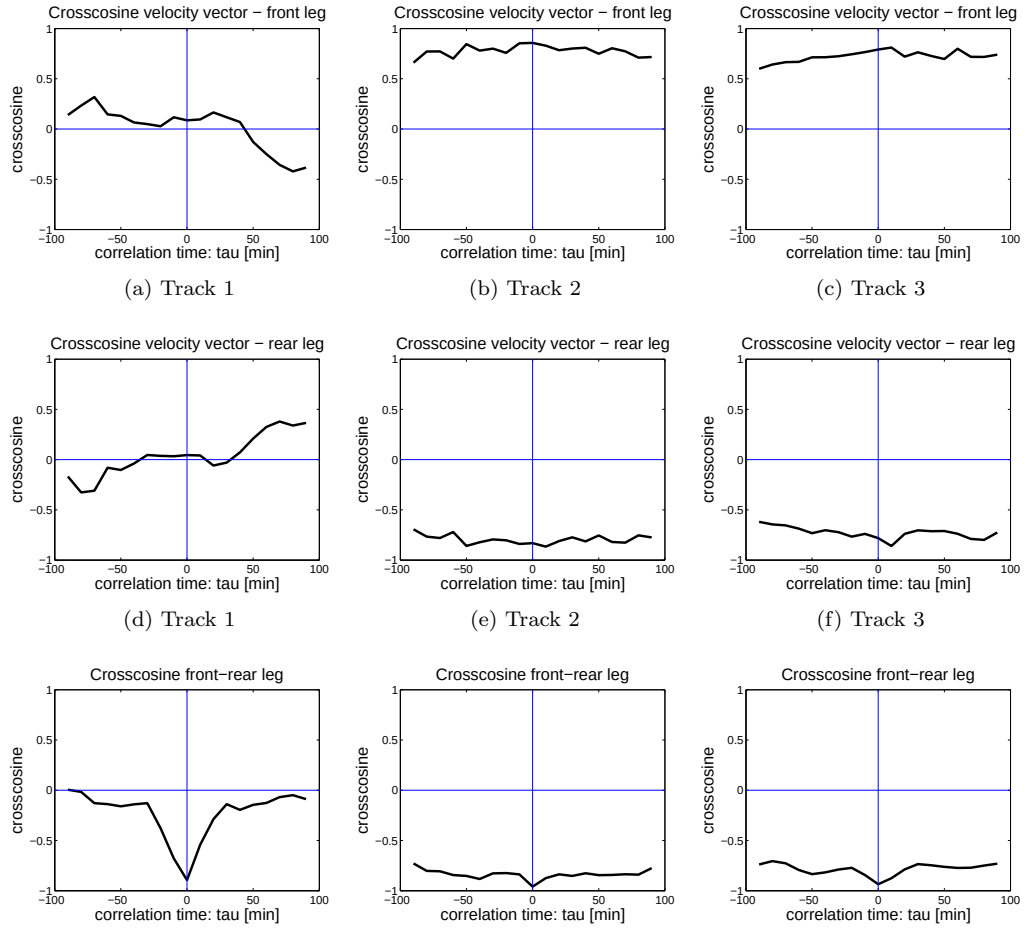

(a) Track 1 (b) Track 2 (c) Track 3

(d) Track 1 (e) Track 2 (f) Track 3

(g) Track 1 (h) Track 2 (i) Track 3

Figure 3.14: Crosscosine of velocity vector with front, **(a)-(c)**, and rear leg, **(d)-(f)**, directions for three selected cell tracks within the white matter. **(g)-(i)** Crosscosine front leg with rear leg. Maximum correlation time $\tau_{max} = 100min$ represents a third of complete time series length. 10 minutes between images.

the range of observed velocities was equal in both cases. Additionally, path reversals were only observed in grey matter.

Thus, overall migration dynamic seems unchanged, the main difference being the appearance of path reversals and a corresponding change of the distributions of cell speed after entering the grey matter area.

3.3 Simulated cell paths

We will now compare simulation results of the previously introduced model (see chapter 2) to results of tracking of grey and white matter cell tracks. The goal is to reproduce real cell tracks as well as possible, and deduct information from necessary model settings. Specifically, we hope to gain an understanding of the differences between white and grey matter migration.

3.3.1 Grey matter

First, parameter settings have been explored to reliably generate tracks comparable to previously analyzed grey matter tracks. Unexpectedly, the best way to consistently achieve path reversal and a bimodal distribution of speeds is to reduce guidance to very low levels and even to zero, effectively turning off structural guidance. Originally, a guidance influence of the structure was introduced to encourage persistent migration and to avoid a 1-dimensional random walk effect (i.e. low effective displacement over long times) that is generated by many parameter sets with only structural attraction present.

Table 3.2 shows the applied parameter set and figures 3.15a and 3.16a display a typical cell track and histogram of speeds generated with this set. Looking at the cell path, we clearly see phases of orientation, characterized by turning events and path reversals (for instance, around the 10 μm mark), as well as phases of constant migration. Comparison of the histogram confirms this impression by showing a very distinct bimodal distribution.

Taking a look at plots of cell speed and protrusivity, as well as polarity vector lengths over time (fig.3.15b), we see that protrusivity (green) precedes cell speed (blue), which in turn precedes cell polarity (red). This is as expected and explained by the way our model works, particularly with adjustment time T_p larger than T_m (compare chapter 2 & tab.3.2). Crosscorrelations of velocity vector with protrusivity and polarity vectors (figs.3.16 (b), (c)) show clear positive correlation at small negative (protrusivity, (b)) or positive (polarity, (c)) τ, respectively. Confirming that the sequence of changes is indeed protrusivity, speed and, last, polarity. This is further supported by crosscorrelation of polarity and protrusivity (fig.3.18d) showing positive correlations for negative time delays.

In the time series plot (fig.3.15b) we see regular peaks of cell speed (blue) with intervals of about 8 minutes. This periodicity is confirmed by autocorrelation analysis showing a shoulder at the 8 minute mark (fig.3.17a). Autocorrelation of polarity

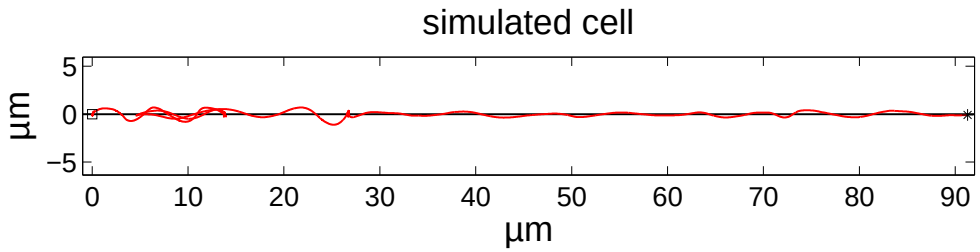

(a) Path

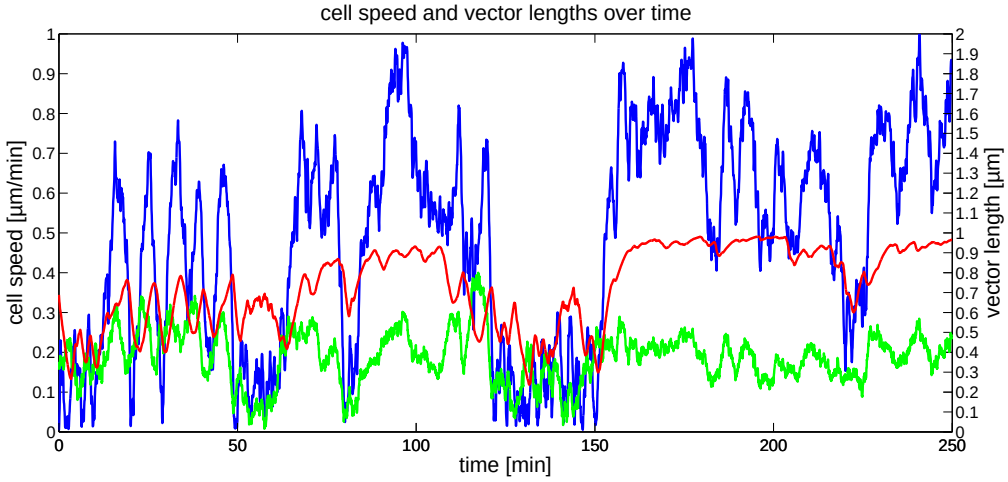

(b) Timeplots

Figure 3.15: **(a)** Simulated cell path in grey matter with 5000 timesteps. Black box denotes starting position. Black asterisk denotes final position. Red line marks the cell path, black line depicts the guiding structure. **(b)** Cell speed (blue), protrusivity (green) and polarity (red) vectors over time of the path in (a). Curves smoothed with a weighted moving average with a width of 2 and weights of [0.25, 0.5, 1].

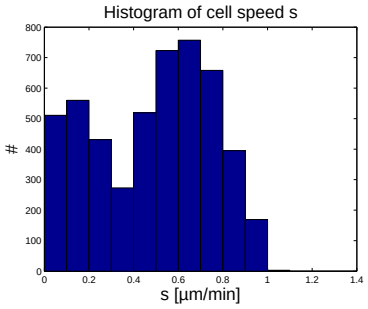

(a) Histogram

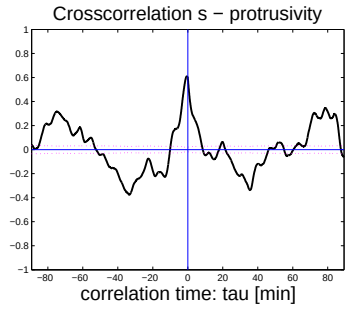

(b) Crosscorrelation speed-protrusivity

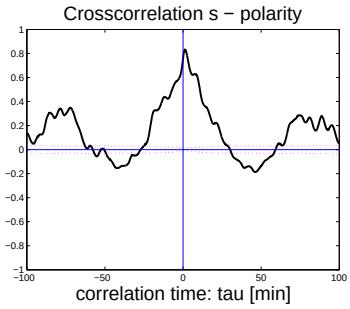

(c) Crosscorrelation speed-polarity

Figure 3.16: **(a)** Histogram of cell speed. **(b, c)** Crosscorrelation of overall cell speed s and length of protrusivity and polarity vectors, respectively. Correlation step size $d\tau = 0.05$ for all graphs. Magenta line denotes significance border.

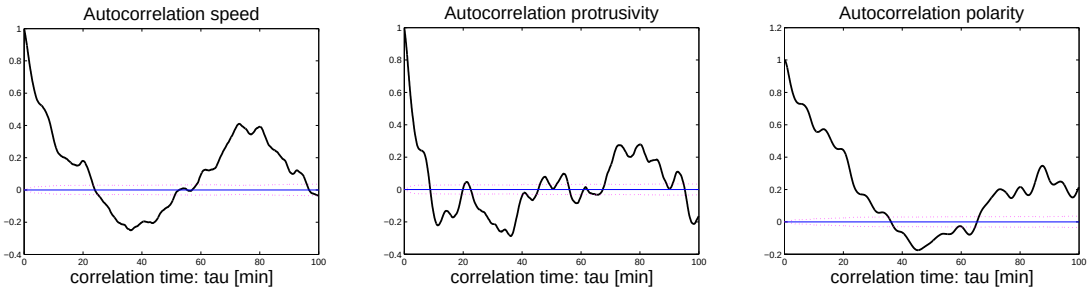

(a) Autocorrelation speed (b) Autocorrelation protrusivity (c) Autocorrelation polarity

Figure 3.17: Autocorrelations of overall cell speed s and magnitudes of cell protrusivity and polarity vectors. Magenta line denotes significance border.

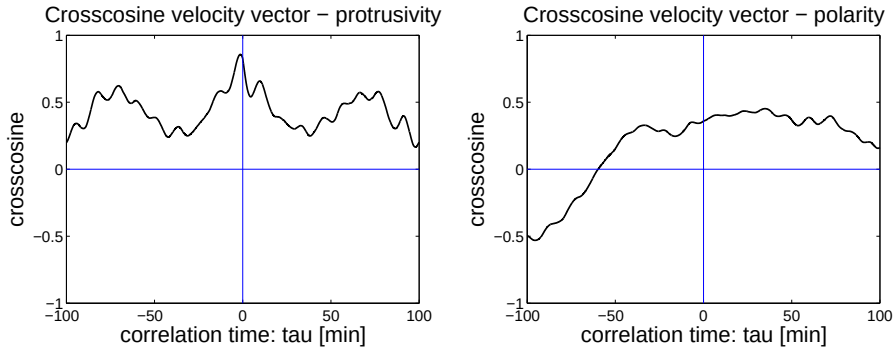

(a) Crosscosine velocity-front (b) Crosscosine velocity-rear

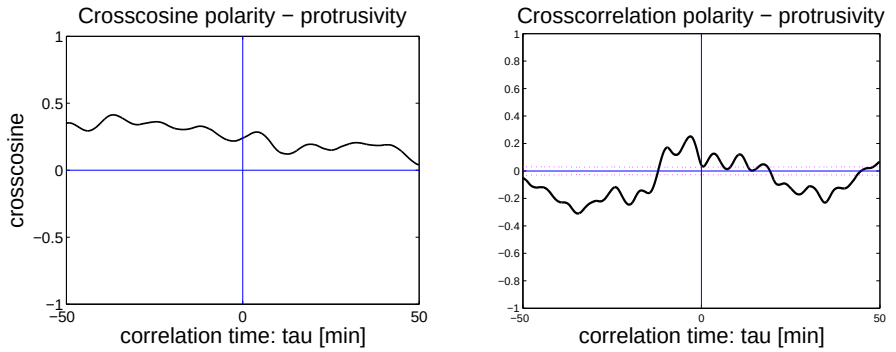

(c) Crosscosine rear-front (d) Crosscorrelation polarity-protrusivity

Figure 3.18: **(a),(b)** Crosscosine of velocity vector and protrusivity and polarity vectors, respectively. Maximum correlation time $\tau_{max} = 50$. **(c)** Crosscosine polarity-protrusivity. Maximum correlation time $\tau_{max} = 50$. **(d)** Crosscorrelation polarity-protrusivity. Maximum correlation time $\tau_{max} = 50$. Correlation step size $d\tau = 0.05$ for all graphs. Magenta line denotes significance border in all correlation plots.

parameter	value	meaning
b_{r0}	0.2	base fluctuation protrusivity parallel
b_0	0.5	base fluctuation protrusivity perpendicular
T_m	2	adjustment time W→P
T_p	3	adjustment time P→W
T_{w0}	1	adjustment time W→W0
w_0	0.3	base protrusivity
$\mathbf{c_h}$	**0(!)**	**structure guidance constant**
c_v	2	structure attraction constant
c_r	3	influence of polarity on protrusivity parallel fluctuation
c_b	5	influence of polarity on protrusivity perpedicular fluctuation
c_w	10	influence of polarity on adjustment time —W—→w0
s_0	2	base cell speed
t_{end}	250	simulation run time
dt	0.05	simulation step size
(x,y)	(0,0)	starting position
ϕ	$-\frac{\pi}{2}$	starting orientation

Table 3.2: Simulation parameters to model a grey matter path. Specifically of note is the fact that path reversal and speed distribution are very well mirrored with structure guidance turned off (c_h=0).

and protrusivity both mirror this interval (see figs.3.17c and 3.17b), which is in line with the observed crosscorrelation results of these values showing positive correlations at positive and negative time delays τ, respectively. This overall periodicity with a duration of 8 minutes results from the meandering form of migration the cell describes (see fig.3.15a). Additionally, we find significant autocorrelations at much higher delays. For speed and polarity these correlations correspond to the waiting time between phases of very low cell speed noticeable in the time series. Comparing the time series (see fig.3.15b), the cell shows reduced speed at around 60 minutes, 130-150 minutes and 230 minutes and, thus, we find positive autocorrelation of cell speed at about 75-80 minutes. These times of reduced migration speed are mirrored in the speed histogram as the first peak of the bimodal distribution. Furthermore, polarity again trails cell speed with a delay and shows positive correlation at 80-85 minutes. Protrusivity, on the other hand, displays shorter waiting times of about 22-24 minutes, which can likely be attributed its generally faster dynamic. Noticeably, Noticeably, we found a different result for *in vivo* cells, where we detected higher duration of front leg period compared to cell speed period.

Crosscosine of velocity and protrusivity direction (fig.3.18a) shows similar results to the corresponding crosscorrelation plot (fig.3.16b) and confirms that cell speed not only follows protrusivity in quantity (vector length), but also in direction. The crosscosine plot of velocity and polarity direction shows the same quality as the cross-correlation plot of the same values (fig.3.16c) and these results mirror the ones for crosscosine of speed and rear leg of *in vivo* grey matter tracks. For this comparison, it needs to be kept in mind that rear leg direction is opposite to migration direction, while the polarity vector always points forward. However, it can be seen that cross-cosine values are overall smaller for negative τ and increase for positive τ (fig.3.18b). Thus, we can confirm that in our model cell polarity follows migration direction (velocity vector orientation) in a similar way than was determined for real cells in grey matter. Correlation analysis of relation of polarity and protrusivity shows that cell elongation and direction follow protrusivity changes (see figs.3.18(c)&(d)).

Addition of small amounts of guidance lowers the occurrence of path reversals and shifts the left peak of the bimodal distribution towards high speed values. However, higher amounts of guidance lead to tracks similar to white matter tracks. A property that will be examined in the next section.

3.3.2 White matter

As noted before, an increase in structural guidance lowers the appearance of path reversal, leads to an increase in higher speeds and, thus, shifts the bimodal distribution towards a single peaked distribution. Consequently, we increased structural guidance to model cells migrating in white matter. An exemplary resulting cell path can be seen in figure 3.19a. Simulated cells migrate very persistently along the structure and path reversals do not happen anymore. However, due to current model constraints increased guidance leads to higher cell speeds (fig.3.19b). This shift can be remedied by a lowered base speed (activity) s_0 and should be seen as a technical necessity not to be interpreted biologically. However, it is additionally necessary to slightly increase fluctuation of protrusive activity (b_{r0}). To recap, b_{r0} is the fluctuation constant governing protrusivity vector length fluctuations and does not affect orientation fluctuation of protrusivity.

parameter	value	meaning
b_{r0}	0.2	base fluctuation protrusivity parallel
b_0	0.5	base fluctuation protrusivity perpendicular
T_m	2	adjustment time W→P
T_p	3	adjustment time P→W
T_{w0}	1	adjustment time W→W0
w_0	0.3	base protrusivity
$\mathbf{c_h}$	**0.1**	**structure guidance constant**
c_v	2	structure attraction constant
c_r	3	influence of polarity on protrusivity parallel fluctuation
c_b	5	influence of polarity on protrusivity perpendicular fluctuation
c_w	10	influence of polarity on adjustment time —W—→ $w0$
s_0	2	base cell speed
t_{end}	250	simulation run time
dt	0.05	simulation step size
(x,y)	(0,0)	starting position
ϕ	$-\frac{\pi}{2}$	starting orientation

Table 3.3: Simulation parameters to model a white matter path. Structure guidance constant c_h set to half its original value lowers occurrence of path reversals and leads to an unimodal distribution of speeds.

Thus, we change parameters accordingly (see tab.3.4) and run more simulations. Exemplary results can be seen in figs.3.20 and 3.21. The appearance of cell paths did not change, but distribution of speeds now resembles the real observed one more

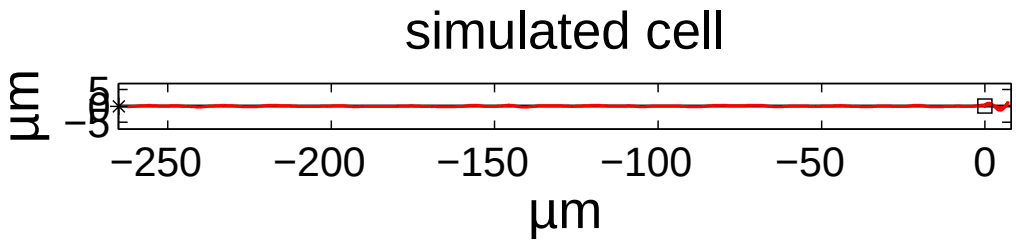

(a) Path

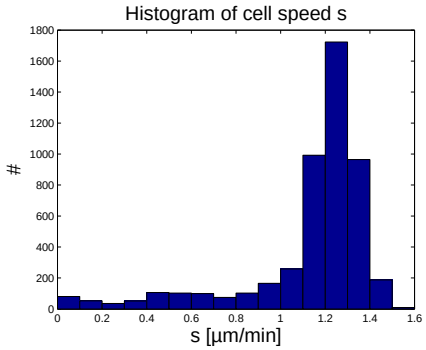

(b) Histogram

Figure 3.19: **(a)** Simulated cell path in white matter with 5000 time steps. Black box denotes starting position and black asterisk final position. Red line depicts cell path, black line depicts guiding structure. Changes to grey matter: $c_h : 0.01 \rightarrow 0.1$. **(b)** Histogram of cell speeds of path in (a).

closely. Since it was necessary to adapt fluctuation of protrusive activity for white matter modeling, we propose that this increased value should be used in grey matter modeling as well. Indeed, we have tested this and apart from broader peaks due to higher variety paths are very much unchanged (data not shown). Thus, we want to note that to switch from grey to white matter paths, the only effectively adapted parameter is guidance strength.

parameter	value	prev. value	meaning
b_{r0}	0.3	0.2	base fluctuation protrusivity parallel
s_0	1	2	base cell speed/activity

Table 3.4: Changes to simulation parameters for modeling a white matter path to shift distribution of speeds.

Continuing our analysis of the simulations, we take a look at time plots and cross-correlations of cell speed, as well as protrusivity and polarity vectors. Figure 3.20b shows cell speed (blue) and magnitudes of protrusivity (green) and polarity (red) vectors over time. Cell polarity is very high throughout the whole simulation run, indicating that the cell is polarized and migrating quite fast and consistently without phases of slowed movement. Polarity and protrusivity follow each other closely with a short time delay (see fig.3.20c), where protrusivity precedes cell speed, which is particularly visible at peak areas. Crosscorrelation confirms this, and shows that the time delay is indeed very small (fig.3.21b). We also notice that crosscorrelation analysis of speed and polarity (fig.3.21c) shows a broad maximum for small positive time delays. Thus, polarity vector length follows migration speed fluctuations, which is in line with previous results for grey matter simulations and *in vivo* analysis. Crosscorrelation of polarity and protrusivity vectors interestingly shows highest correlation at a positive τ of approximately 3 minutes, but also displays a very broad shoulder towards negative τ. Derived from crosscorrelation graphs of these two values with cell speed (figs.3.21b and 3.21c) polarity is expected to follow protrusivity. The increased correlation for positive τ is likely due to the influence of the consistently very high polarity influencing protrusivity fluctuation (compare eqs.2.13).

The time series again shows clear periodicity of cell speed and protrusivity. Autocorrelation of these values shows that this period has a length of 6 minutes (notice the shoulder in fig.3.21e and the small peak in fig.3.21f at 6 minutes). This value is smaller than the one found for grey matter simulations and indicates faster meandering of the cell around the structure. Autocorrelation of polarity again shows a longer period of

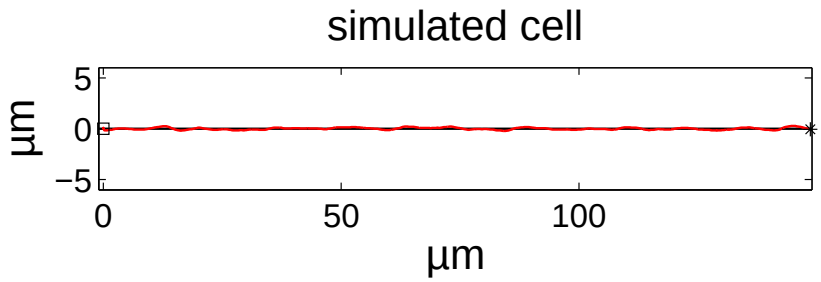

(a) path

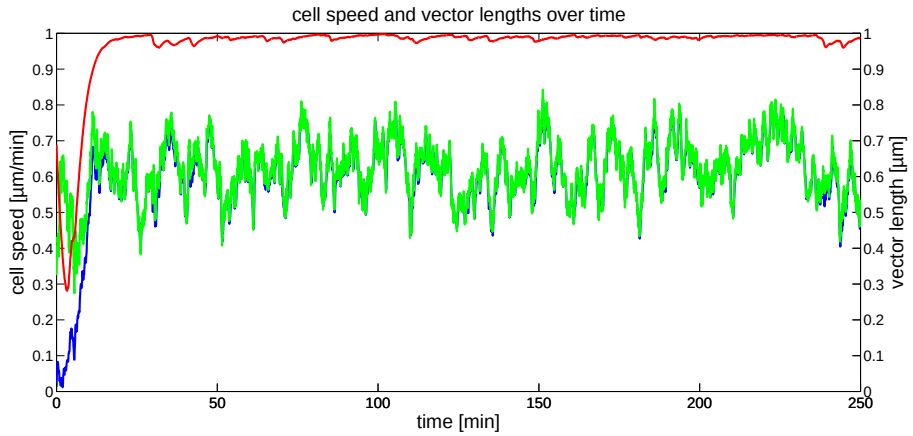

(b) Timeplot

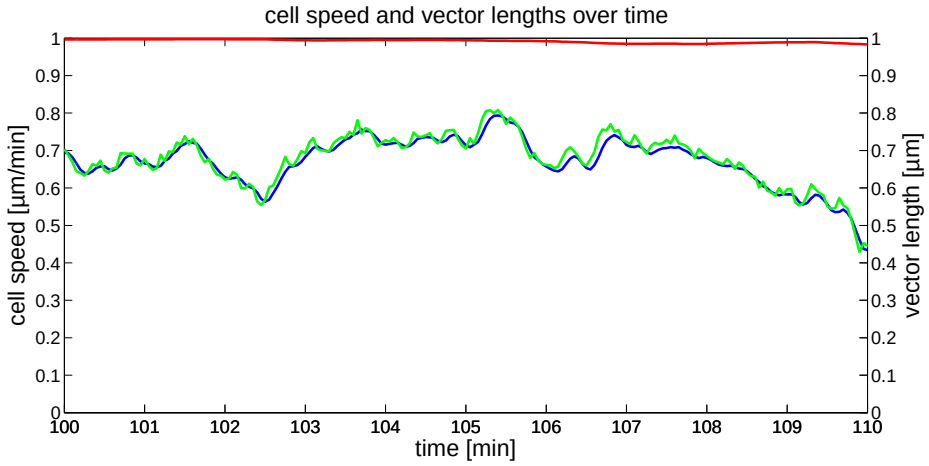

(c) Section

Figure 3.20: **(a)** Simulated white matter path with adapted s_0 and b_{r0}. Black box denotes starting position, black asterisk denotes final position. Red line depicts cell path, black line depicts guiding structure. **(b)** Time series of cell speed (blue) and magnitudes of protrusivity (green) and polarity (red) vectors. **(c)** Section of (b) displaying time between 100-110 minutes. Curves in (b) and (c) smoothed with a weighted moving average of width 2 and weigths of [0.25,0.5,1].

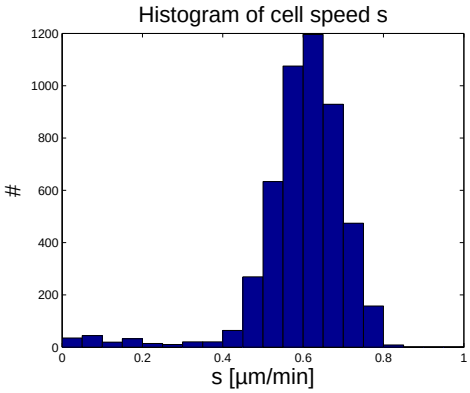

(a) Histogram speed

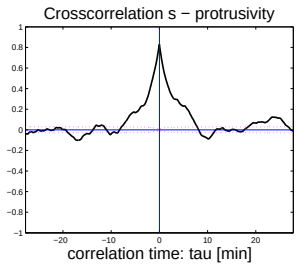

(b) Crosscorr. speed-protrusivity

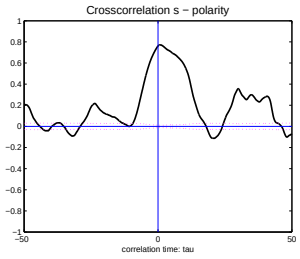

(c) Crosscorr. speed-polarity

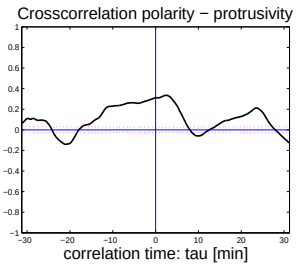

(d) Crosscorr. polarity-protrusivity

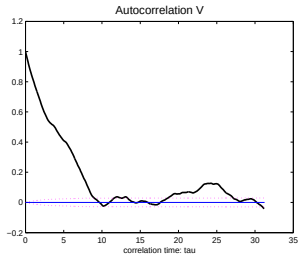

(e) Autocorrelation speed

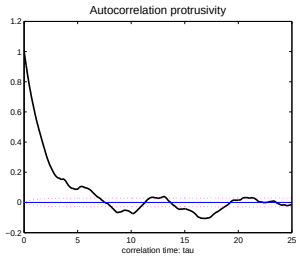

(f) Autocorrelation protrusivity

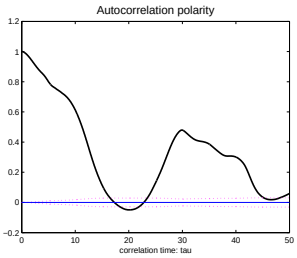

(g) Autocorrelation polarity

Figure 3.21: **(a)** Histogram of cell speeds of path in fig.3.20a. **(b)** Crosscorrelation of speed and protrusivity. **(c)** Crosscorrelation of speed and polarity. **(d)** Crosscorrelation of polarity and protrusivity. **(e)** Autocorrelation of speed. **(f)** Autocorrelation of protrusivity. **(g)** Autocorrelation of polarity. Dotted magenta line denotes significance border in all correlation plots. Correlation step size $d\tau = 0.05$, maximum correlation time τ_{max} varying between correlations (refer to maximum x-axis ticks).

about 9 minutes and a higher persistence (see fig.3.21g) compared to cell speed and protrusivity. This is equal to results of grey matter simulations. Furthermore, we see significant correlations at higher time delays. In contrast to grey matter simulations these correlations are less pronounced. Because we attributed these correlations to waiting times between phases of slowed migration in grey matter paths, these results originate from the more consistently migrating cell. However, for cell speed and protrusivity we find significant autocorrelation at about 12 minutes (figs.3.21e and 3.21f) and for polarity at about 24 minutes (fig.3.21g).

Crosscosine analyses for the very straight path with consistently high polarity we observe here, show overall very high values close to 1 and are, thus, not very informative (graphs not displayed).

3.4 Discussion

In the first section of this chapter we have employed our tracking program to several image stacks of interneuronal precursor cells migrating in extracted slices of grey and white matter of a mouse cerebellum. We have confirmed the visual impression of two differing modes of migration within these tissues. Biologically, this can easily be explained by considering the different stages/goals of this migration. Originating from the germinal layer, interneuronal precursors travel a long distance through white matter to ultimately veer towards and enter grey matter tissue to search for their final destination and then establish connections with surrounding neurons. Thus, white matter migration is long distance, while grey matter migration is short distance and includes searching for a suitable destination location. This is reflected by extracted data confirming a higher mean speed with a steady form of migration in white matter and a more saltatory mode of migration in grey matter, including stopping of cells and occasional path reversals.

Furthermore, we have gathered evidence for a periodicity in cell speed of about 30 minutes and this value seems consistent for both tissues. We could not determine the time relation between protrusion and cell body displacement. This is in part due to the time resolution of the supplied time-lapse movies, but also due to an image resolution where the size of cells only measures a few pixels. A coarse resolution with few pixels to track leads to a more difficult fitting process with higher inaccuracies and, thus, a higher fluctuation of results, possibly overshadowing cell dynamics. However, we found indication that the rear part of the cells is being dragged and elongates (passively) due to increased cell speed. The delay for this is the same as for orientation

adaption of the cell rear towards migration direction and takes roughly 10 minutes (one image). This could originate from active reorientation or, much more likely, be a passive result of cell center translocation. This process seems to be slightly faster in white matter, which we attribute to either extracellular factors (for instance, weaker attachment to the guiding structure) or a higher base activity of the cell.

Using the collected information and data from previous works [19] we have then developed a model of migrating interneuronal precursor cells. The model incorporates migration based on actual cell polarity, which is in turn influenced by protrusive activity (protrusivity). As we propose that these cells are using leading structures to guide their way, protrusivity in our model is influenced heavily by outside factors, namely structural guidance and alignment. Structural alignment is modeled as attraction towards the structure, the range of this influence can be used as a model parameter and thus can be easily interpreted as contact, as well as a short-distance signaling. The exact form of interaction *in vivo* cannot be determined from available data at this point, even if a form of contact guidance is most likely.

Structural guidance has been introduced to relay information about migration direction to the precursor cells. We noticed that simple structure attraction often leads to one-dimensional random walk patterns with cells turning around and migrating back the way they came, resulting in long paths with almost no effective displacement from the starting location. We introduced a guidance effect that does not relay a certain preferred direction, but instead enhances any built-up polarity and thus increases persistence of migration. After running several simulations it soon became clear that this form of guidance is absolutely sufficient to explain migration behaviour of real cells, including a change in mode of migration as seen for white and grey matter track *in vivo*. Indeed, our model predicts that the observed change in cell behaviour could be attributed completely to properties of the guiding structures.

To achieve results comparable with real grey matter paths, particularly a bimodal distribution of speeds, it was necessary to introduce a strong influence of polarity on protrusivity reset time. In effect, the more expressed cell polarity is, the longer the adjustment time of actual protrusivity ($\mathbf{W}$) reverting towards base protrusivity (w_0, see eq.2.7). This setup leads to phases of persistent migration alternating with phases of stopping and reorientation. Expectedly, we noticed that an increase in structural guidance decreased the frequency of slowed, or stopped, migration and, thus, of path reversals. Furthermore, we found that only a very small amount of structural guidance is necessary to achieve consistent grey matter-like migration in simulations. Finally, an increase in guidance strength leads to paths with no reversals very much similar to

white matter paths. However, due to model constraints, a higher guidance strength leads to faster movement and it is therefore necessary to lower the base protrusive activity of the cell. This is because of the way guidance is worked into protrusivity and, ultimately, migration.

In conclusion, we have shown that our model of structure influenced protrusive activity is not only capable of mimicking migration behaviour of interneuronal precursor cells, but is also able to distinguish migration between grey and white matter surroundings, predicting that the observed change of migration behaviour can be explained purely by extracellular influence.

Discussion

We have developed a tracking program suitable to record migration of single migrating cells in 2D-specimens and have used this method to analyze time-lapse recordings of cerebellar slices of P8 mice containing Pax2-GFP stained interneuronal precursor cells. In chapter 1 we have shown that the current version of the program that implements our method works well for its intended use and is indeed suitable to track migrating cells automatically and consistently. As with all tracking programs, quality of results heavily depends on the given images. Image resolution, size of cells to track in pixels, background noise and additional structures and/or cells that shall not be tracked influence any automatic tracking process. However, our program deals with these issues quite well. As we have shown it is able to track cells that consist of a fairly small number of pixels (compare fig. 1.9). Furthermore, by introducing a brightness threshold for force generation (H_{th}) we have added a parameter to account for background noise. Setting this parameter appropriately reduces influence of background noise, depending on brightness fluctuation strength of the noise. Not under our control and very difficult to account for is the presence of secondary structures marked unintentionally by the employed preparation techniques. For instance, Purkinje cells in the time-lapse sequences that formed the basis of this work regularly absorb GFP and are thus readily visible and will be tracked by the automatic tracking program, thus, proper experimental procedures and selection of suitable methods for image generation, as well as adequate selection of (stacks of) images to track remain important for handling this issue.

While the current version of the software implementing our method is suitable to automatically track single cells, any automatic tracking program is most useful if it can be applied to images containing multiple cells successfully and consistently. Manual extraction of a single cell out of a movie by, for instance, selecting a RoI and cutting, is time consuming and prone to subjective choices, and hence, errors. Some enhancements to the program will be necessary so that it can be used to track

multiple cells in given images. Among others, an important issue is how to deal with cells that are not visible in all images of a given stack. In practical use, this 'loss (or gain) of cell visibility' may have two main reasons. First, cells can migrate out of (into) the focal plane and, thus, disappear (appear) in consecutive images. And second, fast moving cells may not be recognized as the same object in consecutive images. Thus, the software needs to keep track of already processed cells and be able to handle newly appearing cells (and, ideally, even identify reappearing cells). In the same manner, it needs to be able to distinguish between disappearing cells and cells that have been lost for moving outside of detection range.

A first step in this direction is to bolster detection abilities to decrease the occurrence of cell loss due to fast migration. To achieve this, it would be possible to enhance the main program by introducing a *cone shaped detection* range in movement direction, instead of the fixed *all around detection* currently employed. This will allow to increase detection range in the direction a cell will move with highest likelihood, while decreasing detection in other directions. Not only will this increase the chance of reacquiring a cell that is lost during tracking using the present implementation of our method, but if properly integrated it will also lower program runtime due to an overall reduced detection area. However, proper scaling of this cone by movement speed, and possibly other factors yet to be determined, will be important. Also, additional conditions might have to be introduced to minimize detection of unrelated cells using this method.

Thus, despite the mentioned caveats, the above results suggest that the current version of the method, and its implementation in the program described here, performed reliably and allowed to faithfully track neuronal migration. We have used these data to compare to, and improve, a model of cerebellar interneuronal migration (see chapter 2).

Given the importance of cell migration in many biological processes, like, for instance, embryogenesis and wound healing, modeling of cell dynamics and migration, and subsequent data analysis, has been an active topic for many years. Consequently, a great many models of cell migration, as well as methods for data analysis, have been developed. The sheer number of models makes it difficult to give an exhaustive overview, but generally they range from single cell to population models including large numbers of cells. Additionally, due to the nature of modeling and the great range of cell types, as well as research interests, almost all of these models focus

on very specific details of cell migration or dynamics. To get the interested reader started on this topic, we can only recommend a select few initial pointers. In an early work, Alt [27] covered the migration of bacterial cells using a random walk algorithm. Additionally, this model includes chemotactical considerations for biased migration. Looking at eukaryotic cells, Dunn [28] deals with protrusion and retraction dynamics in single migrating keratinocytes, Tranquillo [29] explores lamellipodial dynamics of migrating cells, Rubinstein [30] presents a multiscale model of a simple shaped cell similar to keratinocytes and 1996 Tranquillo [31] discussed receptor-mediated leukocyte dynamics. A discreet model of cell migration can be found in [32] and Zaman presents an example of force based migration modeling in three dimensions [33]. Finally, for a recent review on models see Mogilner 2009 [34].

For modeling of guidance and attraction effects of extracellular structures or matrix on cell migration, population models are used almost exclusively, except for chemotactical models which are usually used to model prokaryotic behaviour. The models usually employ diffusion mechanics to describe positional changes of cells ([35], [36] & [37], for instance). Dickinson [35] integrates guidance as an ECM dependent change in turning behaviour. In his model, the turning of cells towards a guiding structure is dependent on the cell's distance to that structure. Chauviere [36] uses a more artificial approach termed "phenotypic switching". This approach defines a fast and a slow mode of migration that cells shift between, depending on their distance to a guiding structure. An example of discreet cell modeling including guidance influences is given by Dallon [38], which covers migration of fibroblasts and includes reciprocal interaction with the fibronectin matrix to achieve guided migration and alignment of cells and ECM. For an introduction on single- and multiscale modeling of cell mechanics see [39].

To our knowledge, our own approach of modeling a discreet cell using protrusive activity (protrusivity) as a key parameter to describe cell migration is a novel one. We propose protrusivity to be the cell's internal activity resulting in the formation of protrusions and eventually migration. In our model, protrusivity is represented as a vector influenced by surrounding structures and, to a lesser degree, reciprocally by the cell's polarity. In contrast to other approaches ([36], for instance) that include predefined modes of migration that cells just switch between, our approach better models biological reality, in our opinion. Furthermore, it appears reasonable that extracellular cues of any form rather result in graded intracellular changes, and not in binary-type distinct switches into different modes. Not to mention that phenotypical changes in migration ("modes") are ultimately based on intracellular activity, as well.

Incorporating this approach by use of our model, we could show that changes in the mode of migration can be achieved solely by extracellular effects influencing intracellular (protrusive) activity. These effects have been split into an attraction and a guidance part, implemented as additive influences on protrusive activity. Exploring simulated migration behaviour under differing weights of these influences (without structure influence, with guidance only, attraction only and guidance plus attraction), we found that both terms (attraction and guidance) were necessary to consistently mirror tracking results of interneuronal precursor cells (for, both, grey and white matter) and achieve persistent directed migration.

Since our model incorporates a single guiding structure only, it could be argued that any attractive influence is simply a necessity in our model to keep the model cell from leaving the vicinity of this structure. In the *in vivo* environment of the cerebellum, the number of guidance structure candidates is much higher and it may be presumed that attraction will not be necessary under these circumstances. Any cell that migrates away from a given guiding structure will inevitably reach another guiding structure and regain any eventual guidance influence. Nevertheless, an attraction mechanism could guarantee double safety by increasing the probability to find leading structures and stay within effective range of these structures.

Consequently, our model predicts that no internal reorganization is necessary to facilitate migration from white to grey matter and that any phenotypic changes of migration result from differences of the surrounding tissues. For the interneuronal precursor cells we observed in this work, this might well be a change from structures prevalent in white matter, like Purkinje cell axons, mossy fibers or even non-cellular ECM (as fibrous hyaluronic acid), to structures prevalent in grey matter, e.g. Purkinje cell dendrite trees, Golgi cell axons and others.

The primary result of comparison of tracks of real cells to paths of modeled cells is certainly the discovery that different modes of migration can be caused by the structure of extracellular space only. Naturally, these influences affect internal cell processes that govern protrusive activity, but we avoided the introduction of distinct (artificial) modes of migration regulation. For instance, conditional switching of suitable parameters, like changing base cell speed or turning behaviour based on a threshold distance from a leading structure. Indeed, in our model no parameter changes regarding cell properties are necessary at all to achieve different phenotypes of migration. Rather, structure relayed influences based on distance affect internal

cell activity (protrusivity), which then governs cell migration. Concerning this topic, it has been shown that distinct changes, observed, for instance, in granule cell migration, are caused very likely by extracellular cues [40]. Nakatsuji found in the same year that the topographical arrangement of surrounding structures can induce changes in migration [41]. The influence of contact guidance on migration is well recognized by now.

Weiger [42] recently found that a stochastic and rapidly changing intracellular signaling is an important determinant of cell migration in fibroblasts, which supports the validity of our concept of protrusivity. While Weiger used a reaction-diffusion model to predict cell migration direction based on signaling hot spots, we model this intracellular activity as a protrusivity vector. However, what both of these approaches have in common are the rapid fluctuations of intracellular organization (be it signaling hot spots or protrusivity vector) and that migration is based on the persistence this intracellular organization.

Taking a further look at the importance of attraction and guidance, in chapter 2 we found that reasonable paths, which show the typical bimodal distribution of speed, may be modeled without setting parameters for attraction or guidance (see figs.2.9(a)-(c)). As mentioned above, attraction might *in vivo* not be necessary due to the high density of potentially guiding structures in the cerebellum. However, in chapter 3 we determined, that attraction alone can result in modeled cell paths mimicking real grey matter tracks quite well. In this case, guidance is only a supporting parameter influencing speed, persistence and occurrence of path reversals and, thus, also ultimately defines whether the cell shows grey or white matter track resemblance. Yet, we also demonstrated that attraction and guidance need to be balanced with each other (see section 2.4.2). If we, thus, interpret attraction simply as a force resulting from attachment of the cell to surrounding structures, it is feasible to predict that an increased density of guiding structures will not influence results. Concluding, we presume that cells migrating along a guiding structure show migration behaviour reflecting both, attachment strength as well as guidance cue strength. Furthermore, if we define the ratio of attraction strength (c_v) to guidance strength (c_h) as influence I ($I = \frac{c_v}{c_h}$), it might be possible to predict structures used as guides in long distance migration by low values of I, and guiding structures used in short range and/or specific positioning by large values of I. As attachment strength can be readily asserted nowadays ([43], [44], for instance) and measurement of guidance cue strength and its influence on cell activity is on the way ([42], for instance) it is reasonable to assume that guiding structures and their primary use (with regard to a specific type of cell)

could be identified by assessing attachment strengths and relayed signaling cues.

Summarizing, in this work we have shown that a model of protrusive activity influenced by guiding structures is suitable to describe real interneuronal precursor cell migrating in real tissue, i.e. slices of developing cerebellum. We further showed that different migration behaviour observed in white and grey matter, respectively, can be attributed just to extracellular cues influencing a cell's protrusive activity. Finally, we predict that guiding structures and their use in long or short distance guidance are potentially recognizable by a characteristic quantity, namely the ratio between cell attachment strength and relayed guidance strength of the structure.

Bibliography

[1] Rakic, "Neuronal-gial interactions during brain development," *TINS*, vol. 13, pp. 184–187, 1990.

[2] Hatten, "Riding the glial monorail," *TINS*, vol. 4, pp. 179–184, 1981.

[3] Voogd, "The anatomy of the cerebellum," *Trends Cog.Sci.*, vol. 2(9), pp. 307–313, 1998.

[4] Goldowitz, "The cells and molecules that make a cerebellum," *Trends Neurosci.*, vol. 21(9), pp. 375–382, 1998.

[5] K. Schilling, "Besides purkinje cells and granule neurons: an appraisal of the cell biology of the interneurons of the cerebellar cortex," *Histochem Cell Biol*, vol. 130, pp. 601–615, 2008.

[6] Zhang, "Developmental fates and migratory pathways of dividing progenitors in the postnatal rat cerebellum," *J.Comp.Neuro.*, vol. 370, pp. 536–550, 1996.

[7] Zhang, "Generation of cerebellar interneurons from dividing progenitors in white matter," *Neuron*, vol. 16, pp. 47–54, 1996.

[8] Maricich, "Pax2 expression defines a subset of gabaergic interneurons and their precursors in the developing murine cerebellum," *J.Neurobiol.*, vol. 41, pp. 281–294, 1999.

[9] D. Hecker, A. Glassmann, J. Kappler, K. Schilling, and W. Alt, "Image analysis of time-lapse movies - a precision control guided approach to correct motion artefacts," *J.Neurosci.Meth.*, vol. 172, pp. 67–73, 2008.

[10] Meijering, "Tracking in cell and developmental biology," *Seminars in Cell and Developmental Biology*, vol. 20, pp. 894–902, 2009.

[11] Meijering, "Time-lapse imaging," *Elsevier Academic Press*, vol. 1, pp. 401–440, 2008.

[12] Kachouie, "A model-based hematopoietic stem cell tracker," *ICIAR*, vol. LNCS 2005, pp. 861–868, 2005.

[13] Kachouie, "Probabilistic model-based cell tracking," *Int.J.Biomed.Imaging*, vol. 2006, pp. 1–10, 2006.

[14] Beucher, "Use of watersheds in contour detection," 1979. Int.Workshop Image Proc.

[15] Blum, "Biological shapes and visual science," *J.theor.Biol.*, vol. 38, pp. 205–287, 1973.

[16] Osher, "Fronts propagating with curvature-dependent speed: Algorithms based on hamilton-jacobi formulations," *J.Comput.Phys.*, vol. 79, pp. 12–49, 1988.

[17] Zimmer, "Segmentation and tracking of migrating cells in videomicroscopy with parametric active contours: A tool for cell-based drug testing," *IEEE Transactions on Medical Imaging*, vol. 21, pp. 1212–1221, 2002.

[18] Ray, "Tracking leukocytes in vivo with shape and size constrained active contours," *IEEE Transactions on Medical Imaging*, vol. 21, pp. 1222–1235, 2002.

[19] D. Hecker, "Bewegungsanalyse neuronaler Vorlaeuferzellen im Cerebellum der Maus." Diploma Thesis. University of Bonn, Dept.theo.Biol., Dec. 2006.

[20] Meijering, "Mtrackj." http://www.imagescience.org/meijering/software/mtrackj/.

[21] Rasband, "Imagej." http://rsbweb.nih.gov/ij/.

[22] Mathworks, "Matlab." http://www.mathworks.com/.

[23] Schafer, "Cell biology: barbed ends rule," *Nature*, vol. 430, pp. 734–735, 2004.

[24] Vallotton, "Tracking retrograde flow in keratocytes: News from the front," *Mol.Biol.Cell*, vol. 16, pp. 1223–1231, 2005.

[25] Weisheit, "Postnatal development of the murine cerebellar cortex," *J.Neurosci*, vol. 44, pp. 466–478, 2006.

[26] Baier, "Hyaluronan is organized into fiber-like structures along migratory pathways in the developing mouse cerebellum," *Matrix Biol.*, vol. 26, pp. 348–358, 2007.

[27] W. Alt, "Biased random walk models for chemotaxis and related diffusion approximations," *J.Math.Biol.*, vol. 9, pp. 147–177, 1980.

[28] Dunn, "Protrusion, retraction and the efficiency of cell locomotion," *Dynamics of Cell and Tissue Motion*, vol. 1, pp. 33–46, 1997.

[29] Tranquillo, "Basic morphogenetic system modeling shape changes of migrating cells: How to explain fluctuating lamellipodial dynamics," *J.Biol.Sys.*, vol. 3, pp. 905–916, 1995.

[30] Rubinstein, "Multiscale two-dimensional modeling of a motile simple-shaped cell," *Mult.Model Simul.*, vol. 3, pp. 413–439, 2005.

[31] Tranquillo, "Stochastic model of receptor-mediated cytomechanics and dynamic morphology of leukocytes," *J.Math.Biol.*, vol. 34, pp. 361–412, 1996.

[32] Nutaro, "A discreet cell migration model," *SCSC*, vol. 0, pp. 811–816, 2007.

[33] Zaman, "Computational model for cell migration in three-dimensional matrices," *Biophys.J.*, vol. 89, pp. 1389–1397, 2005.

[34] Mogilner, "Mathematics of cell motility: Have we got its number?," *J.Math.Biol.*, vol. 58, pp. 105–134, 2009.

[35] Dickinson, "A generalized transport model for biased cell migration in an anisotropic environment," *J.Math.Biol.*, vol. 40, pp. 97–135, 1999.

[36] Chauviere, "A model of cell migration within the extracellular matrix based on a phenotypic switching mechanism," *Math.Med.Biol.*, vol. 0, pp. 1–27, 2009.

[37] Cai, "Modelling directional guidance and motility regulation in cell migration," *Bull.Math.Biol.*, vol. 68, pp. 25–52, 2006.

[38] Dallon, "Biological implications of a discrete mathematical model for collagen deposition and alignment in dermal wound repair," *IMA J.Math.App.Med.Biol.*, vol. 17, pp. 379–393, 2000.

[39] Chauviere, *Cell mechanics: From single scale-based models to multiscale modeling.* CRC Press, 2010.

[40] Komuro, "Distinct modes of neuronal migration in different domains of developing cerebellar cortex," *J.Neurosci.*, vol. 18(4), pp. 1478–1490, 1998.

[41] Nakatsuji, "Paradoxical perpendicular contact guidance displayed by mouse cerebellar granule cell neurons in vitro," *Development*, vol. 106, pp. 441–447, 1989.

[42] Weiger, "Directional persistence of cell migration coincides with stability of asymmetric intracellular signaling," *Biophys.J.*, vol. 98, pp. 67–75, 2010.

[43] Lakshmi, "A simple method for measurement of cell-substrate attachment forces: application to hiv-1 tat," *J.Cell.Sci.*, vol. 110, pp. 249–256, 1997.

[44] Tian, "Quantative method for the analysis of cell attachment using aligned scaffold structures," *J.Physics*, vol. 61, pp. 587–590, 2007.

Summary

The navigation of precursor cells of inhibitory interneurons from their germinal zone inside the fourth ventricle through the white matter towards their final destination within the cerebellum's molecular layer is an ongoing research topic. On the basis of time-lapse images of cerebellar slices of P8 mice we performed automated model-based cell tracking employing image forces derived from pixel brightness values. We found that cells show different modes of migration in cerebellar grey and white matter. Furthermore, we found indication that these cells migrate along guiding structures.

We then developed a model of this type of cell using an approach of structure influenced protrusive activity. We showed that the model is capable of generating cell paths very similar to tracked real cell paths of interneuronal precursor cells and, furthermore, were able to depict both observed modes of migration. Our model predicts that the change in migration behaviour originates solely from a change in guiding structures and not from internal changes of the cells. The two main attributes of a guiding structure, namely attraction of the cells in question and imparting guidance information, are the underlying cause of changes in migration behaviour.

Zusammenfassung

Die Wanderung von Vorläuferzellen inhibitorischer Interneurone von ihrer Keimzone am vierten Ventrikel, durch die weiße Substanz, bis hin zu ihrem endgültigen Zielort in der Molekularschicht des Cerebellums, ist ein aktuelles und aktives Forschungsgebiet. Wir haben eine Methode zur automatisierten Zellverfolgung (Tracking) auf der Basis von Bildkräften, hergeleitet aus Pixelhelligkeiten, entwickelt. Mit Hilfe dieser Methode haben wir die Bewegung von Zellen in time-lapse Aufnahmen von Gewebeschnitten des Kleinhirns von P8 Mäusen verfolgt und ausgewertet. Die Ergebnisse zeigten unterschiedliche Eigenschaften der Migration dieser Zellen innerhalb der weißen und grauen Substanz. Außerdem erhielten wir Anzeichen für die Existenz von Leitstrukturen.

Wir haben dann ein Modell dieses Zelltyps entwickelt, das auf Struktur-beeinflußter protrusiver Aktivität beruht. Wir haben gezeigt, dass dieses Modell in der Lage ist Zellpfade zu generieren die den Tracks echter Zellen vergleichbar sind und zusätzlich fähig ist die beobachteten Änderungen im Migrationsverhalten in den beiden Bereichen (graue und weiße Substanz) nach zu bilden. Unser Modell sagt vorher, dass der Übergang beider Migrationsmodi hauptsächlich von Umgebungsstrukturen und den Eigenschaften des Gewebes herrührt. Die beiden Haupteigenschaften der Leitstrukturen in Bezug auf Migration, Attraktion und Guidance, bilden die Grundlage für diese Veränderungen.